VNIVERSITAT DE VALÈNCIA

Programa de doctorado 3026 Física, RD 1393/2007

Contributions to three problems relevant to cavity quantum optics

PhD dissertation by

Joaquín Ruiz-Rivas Onsés

Under the supervision of

Germán J. de Valcárcel Gonzalvo

Carlos Navarrete-Benlloch

and

Eugenio Roldán Serrano

Valencia, July 2015

A Montserrat y Carlos, mis padres.
A María y Carlota, mis hermanas.
A Daniel y Borja, mis cuñados.
A Carlos, María, Jorge, Pablo y Jaime,
y a los que vendrán.

PROLOGUE

After reading the title of this thesis, one might wonder which is the connection between the three contributions. As we are about to see, they are all framed under the same context and their differences are complementary in such a way that, as a whole, they provide a wide look at the techniques and matters that contemporary quantum optics deals with. However, I would like to mention a more obvious reason that connects them. In order to understand this, one has to look not at the ink on the paper, but at the person holding the pen: these problems are connected because I worked on them during my PhD, although here I have not included all the work I did during my PhD. Indeed, I started my PhD in a completely different subject, namely high energy neutrino experimental physics. Despite my deeply meditated decision of changing to quantum optics, I have very good memories of that period which lasted two years, and I feel grateful to the people that made it possible. When I started the present PhD, I had to decide between two possibilities: either study extensively one topic until it would be worth a PhD or, on the other hand, diversify, learn from different but connected topics, and get a general impression of the current trends in quantum optics. I think that the reader will see clearly that, wisely advised, I chose the second option. Get ready to embark on a trip passing through not only different matters, but also different places, from Munich to Valencia, where I have had the luck to work with people that I admire.

CONTENTS

I

OVERVIEW

In physics, the past two decades have been shocked by the emergence of quantum information. The promises of quantum computing have provided researchers from many different disciplines (computer science, of course, but very prominently solid state physics, quantum optics, and atomic and molecular physics) with a collective goal. In particular, the impact in quantum optics has been tremendous so that, for instance, the generation of squeezed light has gained new relevance for quantum technologies that require high levels of squeezing to generate entanglement levels high enough for the intended effects to appear (be it teleportation, encryption, or many other continuous-variables quantum protocols). By today, quantum technologies include devices capable of working in the strong coupling limit with unprecedented control and accuracy in a rapidly growing field. These new quantum devices are very diverse including cavity-QED [1], optical lattices [2, 3], trapped ions [4, 5], superconducting circuits [6, 7], quantum dots [8], atomic ensembles [9, 10], optomechanical devices [11–13], etc. Although this thesis is not a thesis on quantum information per se, the diversity of its contents is motivated precisely by this current trends in quantum optics, as it is dedicated to the study of three devices that are very relevant in the current framework: optical parametric oscillators (the standard source of squeezed and continuous-variable entangled light), optical microcavities arrays (which are a potential platform for simulating quantum many-body problems), and optomechanical cavities (one of the most promising hybrid devices nowadays). The three chosen devices have been studied under very different perspectives, implying that the physical models as well as the mathematical techniques used to study them have been different too.

In the following, I briefly describe the main content of each of the three parts[1].

- In the first part of the thesis we work with the optical parametric oscillator, which due to the quantum properties of the process behind its functioning, parametric down-conversion process, provides one of the paradigms for the study of non-classical states of light, as well as entanglement and squeezing. For detection and manipulation purposes, it is convenient to have the frequencies of the entangled down-converted fields degenerate, but as the conditions for the latter to occur are quite critical, additional locking techniques are needed, which usually degrade the entanglement levels. In this work, we propose a way to

[1] In Appendix I, according to the regulation, there is a summary in Spanish, one of the official languages of the Universitat de València.

achieve the desired frequency locking, while preserving good levels of entanglement. The technique we introduce requires just injecting the cavity with a laser, and is therefore less invasive than previous proposals which required, e.g., introducing a wave-plate in the cavity.

- In the second part the thesis, we study an array of dissipative tunnel-coupled cavities, each interacting with an incoherently pumped two-level emitter. These type of devices have been introduced as prototype setups for the study of quantum many-body physics with light. We will show that collective correlations among the different elements in the array build up and decay exponentially as the distance between the considered cavities tends to infinity for any dimension of the array. We also find that the lasing properties of the one emitter laser, which conforms the constituents of our model, arise in the system as a result of the emergence of collective photonic modes, even when the emitter and cavity are out of resonance.

- In the third and last part we study pattern formation in optomechanical cavities. Optomechanical systems have received a lot of attention in the last decades because they allow the generation of non-classical states of light and of the mechanical oscillations and also, through "cooling" processes, one can put a macroscopic object into his quantum fundamental state. As far as we know, up to now the proposed models only consider the interaction of few light modes with few mechanical modes. In this part we propose a multimode optomechanical model from which we predict the formation of periodic patterns and localized structures (cavity solitons) among other complex nonlinear phenomena. Also, we discuss realistic designs for its implementation.

II

ACTIVE LOCKING AND ENTANGLEMENT IN TYPE II OPTICAL PARAMETRIC OSCILLATORS

1. INTRODUCTION

1.1 Nonlinear optics and optical parametric oscillators

Nonlinear optics [14] is the study of the phenomena that occur as a consequence of a nonlinear response of a system to the strength of an optical field. This response can often be described by expressing the dipole moment per unit volume, or polarization $P(t)$, as a power series in the field strength $E(t)$,

$$P(t) = \epsilon_0 \left[\chi^{(1)} E(t) + \chi^{(2)} E(t)^2 + \chi^{(3)} E(t)^3 + \ldots \right], \tag{1.1}$$

where for the moment we will forget about the vector character of the field for simplicity.

The reason why the polarization plays a key role in the description of nonlinear optical phenomena is that time-varying polarization can act as the source of new components of the electromagnetic field which, for a lossless, dispersionless medium, will be governed by the wave equation:

$$\nabla^2 E - \frac{n^2}{c^2} \frac{\partial^2 E}{\partial t^2} = \frac{1}{\epsilon_0 c^2} \frac{\partial^2 P}{\partial t^2}, \tag{1.2}$$

where $\nabla^2 = \partial_x^2 + \partial_y^2 + \partial_z^2$ is the Laplacian.

Optical Parametric Oscillators (OPOs) are in essence optical cavities containing a second order nonlinear crystal, the so called noncentrosymmetric crystals that are crystals that do not display inversion symmetry. The nonlinear polarization that is created in such a crystal is given by $P(t) = \epsilon_0 \chi^{(2)} E(t)^2$. Let us now consider the circumstance in which the optical field incident upon a second-order nonlinear optical medium consists of two distinct frequency components, which we represent in the form:

$$E(t) = E_1 e^{-i\omega_1 t} + E_2 e^{-i\omega_2 t} + c.c. \tag{1.3}$$

and therefore, we find that the nonlinear polarization is given by:

$$P(t) = \sum_n P(\omega_n) \tag{1.4}$$

where the summation extends over frequencies ω_n, each one representing a process that can occur in a second order nonlinear crystal.

$$P(2\omega_1) = \epsilon_0 \chi^{(2)} E_1^2 e^{-2i\omega_1 t} + c.c. \quad \text{(SHG)}, \tag{1.5}$$

$$P(2\omega_2) = \epsilon_0 \chi^{(2)} E_2^2 e^{-2i\omega_2 t} + c.c. \quad \text{(SHG)}, \tag{1.6}$$

$$P(\omega_1 + \omega_2) = 2\epsilon_0 \chi^{(2)} E_1 E_2 e^{-i(\omega_1+\omega_2)t} + c.c. \quad \text{(SFG)}, \tag{1.7}$$

$$P(\omega_1 - \omega_2) = 2\epsilon_0 \chi^{(2)} E_1 E_2^* e^{-i(\omega_1-\omega_2)t} + c.c. \quad \text{(DFG)}, \tag{1.8}$$

$$P(0) = 2\epsilon_0 \chi^{(2)} \left(E_1 E_1^* + E_2 E_2^*\right) \quad \text{(OR)}. \tag{1.9}$$

Here we have labeled each expression by the name of the physical process that it describes, such as second-harmonic generation (SHG), sum-frequency generation (SFG), difference-frequency generation (DFG), and optical rectification (OR). However, typically no more than one of these frequency components will be present with any appreciable intensity in the radiation generated by the nonlinear optical interaction. The reason for this behaviour is that the nonlinear polarization can efficiently produce an output signal only if a certain phase-matching condition is satisfied (discussed next), and usually this condition cannot be satisfied for more than one frequency component of the nonlinear polarization. Operationally, one often chooses which frequency component will be radiated by properly selecting the polarization of the input radiation and the orientation and temperature of the nonlinear crystal. From a classical perspective, this is the main property of the second-order nonlinear crystals, frequency conversion, capable of providing coherent light at regions of the spectrum where lasers are not available.

In the OPO, the only relevant physical process is the difference-frequency generation (Fig. 1.1a), where the frequency of the generated wave is the difference of the those of the applied fields. The conservation of energy requires that for every photon that is created at the difference frequency $\omega_3 = \omega_1 - \omega_2$, a photon at the higher input frequency (ω_1) must be destroyed and a photon at the lower input frequency (ω_2) must be created (Fig. 1.1b). Thus, the lower frequency input field is amplified by the process of difference-frequency generation. For this reason, the process of difference-frequency generation is also known as optical parametric amplification. Two-photon emission can occur even if the ω_2 field is not applied, it can be generated through some initial fluctuations in the system, for example, a small amount of thermal photons. This process is known as parametric fluorescence or spontaneous parametric down-conversion. In this context, and from now on

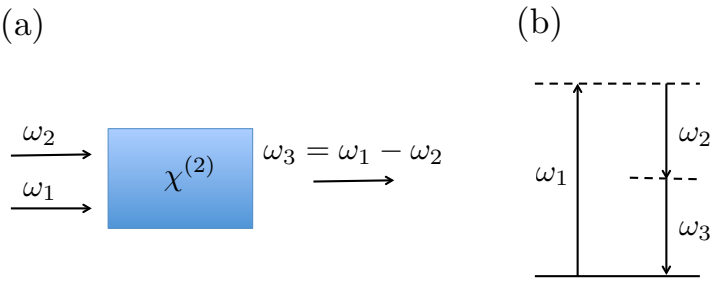

Fig. 1.1: Difference-frequency generation. (a) Geometry of the interaction. (b) Energy-level description.

in this thesis, the applied field frequency ω_1 is called the pump frequency, ω_p, while the spontaneously generated frequencies are called signal and idler, ω_s and ω_i, respectively, which satisfy the condition $\omega_p = \omega_s + \omega_i$.

The efficiency of the spontaneous parametric down-conversion descends dramatically when the wave vector mismatch ($\Delta k = k_i + k_s - k_p$) is not zero, which also can be seen as the violation of the conservation of the linear momentum. Perfect matching ($\Delta k = 0$) is difficult to achieve because of normal dispersion: the refractive index is an increasing function of frequency. If the three waves (pump, signal and idler) have the same polarization, the *phase matching condition* can be recasted as:

$$\frac{\omega_i}{\omega_s} = -\frac{n(\omega_p) - n(\omega_s)}{n(\omega_p) - n(\omega_i)} \tag{1.10}$$

The right hand side of this expression is always negative because, as $\omega_p = \omega_s + \omega_i$, it happens that $n(\omega_p) > \{n(\omega_s), n(\omega_i)\}$, so the phase matching condition cannot be fulfilled. Hence, in order to conserve linear momentum, the three waves involved in the down-conversion process cannot have the same polarization, and the medium must show birefringence, that is, different refractive index for two different directions of the linear polarization, called ordinary and extraordinary axes. In this scenario, if we assume that $\omega_s > \omega_i$, and that the extraordinary refractive index is larger than the ordinary one, $n_\mathrm{e}(\omega) > n_\mathrm{o}(\omega)$, and we align the crystal so that the pump wave is polarized along the ordinary axis and the signal along the extraordinary, the numerator of Eq. 1.10 becomes positive,

$$\frac{\omega_i}{\omega_s} = \frac{n_\mathrm{e}(\omega_s) - n_\mathrm{o}(\omega_p)}{n_\mathrm{o}(\omega_p) - n(\omega_i)} \tag{1.11}$$

We can distinguish then two types of processes. In a *type I* process both signal and idler have the same polarization (extraordinary with our conventions), while in a *type II* process they have orthogonal polarizations (extraordinary is the signal and ordinary the idler with our conventions). When signal and idler are frequency degenerate, the phase matching conditions are reduced to,

$$[\text{type I}] \quad n_{\text{e}}(\omega_0) = n_{\text{o}}(2\omega_0), \tag{1.12}$$

$$[\text{type II}] \quad n_{\text{e}}(\omega_0) = 2n_{\text{o}}(2\omega_0) - n_{\text{o}}(\omega_0). \tag{1.13}$$

Although there are methods for tuning the refractive indices felt by the different waves (e.g., angle tuning, which requires a precise angular orientation of the crystal with respect to the propagation direction of the incident light, or temperature tuning, relying on the strong dependence of birefringence on the crystal temperature), this conditions are quite critical, and it in practice it is impossible to work at frequency degeneracy without more elaborated locking techniques. Indeed, this fact will motivate the work that we have developed in this part of the thesis.

Now we are able to understand what *optical parametric oscillators* (OPOs) are: in essence, an optical resonator containing crystal with second order nonlinearity. This optimizes the frequency conversion process, i.e., if one pump photon is not transformed into a signal-idler pair when it first crosses the crystal, it is reflected back in order to have one more chance to be converted. Also, the presence of radiation at frequency ω_s and ω_i can stimulate the emission of additional photons at these frequencies, so signal and idler fields can build up to large intensities.

Consider the cavity resonances depicted in Fig. 1.2. Attending to the degeneracies that signal and idler may have in frequency and polarization, one can operate the OPO in four different regimes. For example, if we choose some cavity resonance $2\omega_0$ as the pump mode with ordinary polarization we could have: *(i) degenerate type I* OPO, in which signal and idler are indistinguishable and we talk then about a single mode, the signal mode, having frequency ω_0 and extraordinary polarization (Fig. 1.2a); *(ii) degenerate type II* OPO, in which the signal and idler have orthogonal polarizations but the same frequency (Fig. 1.2b); *(iii) non-degenerate type I*, in which the signal and idler have the same polarization but correspond to two opposite frequency sidebands around ω_0 (Fig. 1.2c) and *(iv) non-degenerate type II*, in which the signal and idler are distinguishable both in frequency and polarization (Fig. 1.2d).

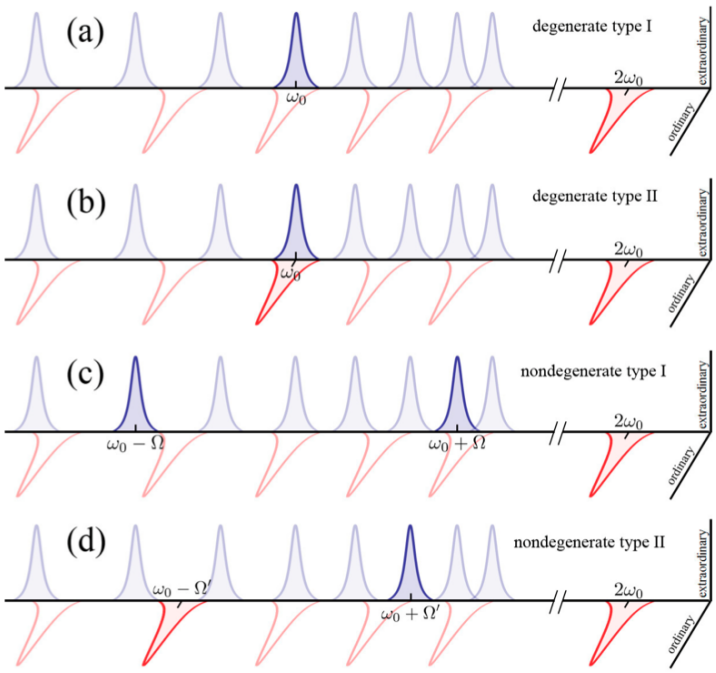

Fig. 1.2: (Taken from [15]) Down-conversion processes inside an optical cavity. In this example the structure of the resonances inside the cavity is such that the four types of processes can appear, as they are all energy conserving. Hence, when the pump field has frequency $2\omega_0$, signal and idler can be indistinguishable (a), or distinguishable in polarization (b), in frequency (c), or in them both (d).

1.2 Quantum correlations

Classically, the generation of the down-converted field requires the nonlinear gain to compensate for the cavity losses, what means that the OPO has to be pumped above a certain power threshold in order for signal and idler to start oscillating inside the cavity. Quantum-mechanically the situation is different; below threshold, the output field has zero mean amplitude but also exhibits small fluctuations. Above the threshold, the output field has nonzero mean amplitude and also exhibits small fluctuations. What really makes the OPO to play a major role in Quantum Optics is that these fluctuations are nonclassical [16].

In the following we are going to explain the basics of these nonclassical

states of light and how they apply to OPOs, and some notions of how it is possible to identify these states in a laboratory. For the full understanding of the following some notions of quantum mechanics are needed, which are given in Appendix A.

1.2.1 Squeezing

An important application of harmonic oscillators, e.g., the electromagnetic field, is *sensing*: The oscillator is put in contact with a system that we want to test, and some information about this gets encoded as phase or amplitude modulations in the oscillator. When any other source of technical noise is removed, that is, when the measurement equipment behaves basically as ideal, the *quantum noise* become the main limitation. It could happen that if the signal generated by the system that we want to study is tiny enough that is below the quantum noise level, we wouldn't see it. The solution to this problem are the squeezed states, where the noise of either the phase or the amplitude is decreased by increasing proportionally the other, as required by the uncertainty principle. Instead of phase and amplitude, whose corresponding quantum observables are very complicated, one usually talks about *quadratures*, which are both simple to measure and to handle theoretically.

Quadratures and phase-space picture of coherent states: It is well known that the concept of phase space in quantum mechanics is problematic owing the fact that the canonical variables $\hat{x}$ and $\hat{p}$ are incompatible, i.e. they do not commute (Appendix A). Thus, the state of a system is not well localized as a point in phase space as it is in classical mechanics. In order to explain this, we now introduce dimensionless versions of the position and momentum operators, the so-called quadrature operators

$$\hat{X} = (a^\dagger + a) \quad \text{and} \quad \hat{Y} = i(a^\dagger - a), \tag{1.14}$$

where $\hat{a}$ and $\hat{a}^\dagger$ are annihilation and creation operators for excitations of the harmonic oscillator (that is, photons in one particular mode of the electromagnetic field). They satisfy the commutation relation $\left[\hat{X}, \hat{Y}\right] = 2i$, so that defining the variance of an operator $\hat{A}$

$$V(A) = (\Delta A)^2 = \langle \hat{A}^2 \rangle - \langle \hat{A} \rangle^2, \tag{1.15}$$

the corresponding Heisenberg uncertainty relation is $\Delta X \Delta Y \geq 1$. States for which the equality of this relation achieved are called *minimum-uncertainty states*.

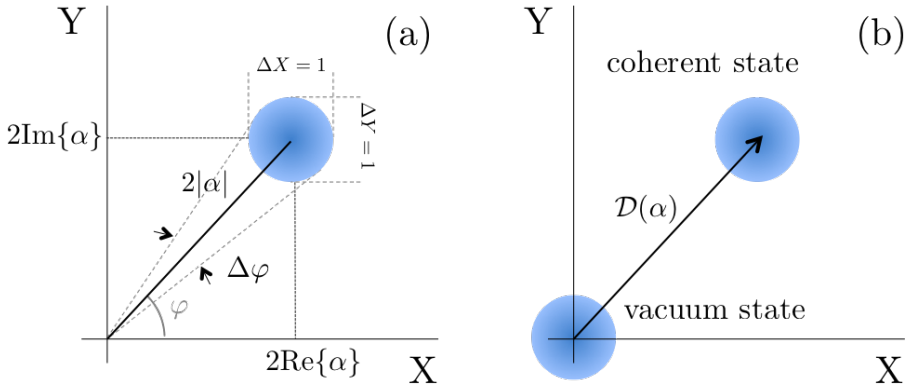

Fig. 1.3: (a) Phase-space portrait of a coherent state of amplitude $2|\alpha|$ and phase angle φ. $\Delta\varphi$ represents the phase uncertainty and $\Delta X = \Delta Y = 1$ the quadratures uncertainties. (b) A coherent state of aritrary amplitude can be generated by applying a displacement ($\mathcal{D}(\alpha)$) to the vacuum state. Note the error circle is the same of all coherent states.

Coherent states, introduced in Appendix A and labeled by a complex amplitude α, are a particular class of minimum-uncertainty states with $\Delta X = \Delta Y = 1$, and expectation values $\langle \hat{X} \rangle_\alpha = 2\mathrm{Re}\{\alpha\}$ and $\langle \hat{Y} \rangle_\alpha = 2\mathrm{Im}\{\alpha\}$. A coherent state may be represented pictorially then as in Fig. 1.3a, where the circle represents the "area of uncertainty" of the coherent state, the fluctuations being equal in all directions of phase space, its center located at distance $2|\alpha|$ from the origin and forming an angle $\varphi = \arctan\left(\mathrm{Im}\{\alpha\}/\mathrm{Re}\{\alpha\}\right)$ with respect to the position axis. Further, $\Delta\varphi$, in a qualitative sense, represents the phase uncertainty of the coherent state and it should be clear that $\Delta\varphi$ diminishes for increasing $|\alpha|$, the fluctuations in $\hat{X}$ and $\hat{Y}$ being independent of α and identical to those of the vacuum state. Indeed, for the vacuum state $|\alpha| = 0$, and its phase space representation is given in Fig. 1.3b, where it is evident that uncertainty in the phase is as large as possible, i.e. $\Delta\varphi = 2\pi$. The representation of any other coherent state $|\alpha\rangle$ is then obtained by displacing this uncertainty circle to the point $(2\mathrm{Re}\{\alpha\}, 2\mathrm{Im}\{\alpha\})$, and hence these states can be visualized as classical states carrying with them vacuum uncertainties (Appendix A).

It is going to be convenient to define a *general quadrature operator*

$$\hat{X}^\psi = \hat{X}\cos\psi + \hat{Y}\sin\psi = e^{-i\psi}\hat{a} + e^{i\psi}a^\dagger \tag{1.16}$$

which is the quadrature operator associated to a direction of phase space forming an angle ψ with respect to the position axis. We will denote the

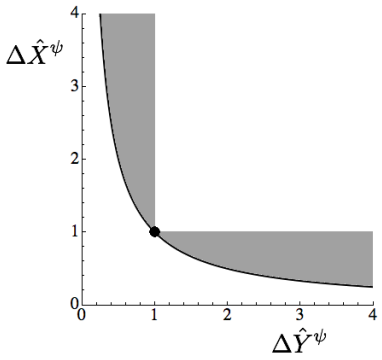

Fig. 1.4: Plot of ΔX versus ΔY for the minimum-uncertainty states. The dot marks a coherent state while the shaded region corresponds to the squeezed states.

quadrature defined along its orthogonal direction by $\hat{Y}^{\psi} = \hat{X}^{\psi+\pi/2}$. These pair of general quadratures satisfy the same relations as the ones defined in 1.14, in particular the commutation relation $\left[\hat{X}^{\psi}, \hat{Y}^{\psi}\right] = 2i$ and the uncertainty relation $\Delta X^{\psi} \Delta Y^{\psi} \geq 1$.

Squeezed states. There is a whole family of minimum-uncertainty states defined by $\Delta X^{\psi} \Delta Y^{\psi} = 1$. If we plot ΔX^{ψ} against ΔY^{ψ}, these minimum-uncertainty states lie on a hyperbola (Fig 1.4). Only points lying to the right of the hyperbola correspond to physical states. The minimum-uncertainty coherent state with $\Delta X^{\psi} = \Delta Y^{\psi}$ can be seen then a special case of a more general class of states which have reduced uncertainty in one quadrature at the expense of increased uncertainty in its orthogonal ($\Delta X^{\psi} \leq 1 \leq \Delta Y^{\psi}$). These states correspond to the shaded region in Fig. 1.4. Such states we shall call *squeezed states*, and they may be generated by using the unitary squeezing operator

$$\hat{S}(z) = \exp\left(\frac{z^*}{2}\hat{a}^2 - \frac{z}{2}\hat{a}^{\dagger 2}\right) \tag{1.17}$$

where $z = r\exp(i\theta)$ is called the *squeezing parameter*. Similarly to the displacement operator (Appendix A), this operator is unitary; hence, it can be generated by making the oscillator evolve with the Hamiltonian $\hat{H}_S = i\hbar(z^*\hat{a}^2 - z\hat{a}^{\dagger 2})/2T$ during a time T, which generates excitations in pairs, just as what happens in parametric down-conversion, and hence it is to be expected that OPOs can generate squeezed states of light.

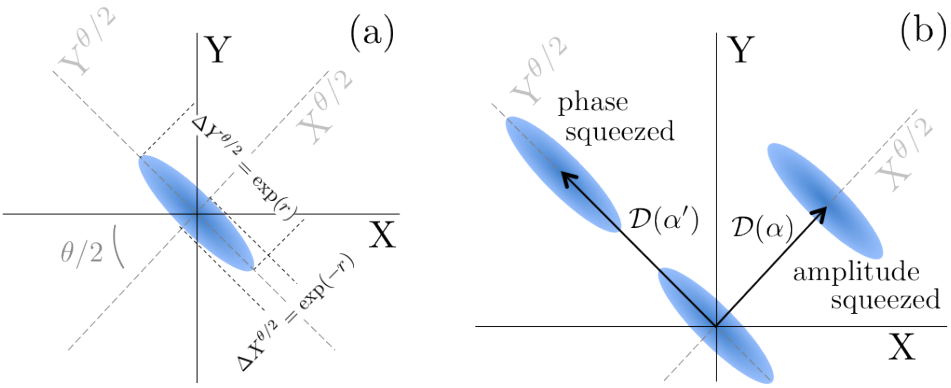

Fig. 1.5: (a) Phase space sketch of a squeezed vacuum state. (b) Applying displacements in the direction fo the squeezed or antisqueezed quadratures, one obtains amplitude of phase squeezed states, respectively

Using the Baker-Campbell-Haussdorf lemma we can apply it to the annihilation operator

$$\hat{S}^\dagger(z)\hat{a}\hat{S}(z) = \hat{a}\cosh r - e^{i\theta}\hat{a}^\dagger \sinh r. \tag{1.18}$$

In terms of quadratures, these expressions are easily rewritten as

$$\hat{S}^\dagger(z)\hat{X}^{\theta/2}\hat{S}(z) = e^{-r}\hat{X}^{\theta/2} \quad \text{and} \quad \hat{S}^\dagger(z)\hat{Y}^{\theta/2}\hat{S}(z) = e^{r}\hat{Y}^{\theta/2}, \tag{1.19}$$

so the squeezing appears along the $\theta/2$ direction, half the argument of the squeezing parameter.

Suppose now that before the *squeezing transformation* the state of the system was vacuum, which has the statistical properties $\langle \hat{X}^\psi \rangle = 0$ and $\Delta X^\psi = 1$ for all the ψ. After the transformation 1.19 the mean of any quadrature is still zero, but the uncertainty of the quadrature $\hat{X}^{\theta/2}$ has decreased to $\Delta X^{\theta/2} = \exp(-r)$, while that of quadrature $\hat{Y}^{\theta/2}$ has increased to $\Delta Y^{\theta/2} = \exp(r)$. Hence, in this case, the squeezing operator creates a minimum uncertainty squeezed state, that is, a state in which the uncertainty of one quadrature is reduced below the vacuum level, while the quadratures still satisfy the lower bound set by uncertainty relation.

The phase space sketch of this squeezed vacuum state is showed in Fig. 1.5a. The uncertainty circle associated to the vacuum state has turned into an ellipse, showing that the quadrature uncertainty along the $\theta/2$ direction of phase space is reduced. An amplitude squeezed state can be then created

by applying a subsequent displacement along the $\theta/2$ axis as shown in Fig. 1.5b. If the displacement is applied along the $(\theta+\pi)/2$ direction, then a phase squeezed state is obtained. As displacements do not change the uncertainty properties of the state, these amplitude or phase squeezed states are still minimum uncertainty states.

1.2.2 Entanglement

Quantum entanglement refers to correlations between two constituents of a system (e.g. individual particles) which cannot be explained via classical physics. In this case, a quantum state may be given for the system as a whole and it can not be factorized. One constituent cannot be fully described without considering the other(s), or in other way, the measurement of one constituent influences the rest of the system, even if their parts are causally separated. Naturally, this conclusion made uncomfortable the founding fathers of the modern concept of causality (Special Relativity) and in 1935, Einstein, Podolsky and Rosen (EPR [17]), came with an argument which was supposed to tumble down the foundations of quantum mechanics. However, John S. Bell presented in 1964 a measurable way of testing the EPR ideas against quantum mechanics, in particular proving that quantum mechanics and local-realistic theories provide different predictions for certain types of experiments. Even though, to date, no experiment has been capable of performing such a test without loopholes, the overwhelming evidence points out in the direction of quantum mechanics as the 'winner' of the debate. Hence, now the main efforts are used not in testing the non-locality of quantum mechanics, but in searching for applications that might be derived from it, for example the possibility of building quantum computers, where the key feature that lies behind its operation is quantum entanglement.

We say that two systems are entangled when they share correlations between non-commuting observables beyond what's classically permitted. For our purposes, it is enough to think about two harmonic oscillators (A and B) in a state in which both their positions and momenta share quantum mechanical correlations. Mathematically, we can express this in terms of variances; consider two orthogonal quadratures $\{\hat{X}_A^{\varphi_a}, \hat{Y}_A^{\varphi_a}\}$ and $\{\hat{X}_B^{\varphi_b}, \hat{Y}_B^{\varphi_b}\}$ for oscillators A and B, respectively; then their joint state is separable if and only if

$$W_{AB}^{\varphi_a\varphi_b} = V[(\hat{X}_A^{\varphi_a} - \hat{X}_B^{\varphi_b})/\sqrt{2}] + V[(\hat{Y}_A^{\varphi_a} + \hat{Y}_B^{\varphi_b})/\sqrt{2}] \geq 2 \tag{1.20}$$

for every $\varphi_{a,b}$. As we explain in Appendix A, coherent states are the quantum

mechanical states closest to a classical description. It is easy to check that for any coherent state one has $V[(\hat{X}_A^{\varphi_a} - \hat{X}_B^{\varphi_b})/\sqrt{2}] = V[(\hat{Y}_A^{\varphi_a} + \hat{Y}_B^{\varphi_b})/\sqrt{2}] = 1$ $\forall \varphi_{a,b}$, leading to $W_{AB}^{\varphi_a \varphi_b} = 2$, precisely the lower bound of the criterion. Hence, even if this criterion does not quantify the amount of entanglement present in the state (it offers just a way to prove whether a state is separable or not), in many instances one can interpret the level of violation of the separability condition as how strong the quantum correlations between the oscillators are, especially when the violation is very severe. Let us now explain how to generate a class of such entangled states.

Two mode squeezing operator. Note first that the conditions $V[(\hat{X}_A^{\varphi_a} - \hat{X}_B^{\varphi_b})/\sqrt{2}] < 1$ and $V[(\hat{Y}_A^{\varphi_a} + \hat{Y}_B^{\varphi_b})/\sqrt{2}] < 1$ are actually quite reminiscent of the quadrature squeezing that we introduced in the previous section, except for now the squeezing appears in a pair of joint quadratures. Let us call $\hat{a}$ and $\hat{b}$ the annihilation operators for the A and B harmonic oscillators, respectively. Consider the unitary operator

$$\hat{S}_{AB}(z) = \exp\left(z^* \hat{a}\hat{b} - z\hat{a}^\dagger \hat{b}^\dagger\right) \tag{1.21}$$

which we will call the *two-mode squeezing operator*. Similarly to the squeezing operator, this operator generates excitations in correlated pairs, but now in distinguishable modes; hence, we can expect entanglement to appear in type II OPOs, in which the down-converted pairs are distinguishable in polarization. Using the Baker-Campbell-Haussdorf lemma, the annihilation operators are easily transformed under the action of the two-mode squeezing operator as

$$\hat{S}_{AB}^\dagger(z)\hat{a}\hat{S}_{AB}(z) = \hat{a}\cosh r - e^{i\theta}\hat{b}^\dagger \sinh r, \tag{1.22a}$$

$$\hat{S}_{AB}^\dagger(z)\hat{b}\hat{S}_{AB}(z) = \hat{b}\cosh r - e^{i\theta}\hat{a}^\dagger \sinh r, \tag{1.22b}$$

where $z = r\exp(i\theta)$. By using these results, we can show that, in the state defined by the action of $\hat{S}_{AB}(z)$ on the two-mode vacuum state (*two-mode squeezed vacuum*), the variances read as:

$$V[(\hat{X}_A^{\theta/2} + \hat{X}_B^{\theta/2})/\sqrt{2}] = V[(\hat{Y}_A^{\theta/2} - \hat{Y}_B^{\theta/2})/\sqrt{2}] = \exp(-2r), \tag{1.23a}$$

$$V[(\hat{X}_A^{\theta/2} - \hat{X}_B^{\theta/2})/\sqrt{2}] = V[(\hat{Y}_A^{\theta/2} + \hat{Y}_B^{\theta/2})/\sqrt{2}] = \exp(2r), \tag{1.23b}$$

Hence, using the shorthand notation $W_{AB}^{\varphi_a \varphi_b} = W_{AB}^{\varphi}$ when $\varphi_a = \varphi_b = \varphi$, we have that $W_{AB}^{(\theta-\pi)/2} = 2\exp(-2r) < 2$ $\forall r > 0$. In particular, for $\theta = \pi$ and $r \to \infty$ we obtain a perfectly correlated state called EPR state,

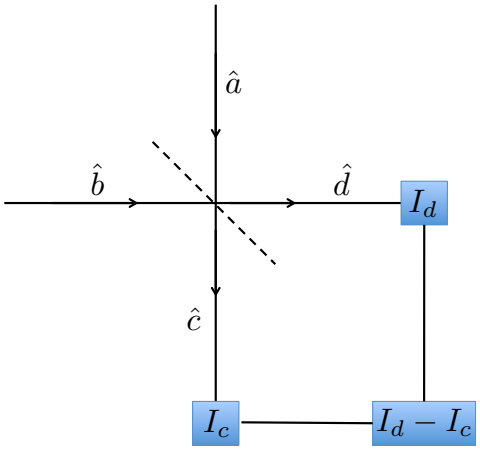

Fig. 1.6: Schematic of the balanced homodyne method for the detection squeezing. The field to be detected enters along $\hat{a}$ while a strong coherent field is injected along $\hat{b}$. The boxes in the lower left and upper right represent photo-detectors measuring the respective photo-currents. The box on the lower right represents a correlation device that subtracts the photo-currents.

because this state was the one used by EPR in their attempt to discredit quantum mechanics [17]. In such a state, the measurement of the position or the momentum of harmonic oscillator A would determine the position or momentum of B, respectively, even when these are causally separated. This is what Einstein called “spooky action at a distance”. He claimed that in order for any physical theory to be true it can’t violate causality. As EPR put forward, "if without in anyway disturbing a system, we can predict with certainty (i.e., with probability equal to unity), the value of a physical quantity, then there exists an element of physical reality corresponding to that quantity". In other words, the states should be determined from the beginning according to some hidden variables that the theory is not taking in to account, and therefore, the theory would be incomplete. Against this asseveration, one could say that the observer of B (Bob) would never know with certainty the value of its measurement, if the observer of A (Alice) doesn’t tell him, what would causally connect them. But, as mentioned above, the strongest and definitive argument are Bell inequalities, which in a very clever and testable way are able to rule out local hidden variable theories in favour of quantum theory.

1.2.3 Detection of quadrature squeezed light

Once we have explained what squeezed light is, the next question concerns how squeezing, and the quadratures in particular, can be detected. Here we explain the method known as *balanced homodyne detection*. The general idea behind the method consists in mixing in a 50/50 beam-splitter the field presumed to contain the squeezing with a strong coherent field, called the *local oscillator*. A scheme of the method is shown in Fig. 1.6. Mode a contains the single-mode field that is possibly squeezed. The local oscillator, b, contains an intense laser field which may be taken as a coherent state of amplitude β, and has the same spatio-temporal profile and polarization as the mode we want to detect (but orthogonal propagation direction). As mentioned, the beam-splitter is assumed to be 50/50 (hence the term *balanced* homodyne detection). In such case, assuming that the reflected beam suffers a $\pi/2$ phase shift, the input and output modes are related according to:

$$\hat{c} = \frac{1}{\sqrt{2}}(\hat{a} + i\hat{b}), \tag{1.24a}$$

$$\hat{d} = \frac{1}{\sqrt{2}}(\hat{b} + i\hat{a}). \tag{1.24b}$$

The last step consists in measuring the difference of the intensities recorded by detectors impinged by the output beams. Such a measurement is then sensitive to the photon-number difference operator

$$\hat{n}_{cd} = \hat{c}^\dagger\hat{c} - \hat{d}^\dagger\hat{d} = i(\hat{a}^\dagger\hat{b} - \hat{a}\hat{b}^\dagger). \tag{1.25}$$

Assuming the b mode is in a coherent state $|\beta\rangle$, where $\beta = |\beta|\, e^{i\psi}$, the moments of the measured signal will be proportional to

$$\langle \hat{n}_{cd} \rangle = |\beta| \left\langle \hat{X}^\varphi \right\rangle, \tag{1.26a}$$

$$\left\langle \hat{n}_{cd}^2 \right\rangle = |\beta|^2 \left[\left\langle \hat{X}^{\varphi 2} \right\rangle + \frac{\left\langle \hat{a}^\dagger\hat{a} \right\rangle}{|\beta|^2} \right]. \tag{1.26b}$$

where $\hat{X}^\varphi = e^{-i\varphi}\hat{a} + e^{i\varphi}a^\dagger$ and $\varphi = \psi + \pi/2$. By changing ψ, we can measure an arbitrary quadrature of the field. In the limit of a strong local oscillator ($|\beta|^2 \gg \langle \hat{a}^\dagger\hat{a} \rangle$), the variance of the measured signal is proportional then to

$$V(\hat{n}_{cd}) = |\beta|\, V(\hat{X}^\varphi), \tag{1.27}$$

and hence allows to determine whether there is squeezing in the input field.

Even though this picture offers all the basic ingredients that one has to understand about light detection, it is in a sense far from how light is observed in real experiments. For a given cavity mode (with well defined spatial profile and polarization), there exist a continuum of modes outside the cavity. In order to measure one of such modes, we have to prepare the local oscillator with exactly the same polarization and spatial profile. Moreover, its frequency determines the center frequency around which the detection is performed, and is normally tuned to the frequency of the field oscillating inside the cavity. On the other hand, the photons on the detector will generate cascades of electrons that will be translated as a continuous current in time (*photocurrent*). In the temporal domain, it is possible to show that the latter is saturated by noise at all times, and hence it is convenient to work in Fourier space. In particular, by properly processing the measured data with a power spectrum, one has access to the so-called spectral covariance matrix [18], which reads

$$V^{\varphi}(\Omega) = \mathbb{1} + 2\gamma_{\mathrm{s}} \lim_{t\to\infty} \int_{-\infty}^{+\infty} dt' M(t,t') e^{-\mathrm{i}\Omega t'}. \tag{1.28}$$

with $2\gamma_s$ the leaking rate of photons out of the cavity, and

$$M = \begin{pmatrix} \langle : \delta\hat{X}^{\varphi}(t)\delta\hat{X}^{\varphi}(t+t') : \rangle & \frac{1}{2}\langle \{ : \delta\hat{X}^{\varphi}(t), \delta\hat{Y}^{\varphi}(t+t') : \} \rangle \\ \frac{1}{2}\langle \{ : \delta\hat{X}^{\varphi}(t), \delta\hat{Y}^{\varphi}(t+t') : \} \rangle & \langle : \delta\hat{Y}^{\varphi}(t)\delta\hat{Y}^{\varphi}(t+t') : \rangle \end{pmatrix} \tag{1.29}$$

where $\delta\hat{A} = \hat{A} - \langle\hat{A}\rangle$, :: denotes normal order of the operators, and $\{A, B\} = AB + BA$ is the anti-commutator. The diagonal of 1.28 encodes the so called *noise spectra* of the quadratures $V(\hat{X}^{\varphi}, \Omega)$ and $V(\hat{Y}^{\varphi}, \Omega)$, which signal the presence of squeezing whenever one of them is smaller than 1. It is important not to confuse the *noise frequency* Ω with the optical frequencies. The spectral convariance matrix and the noise spectra in particular, will be the main objects of study in this part of the thesis.

1.2.4 Quantum correlations in OPOs.

Type I OPOs (Fig. 1.2), in which both signal and idler are linearly polarized within the extraordinary axis of the crystal, hold the record for quadrature noise reduction or single-mode squeezing (more than 90% below vacuum fluctuations [19–23]); this is manifested in the mode at the degenerate frequency $\omega_{\mathrm{s}} = \omega_{\mathrm{i}} \sim \omega_0$, but squeezing is large only when working close to threshold [24]. The squeezed light generated has been a basic resource in the field

of high-precision measurements, helping to overcome the standard quantum limit imposed by vacuum fluctuations [25–28]. On the other hand, mixing the output of two degenerate type I OPOs on a beam splitter, one can obtain a pair of entangled beams (in the continuous-variable of Einstein-Podolsky-Rosen—EPR—sense [17]), what makes these devices a basic resource also for continuous-variable quantum information protocols [29, 30]; however, these method for the generation of entanglement requires the nonlinear cavities to be precisely locked to generate indistinguishable down-converted fields whose squeezing occurrs in two orthogonal quadratures, what introduces one level of complexity .

Of more interest for our current work are type II OPOs (Fig. 1.2), that is, OPOs in which signal and idler have orthogonal polarizations (one following the extraordinary crystal axis, and the other one the ordinary). Just as the degenerate type I OPO, there is an observable which shows large squeezing levels only close to threshold, which in this case corresponds to the sum of the phases of signal and idler; in other words, close to threshold, type II OPOs show signal-idler phase anticorrelations beyond the standard quantum limit [31–33]. But type II OPOs have one more interesting property: they are invariant under changes of the signal-idler phase difference, what means that quantum noise is able to act on this variable without bounds, making it diffuse and eventually completely undetermined (in the quantum mechanical sense) [15, 31, 34–37]. But invoking now the Heisenberg principle, a completely undetermined phase difference between signal and idler allows for complete noise reduction in their intensity difference (its canonically conjugate variable); indeed, signal and idler become twin beams above threshold, that is, their amplitudes are perfectly correlated [34, 38, 39]. Hence, non-degenerate OPOs show (ideally) perfect amplitude correlations at any pumping level above threshold, and large phase anti-correlations close to threshold, which means that close to this point they should be in a high-quality continuous-variable entangled state [32, 33, 35]. From a quantum optics perspective, this means that below threshold OPOs should emit a two-mode squeezed vacuum state, while above threshold they would emit a displaced one (a 'bright' EPR state).

However, there are two issues that make above-threshold type II OPOs not practical as an EPR source, specially from a detection point of view. First, the phase–matching conditions ensuring that it is the frequency degenerate process the one with larger gain (lowest threshold) are quite critical, and hence, signal and idler will have different frequencies in general;

for example, in the case of ref. [40], where the authors are able to make the frequency difference between signal and idler as small as 150 kHz for a cavity with 8 GHz free spectral range and 6 MHz linewidth, variations of the cavity length on the order of the nanometer can make the oscillation frequencies jump to frequencies separated by several times the free spectral range (mode hopping); second, the signal-idler phase-difference is chosen at random at any realization and diffuses with time (rather fast close to threshold), making it virtually impossible to capture the squeezed quadratures in a balanced homodyne detection scheme. Hence, additional signal-idler phase locking techniques are required.

The pioneering example of such locking techniques was introduced by Fabre and collaborators [41, 42]. Their idea consisted in embedding in the cavity a $\lambda/4$ plate with its fast axis misaligned with respect to the extraordinary axis of the nonlinear crystal. The plate introduces a coupling between the signal and idler modes which breaks the phase invariance of the OPO, and it was then shown in [41] that in a given region of the parameter space (in particular of the detunings of signal and idler) the frequencies of signal and idler get locked to ω_0; this OPO is known as the *self–phase–locked OPO*, and was already studied experimentally in [42]. Note that, as mentioned, this self–locking effect is accomplished by breaking the phase symmetry of the OPO, and hence, one should expect a degradation of the signal–idler intensity correlations, or, equivalently, of the noncritical squeezing induced by spontaneous polarization symmetry breaking described in [43]. For example, in ref. [42] the intensity–difference fluctuations showed 89% quantum noise reduction prior to the introduction of the plate, while after obtaining frequency degeneracy through the self–phase–locking mechanism this value fell down to a more humble 65%.

1.3 Actively–phase–locked OPO model

In this part of the thesis we study an alternative locking mechanism which consists in the injection of a laser at frequency degeneracy ω_0, what seems less invasive and more controllable than the introduction of a $\lambda/4$ wave plate; we will call *actively–phase–locked OPO* to such OPO configuration. We will show that, from a classical point of view, this injection locks the signal and idler frequencies to the desired ω_0 for any injection level when pumping below threshold; above threshold, the injection has to surpass some minimum value in order to achive locking. From a quantum point of

view, we prove that such technique generates a pair of frequency-degenerate and bright signal-idler beams, which share high levels of continuous-variable entanglement in a very wide region of the parameter space. Since these modes are frequency degenerate, their entanglement is equivalent to having phase-squeezing in two other modes with orthogonal polarization, what makes its detection straightforward with usual balance homodyning. This locking technique is reminiscent of a previous work developed in our group in the context of frequency-degenerate type I OPOs tuned to the first family of transverse modes [15, 36, 37, 44, 45], in which it was proposed injecting a TEM_{10} mode at the subharmonic to lock the phase-difference between the down-converted modes with opposite orbital angular momentum.

For definiteness and without loss of generality, we consider a symmetric Fabry-Perot cavity with a thin nonlinear crystal in its center ($z = 0$), where the electric field operator at the relevant frequencies can be approximately written as $\hat{\mathbf{E}}(\mathbf{r}, t) = \sum_{j=\mathrm{p,s,i}} \hat{\mathbf{E}}_j^{(+)}(\mathbf{r}, t) + \mathrm{H.c.}$, with

$$\hat{\mathbf{E}}_j^{(+)}(\mathbf{r}_\perp, t) = \mathrm{i}\sqrt{\frac{2\hbar\omega_j}{\pi\varepsilon_0 n_j L_j w_j^2}} e^{-r^2/w_j^2} \boldsymbol{\varepsilon}_j \hat{a}_j e^{-(1+\delta_{j\mathrm{p}})\mathrm{i}\omega_0 t}, \tag{1.30}$$

where ω_j, n_j, L_j, w_j, $\boldsymbol{\varepsilon}_j$ and $\delta_{j\mathrm{p}}$ are, respectively, the resonance frequency, refractive index, optical cavity length, transverse spot size at the cavity waist, polarization of the corresponding mode and the Kronecker delta; $\mathbf{r}_\perp = (x, y)$ is the transverse coordinate vector, with $r = |\mathbf{r}_\perp|$, and we have assumed there are TEM_{00} transverse modes resonating at the three relevant frequencies, giving rise to the simple Gaussian transverse profile of the expression. Finally, let us remark that, starting from the Schrodinger picture, we have moved to a new picture rotating at frequency $2\omega_0$ for the pump, and ω_0 for signal and idler, so that the the annihilation ($\hat{a}_j$) and creation ($\hat{a}_j^\dagger$) operators in the expression are time-independent, and satisfy canonical commutation relations $[\hat{a}_j, \hat{a}_l^\dagger] = \delta_{jl}$.

The resonance scheme and polarization of the fields are sketched in Figure 1.7: the pump is polarized within the ordinary axis of the crystal and resonates at frequency $2\omega_0$, while signal and idler are polarized within the extraordinary and ordinary axis by convention, respectively, and resonate at frequencies $\omega_{\mathrm{s,i}} = \omega_0 + \delta_{\mathrm{s,i}}$, with $|\delta_{\mathrm{s,i}}|$ smaller or on the order of their cavity linewidth $\gamma_{\mathrm{s}} = \gamma_{\mathrm{i}}$, taken equal for signal and idler for simplicity. Apart from pumping the cavity with a laser at frequency $2\omega_0$ with ordinary polarization, we inject an external laser field at the degenerate frequency ω_0 with polarization $\boldsymbol{\varepsilon}_{\mathrm{L}} = e^{-\mathrm{i}\theta_{\mathrm{L}}}\mathbf{e}_{\mathrm{e}} \cos\varphi_{\mathrm{L}} + e^{\mathrm{i}\theta_{\mathrm{L}}}\mathbf{e}_{\mathrm{o}} \sin\varphi_L$, where $\mathbf{e}_{\mathrm{e}}$ and $\mathbf{e}_{\mathrm{o}}$

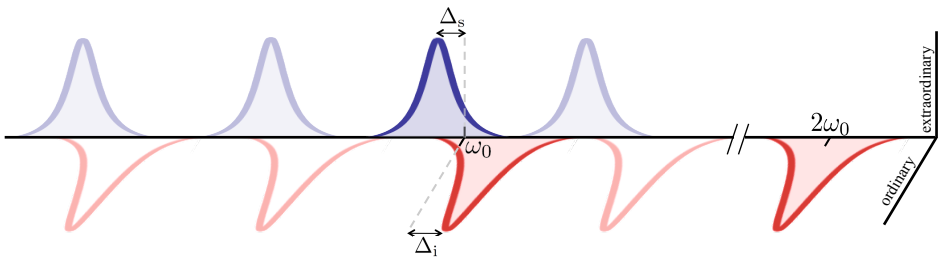

Fig. 1.7: Resonance scheme of the type II OPO in which we propose to obtain frequency degeneracy via an external injection at the degenerate frequency ω_0.

are unit vectors following, respectively, the extraordinary and ordinary axes of the crystal. In this last expression the angles θ_L and φ_L are used to parametrize any polarization (Jones) vector, and although they don not have an immediate geometric meaning, they can be easily related to the polarization ellipse parameters, see [15]. Including cavity losses through the usual Lindblad terms, the master equation governing the evolution of the state of the system reads [46]

$$\frac{d\hat{\rho}}{dt} = \frac{1}{i\hbar}\left[\hat{H}, \hat{\rho}\right] + \sum_{j=p,s,i} \gamma_j (2\hat{a}_j \hat{\rho} \hat{a}_j^\dagger - \hat{a}_j^\dagger \hat{a}_j \hat{\rho} - \hat{\rho} \hat{a}_j^\dagger \hat{a}_j), \tag{1.31}$$

where, in the rotating picture we are working on, the Hamiltonian can be written as $\hat{H} = \hat{H}_0 + \hat{H}_{PDC} + \hat{H}_{inj}$, with

$$\hat{H}_0 = \hbar\delta_s \hat{a}_s^\dagger \hat{a}_s + \hbar\delta_i \hat{a}_i^\dagger \hat{a}_i, \tag{1.32a}$$

$$\hat{H}_{PDC} = i\hbar\chi(\hat{a}_p \hat{a}_s^\dagger \hat{a}_i^\dagger - \hat{a}_p^\dagger \hat{a}_s \hat{a}_i), \tag{1.32b}$$

$$\hat{H}_{inj} = \sum_{j=p,s,i} i\hbar(\mathcal{E}_j \hat{a}_j^\dagger - \mathcal{E}_j^* \hat{a}_j). \tag{1.32c}$$

In this expression, the detunings are defined as $\delta_j = \omega_j - \omega_0$; the down-conversion coupling reads

$$\chi = \sqrt{\frac{9\hbar\omega_p\omega_s\omega_i}{2\pi^3\varepsilon_0 n_p n_s n_i L_p L_s L_i}} \frac{l_c w_p w_s w_i \chi^{(2)}_{oee}(\omega_p; \omega_s, \omega_i)}{w_p^2 w_s^2 + w_s^2 w_i^2 + w_i^2 w_p^2}, \tag{1.33}$$

where l_c and $\chi^{(2)}_{oee}(\omega_p; \omega_s, \omega_i)$ are, respectively, the crystal's length and its relevant nonlinear susceptibility coefficient [15]; the damping rates are related

to the (intensity) transmisivities of the mirror at the corresponding frequency, $\mathcal{T}_j$, by $\gamma_j = c\mathcal{T}_j/4L_j$; and the injection parameters can be approximately written in terms of the power of the injected lasers at frequencies $2\omega_0$ and ω_0 as $\mathcal{E}_\mathrm{p} = \sqrt{\gamma_\mathrm{p} P_{2\omega_0}/\hbar\omega_0}$, $\mathcal{E}_\mathrm{s} = \sqrt{2\gamma_\mathrm{s} P_{\omega_0}/\hbar\omega_0}e^{\mathrm{i}(\phi_\mathrm{L}-\theta_\mathrm{L})}\cos\varphi_\mathrm{L}$, and $\mathcal{E}_\mathrm{i} = \sqrt{2\gamma_\mathrm{s} P_{\omega_0}/\hbar\omega_0}e^{\mathrm{i}(\phi_\mathrm{L}+\theta_\mathrm{L})}\sin\varphi_\mathrm{L}$, where ϕ_L is the phase of the ω_0 injection relative to the $2\omega_0$ injection, whose phase we take as a reference.

In order to get analytical insight, and following previous works [15, 36, 37, 44, 45], we map this master equation to a set of stochastic Langevin equations by using the positive P coherent representation [47]. This is an exact procedure by which an independent complex stochastic variable is associated to each bosonic operator, that is, $\{\alpha_j, \alpha_j^+\}_{j=\mathrm{p,s,i}}$ to $\{\hat{a}_j, \hat{a}_j^\dagger\}_{j=\mathrm{p,s,i}}$; quantum expectation values of any operator are then obtained as stochastic averages by replacing the bosonic operators by their corresponding stochastic variable in the normally-ordered version of the operator. It is not difficult to show that the stochastic Langevin equations associated to the master equation 1.31 read

$$\dot{\alpha}_\mathrm{p} = \mathcal{E}_\mathrm{p} - \gamma_\mathrm{p}\alpha_\mathrm{p} - \chi\alpha_\mathrm{s}\alpha_\mathrm{i}, \tag{1.34a}$$
$$\dot{\alpha}_\mathrm{p}^+ = \mathcal{E}_\mathrm{p} - \gamma_\mathrm{p}\alpha_\mathrm{p}^+ - \chi\alpha_\mathrm{s}^+\alpha_\mathrm{i}^+, \tag{1.34b}$$
$$\dot{\alpha}_\mathrm{s} = \mathcal{E}_\mathrm{s} - (\gamma_\mathrm{s} + \mathrm{i}\delta_\mathrm{s})\,\alpha_\mathrm{s} + \chi\alpha_\mathrm{p}\alpha_\mathrm{i}^+ + \sqrt{\chi\alpha_\mathrm{p}}\xi(t), \tag{1.34c}$$
$$\dot{\alpha}_\mathrm{s}^+ = \mathcal{E}_\mathrm{s} - (\gamma_\mathrm{s} - \mathrm{i}\delta_\mathrm{s})\,\alpha_\mathrm{s}^+ + \chi\alpha_\mathrm{p}^+\alpha_\mathrm{i} + \sqrt{\chi\alpha_\mathrm{p}^+}\xi^+(t), \tag{1.34d}$$
$$\dot{\alpha}_\mathrm{i} = \mathcal{E}_\mathrm{i} - (\gamma_\mathrm{s} + \mathrm{i}\delta_\mathrm{i})\,\alpha_\mathrm{i} + \chi\alpha_\mathrm{p}\alpha_\mathrm{s}^+ + \sqrt{\chi\alpha_\mathrm{p}}\xi^*(t), \tag{1.34e}$$
$$\dot{\alpha}_\mathrm{i}^+ = \mathcal{E}_\mathrm{i} - (\gamma_\mathrm{s} - \mathrm{i}\delta_\mathrm{i})\,\alpha_\mathrm{i}^+ + \chi\alpha_\mathrm{p}^+\alpha_\mathrm{s} + \sqrt{\chi\alpha_\mathrm{p}^+}[\xi^+(t)]^*, \tag{1.34f}$$

where we have defined independent complex noises $\xi(t)$ and $\xi^+(t)$, with zero mean, and only non-zero two-time correlators

$$\langle\xi(t)\xi^*(t')\rangle = \left\langle\xi^+(t)[\xi^+(t')]^*\right\rangle = \delta(t-t'). \tag{1.35a}$$

In order to reduce the number of parameters of the problem, we now make some changes of variables; in particular, we redefine time as $\tau = \gamma_\mathrm{s}t$, the stochastic amplitudes as

$$\beta_\mathrm{p} = \frac{\chi}{\gamma_\mathrm{s}}\alpha_\mathrm{p}, \quad \beta_\mathrm{s,i} = \frac{\chi}{\sqrt{\gamma_\mathrm{s}\gamma_\mathrm{p}}}\alpha_\mathrm{s,i}\exp(\pm\mathrm{i}\theta_\mathrm{L}), \tag{1.36}$$

and the noises as

$$\eta(\tau) = \frac{1}{\sqrt{\gamma_\mathrm{s}}}\xi(t), \quad \eta^+(\tau) = \frac{1}{\sqrt{\gamma_\mathrm{s}}}\xi^+(t), \tag{1.37}$$

which satisfy the statistical properties (1.35), but now respect to the dimensionless time τ,

$$\langle \eta(\tau)\eta^*(\tau')\rangle = \left\langle \eta^+(\tau)[\eta^+(\tau')]^*\right\rangle = \delta(\tau-\tau'). \tag{1.38}$$

In terms of these new variables, the Langevin equations read

$$\dot{\beta}_{\rm p} = \kappa\left(\sigma - \beta_{\rm p} - \beta_{\rm s}\beta_{\rm i}\right), \tag{1.39a}$$
$$\dot{\beta}^+_{\rm p} = \kappa\left(\sigma - \beta^+_{\rm p} - \beta^+_{\rm s}\beta^+_{\rm i}\right), \tag{1.39b}$$
$$\dot{\beta}_{\rm s} = \varepsilon_{\rm s}e^{{\rm i}\phi_{\rm L}} - (1+{\rm i}\Delta_{\rm s})\,\beta_{\rm s} + \beta_{\rm p}\beta^+_{\rm i} + g\sqrt{\beta_{\rm p}}\exp({\rm i}\theta_{\rm L})\eta(\tau), \tag{1.39c}$$
$$\dot{\beta}^+_{\rm s} = \varepsilon_{\rm s}e^{-{\rm i}\phi_{\rm L}} - (1-{\rm i}\Delta_{\rm s})\,\beta^+_{\rm s} + \beta^+_{\rm p}\beta_{\rm i} + g\sqrt{\beta^+_{\rm p}}\exp(-{\rm i}\theta_{\rm L})\eta^+(\tau), \tag{1.39d}$$
$$\dot{\beta}_{\rm i} = \varepsilon_{\rm i}e^{{\rm i}\phi_{\rm L}} - (1+{\rm i}\Delta_{\rm i})\,\beta_{\rm i} + \beta_{\rm p}\beta^+_{\rm s} + g\sqrt{\beta_{\rm p}}\exp(-{\rm i}\theta_{\rm L})\eta^*(\tau), \tag{1.39e}$$
$$\dot{\beta}^+_{\rm i} = \varepsilon_{\rm i}e^{-{\rm i}\phi_{\rm L}} - (1-{\rm i}\Delta_{\rm i})\,\beta^+_{\rm i} + \beta^+_{\rm p}\beta_{\rm s} + g\sqrt{\beta^+_{\rm p}}\exp({\rm i}\theta_{\rm L})[\eta^+(\tau)]^+, \tag{1.39f}$$

where we have defined the parameters

$$\kappa = \frac{\gamma_{\rm p}}{\gamma_{\rm s}}, \quad \sigma = \frac{\chi\mathcal{E}_{\rm p}}{\gamma_{\rm s}\gamma_{\rm p}}, \quad \Delta_j = \delta_j/\gamma_{\rm s}, \tag{1.40}$$
$$\varepsilon_{\rm s,i} = \frac{g}{\gamma_{\rm s}}|\mathcal{E}_{\rm s,i}|, \quad g = \frac{\chi}{\sqrt{\gamma_{\rm s}\gamma_{\rm p}}}.$$

Note that the Fokker-Planck equation associated to this Langevin system is independent of $\theta_{\rm L}$, and hence, we can remove the phase factors in the noises. In other words, the system is only sensitive to the parameter $\varphi_{\rm L}$ of the injection's polarization.

In order to get some analytic insight, we are going to simplify the problem to what we will call *symmetric configuration* of the actively–phase–locked OPO: we assume the detunings to be opposite, that is, $\Delta_{\rm s} = -\Delta_{\rm i} = \Delta$, and inject with $\varphi_{\rm L} = \pi/4$ (arbitrary polarization ellipse along the $\pm 45^o$ axis), so that signal and idler get equally pumped, $|\varepsilon_{\rm s}| = |\varepsilon_{\rm i}| \equiv \sqrt{\mathcal{I}}$. Moreover, we consider the signal injection in phase with the pump injection ($\phi_{\rm L} = 0$, usually denoted by amplification regime). Even though in real experiments such a symmetric configuration is in general not possible to achieve, since it requires unfeasible fine-tuning, it will allow us to get analytical results from which understanding the physics. Moreover, in the last section we will show numerically that all the conclusions obtained for this case, can be extrapolated to the non-symmetric case. Taking all these consideration

into account, and further performing an adiabatic elimination of the pump ($\dot{\beta}_\mathrm{p} = \dot{\beta}_\mathrm{p}^+ = 0$) under the assumption $\gamma_\mathrm{p} \gg \gamma_\mathrm{s}$, we can reduce our model equations (1.39) to

$$\dot{\beta}_\mathrm{s} = \sqrt{\mathcal{I}} - (1 + \mathrm{i}\Delta)\,\beta_\mathrm{s} + \tilde{\beta}_\mathrm{p}\beta_\mathrm{i}^+ + g\sqrt{\tilde{\beta}_\mathrm{p}}\eta(\tau), \tag{1.41a}$$

$$\dot{\beta}_\mathrm{s}^+ = \sqrt{\mathcal{I}} - (1 - \mathrm{i}\Delta)\,\beta_\mathrm{s}^+ + \tilde{\beta}_\mathrm{p}^+\beta_\mathrm{i} + g\sqrt{\tilde{\beta}_\mathrm{p}^+}\eta^+(\tau), \tag{1.41b}$$

$$\dot{\beta}_\mathrm{i} = \sqrt{\mathcal{I}} - (1 - \mathrm{i}\Delta)\,\beta_\mathrm{i} + \tilde{\beta}_\mathrm{p}\beta_\mathrm{s}^+ + g\sqrt{\tilde{\beta}_\mathrm{p}}\eta^*(\tau), \tag{1.41c}$$

$$\dot{\beta}_\mathrm{i}^+ = \sqrt{\mathcal{I}} - (1 + \mathrm{i}\Delta)\,\beta_\mathrm{i}^+ + \tilde{\beta}_\mathrm{p}^+\beta_\mathrm{s} + g\sqrt{\tilde{\beta}_\mathrm{p}^+}[\eta^+(\tau)]^*, \tag{1.41d}$$

with

$$\tilde{\beta}_\mathrm{p} = \sigma - \beta_\mathrm{s}\beta_\mathrm{i}, \quad \tilde{\beta}_\mathrm{p}^+ = \sigma - \beta_\mathrm{s}^+\beta_\mathrm{i}^+.$$

These are the final equations that will model quantum-mechanically our system in the remaining of the chapter. In the following, we will be interested in the quantum properties of the down-converted field; in particular, it will be useful to define a polarization mode

$$\boldsymbol{\varepsilon}_\theta = [e^{-\mathrm{i}(\theta_\mathrm{L}-\theta)}\mathbf{e}_\mathrm{e} + e^{\mathrm{i}(\theta_\mathrm{L}-\theta)}\mathbf{e}_\mathrm{o}]/\sqrt{2}, \tag{1.42}$$

where we include the phase θ_L of the injection beam for later convenience, with associated annihilation operator

$$\hat{a}_\theta = [e^{\mathrm{i}(\theta_\mathrm{L}-\theta)}\hat{a}_\mathrm{s} + e^{-\mathrm{i}(\theta_\mathrm{L}-\theta)}\hat{a}_\mathrm{i}]/\sqrt{2}, \tag{1.43}$$

and quadratures

$$\hat{X}_\theta^\psi = e^{-\mathrm{i}\psi}\hat{a}_\theta + e^{\mathrm{i}\psi}\hat{a}_\theta^\dagger. \tag{1.44}$$

The stochastic amplitude associated to this mode is

$$\beta_\theta = [e^{-\mathrm{i}(\theta)}\beta_\mathrm{s} + e^{\mathrm{i}(\theta)}\beta_\mathrm{i}]/\sqrt{2}, \tag{1.45}$$

so that defining the corresponding normalized stochastic quadratures

$$x_\theta^\psi = e^{-\mathrm{i}\psi}\beta_\theta + e^{\mathrm{i}\psi}\beta_\theta^+, \tag{1.46}$$

the covariance matrix 1.28 of that polarization mode reads

$$V_\theta^\psi(\omega) = \mathbb{1} + \frac{2}{g^2}\lim_{\tau\to\infty}\int_{-\infty}^{+\infty} d\tau' M(t,t')e^{-\mathrm{i}\omega\tau'}, \tag{1.47}$$

where we have defined the dimensionless noise frequency $\omega = \Omega/\gamma_s$ and the two-time correlation matrix

$$M = \begin{pmatrix} \langle \delta x_\theta^\psi(\tau)\delta x_\theta^\psi(\tau+\tau')\rangle & \frac{1}{2}\langle\{\delta x_\theta^\psi(\tau), \delta y_\theta^\psi(\tau+\tau')\}\rangle \\ \frac{1}{2}\langle\{\delta x_\theta^\psi(\tau), \delta y_\theta^\psi(\tau+\tau')\}\rangle & \langle \delta y_\theta^\psi(\tau)\delta y_\theta^\psi(\tau+\tau')\rangle \end{pmatrix} \tag{1.48}$$

Note that the bra-c-kets denote in this expression stochastic averages, which within the positive P representation are indeed equivalent to the expectation value of the corresponding normally-ordered quantum operators.

This is the object that will be analyzed in this part of the thesis, and from which we will study the quantum properties of the system. In order to find it, we need to solve the stochastic equations (1.41), what we will do by applying the so-called *linearization technique*. In such approach, one first finds the classical stable configuration of the system, and then considers quantum fluctuations around it. Under the assumption that the classical solution is a strong attractor, so that quantum noise is strongly damped, one can assume quantum fluctuations to be of order g, and neglect terms of order g^2 or larger in the (1.41), obtaining a linear system easy to solve (assuming in addition that the normalized stochastic noises are of order g^0 at most). Hence, we see that this method requires a clear understanding of the classical behaviour of the system, and this is precisely what we will study in the next section.

2. CLASSICAL BEHAVIOUR. FREQUENCY LOCKING.

As mentioned above, in this section we are interested in the classical behavior of the system, our main intention being proving that signal–idler frequency–locking can be accomplished with this scheme. The classical evolution equations are retrieved from the Langevin equations 1.41 by setting the noises to zero, and replacing the 'plus' amplitudes by the corresponding complex-conjugate ones, what is equivalent to making a coherent-state ansatz for the state of the optical modes. This leads to:

$$\dot{\beta}_{\rm s} = \sqrt{\mathcal{I}} - (1 + {\rm i}\Delta)\,\beta_{\rm s} + (\sigma - \beta_{\rm s}\beta_{\rm i})\beta_{\rm i}^{*}, \tag{2.1a}$$

$$\dot{\beta}_{\rm i} = \sqrt{\mathcal{I}} - (1 - {\rm i}\Delta)\,\beta_{\rm i} + (\sigma - \beta_{\rm s}\beta_{\rm i})\beta_{\rm s}^{*}. \tag{2.1b}$$

These equations have the symmetry $\{\beta_{\rm s} \to \beta_{\rm i}^{*}, \beta_{\rm i} \to \beta_{\rm s}^{*}\}$, what suggests looking for symmetric stationary solutions of the type

$$\bar{\beta}_{\rm s} = \bar{\beta}_{\rm i}^{*} = \sqrt{I}\exp({\rm i}\varphi). \tag{2.2}$$

Note that whenever this solution exists (and is stable), the classical down–converted field emitted by the OPO will be

$$\bar{\mathbf{E}}_{\rm DC}^{(+)}(\mathbf{r}_{\perp},t) = {\rm i}\sqrt{\frac{2\hbar\omega_{\rm s} I}{\pi\varepsilon_0 n_{\rm s} L_{\rm s} w_{\rm s}^2 g}}\, e^{-r^2/w_{\rm s}^2}(e^{-{\rm i}(\theta_{\rm L}-\varphi)}\mathbf{e}_{\rm e} + e^{{\rm i}(\theta_{\rm L}-\varphi)}\mathbf{e}_{\rm o})e^{-{\rm i}\omega_0 t}, \tag{2.3}$$

where we have taken the expectation value of (1.30) and made the correspondence $\langle\hat{a}_{\rm s,i}(t)\rangle = \exp(\mp{\rm i}\theta_{\rm L})\beta_{\rm s,i}(t)/g$. As expected, when the stationary solutions are stable ($\beta_{\rm s,i}(t) = \bar{\beta}_{\rm s,i}$), this corresponds to a field oscillating at the degenerate frequency ω_0. Moreover, the polarization of this field (which is always within the $\pm 45^{o}$ axis) can always be chosen as linear by selecting a proper $\theta_{\rm L}$ tuned to φ. Note that we have taken $\omega_{\rm s}/n_{\rm s}L_{\rm s}w_{\rm s}^2 = \omega_{\rm i}/n_{\rm i}L_{\rm i}w_{\rm i}^2$ for simplicity. In the remaining of this section we study the conditions under which this solution exists and is stable.

It is completely trivial to show from (2.1) that the intensity I of the symmetric solution satisfies the third order polynomial

$$\mathcal{I} = [(I + 1 - \sigma)^2 + \Delta^2]I, \tag{2.4}$$

while its phase φ is uniquely determined from I as

$$\varphi = \arg\{I + 1 - \sigma - \mathrm{i}\Delta\}. \tag{2.5}$$

The polynomial (2.4) sometimes has a single positive definite solution, while sometimes its three roots are positive definite (see Figures 2.1 and 2.2). By solving the equation $\partial\mathcal{I}/\partial I = 0$, it is simple to show that the turning points $I_\pm$ have the expression

$$I_\pm = \frac{2}{3}(\sigma - 1) \pm \frac{1}{3}\sqrt{(\sigma - 1)^2 - 3\Delta^2} \tag{2.6}$$

and hence, they exist only for $\sigma > 1 + \sqrt{3}\Delta$. For $\sigma \leq 1 + \sqrt{3}\Delta$ the solution is therefore single–valued.

In order to analyze the stability of this symmetric solution, we will change to a new polarization basis

$$\boldsymbol{\varepsilon}_\mathrm{b} = \frac{1}{\sqrt{2}}[e^{-\mathrm{i}(\theta_\mathrm{L}-\varphi)}\mathbf{e}_\mathrm{e} + e^{\mathrm{i}(\theta_\mathrm{L}-\varphi)}\mathbf{e}_\mathrm{o}],\ \ \boldsymbol{\varepsilon}_\mathrm{d} = \frac{1}{\sqrt{2}\mathrm{i}}[e^{-\mathrm{i}(\theta_\mathrm{L}-\varphi)}\mathbf{e}_\mathrm{e} - e^{\mathrm{i}(\theta_\mathrm{L}-\varphi)}\mathbf{e}_\mathrm{o}], \tag{2.7}$$

where $\boldsymbol{\varepsilon}_\mathrm{b}$ corresponds to the polarization mode excited by the symmetric solution (2.2) and $\boldsymbol{\varepsilon}_\mathrm{d}$ to its orthogonal, that is, to the bright and dark modes of the system. The corresponding coherent amplitudes are written as

$$\beta_\mathrm{b} = \frac{1}{\sqrt{2}}(e^{-\mathrm{i}\varphi}\beta_\mathrm{s} + e^{\mathrm{i}\varphi}\beta_\mathrm{i}),\ \ \beta_\mathrm{d} = \frac{\mathrm{i}}{\sqrt{2}}(e^{-\mathrm{i}\varphi}\beta_\mathrm{s} - e^{\mathrm{i}\varphi}\beta_\mathrm{i}), \tag{2.8}$$

and satisfy the evolution equations

$$\dot{\beta}_\mathrm{b} = \sqrt{2\mathcal{I}}\cos\varphi - \beta_\mathrm{b} - \Delta\beta_\mathrm{d} + (\sigma - \beta_\mathrm{b}^2/2 - \beta_\mathrm{d}^2/2)\beta_\mathrm{b}^*, \tag{2.9a}$$

$$\dot{\beta}_\mathrm{d} = \sqrt{2\mathcal{I}}\sin\varphi - \beta_\mathrm{d} + \Delta\beta_\mathrm{b} + (\sigma - \beta_\mathrm{b}^2/2 - \beta_\mathrm{d}^2/2)\beta_\mathrm{d}^*. \tag{2.9b}$$

In this new basis the symmetric solution reads

$$\bar{\beta}_\mathrm{b} = \sqrt{2I}, \qquad \bar{\beta}_\mathrm{d} = 0, \tag{2.10}$$

and its associated stability matrix is

$$\mathcal{L} = \begin{bmatrix} -1 - 2I & \sigma - I & -\Delta & 0 \\ \sigma - I & -1 - 2I & 0 & -\Delta \\ \Delta & 0 & -1 & \sigma - I \\ 0 & \Delta & \sigma - I & -1 \end{bmatrix}. \tag{2.11}$$

The characteristic polynomial of this stability matrix can be factorized into two second order polynomials, namely $P_{\mathrm{I}}(\lambda) = (\lambda + 1 + \sigma)^2 + \Delta^2 - I^2$ and $P_{\mathrm{II}}(\lambda) = (\lambda + 1 - \sigma + 2I)^2 + \Delta^2 - I^2$. The bifurcation diagrams for the different parameter regions are shown in Figures 2.1 and 2.2; now we discuss them in depth.

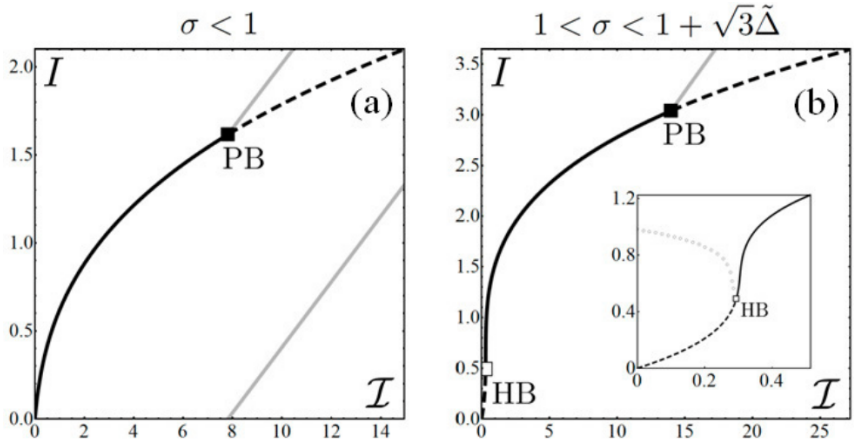

Fig. 2.1: (Caption valid also for Figure 2.2) Bifurcation diagrams of the type II OPO with an injected signal at the degenerate frequency, for the symmetric configuration $\Delta_{\mathrm{s}} = -\Delta_{\mathrm{i}} \equiv \Delta$ and $\varepsilon_{\mathrm{s}} = \varepsilon_{\mathrm{i}} \equiv \sqrt{\mathcal{I}}$; the value $\Delta = 0.6$ is chosen for all the figures (the same behavior is found for any other choice), while we set σ to 0.5 in (a), 1.98 in (b), 2.09 in 2.2.(a), and 2.8 in 2.2.(b). The black lines correspond to the intensity I of the stationary symmetric solution (2.2), the solid or dashed character of the lines meaning that this solution is stable or unstable, respectively. The upper and lower grey solid lines correspond to the values of $|\bar{\beta}_{\mathrm{b}}|^2/2$ and $|\bar{\beta}_{\mathrm{d}}|^2/2$, respectively, that is to half the intensity of the bright and dark (only showed in the $\sigma < 1$ case) modes; these lines have been found numerically, and show how above the pitchfork bifurcation (marked as PB in the figures) the symmetric solution (2.2) becomes unstable, and a new asymmetric solution is born. As explained in the text, for $\sigma > 1$ it is possible to find periodic solutions connecting the $\mathcal{I} = 0$ axis with the Hopf bifurcation (marked as HB in the figures); we have checked numerically that this periodic orbits exist, and moreover they are "symmetric", that is, $\beta_{\mathrm{s}}(t) = \beta_{\mathrm{i}}^*(t)$.

Let us start by studying the instabilities predicted by the first polynomial, whose roots are given by

$$\lambda_{\pm}^{\mathrm{I}} = -(1 + \sigma) \pm \sqrt{I^2 - \Delta^2}. \tag{2.12}$$

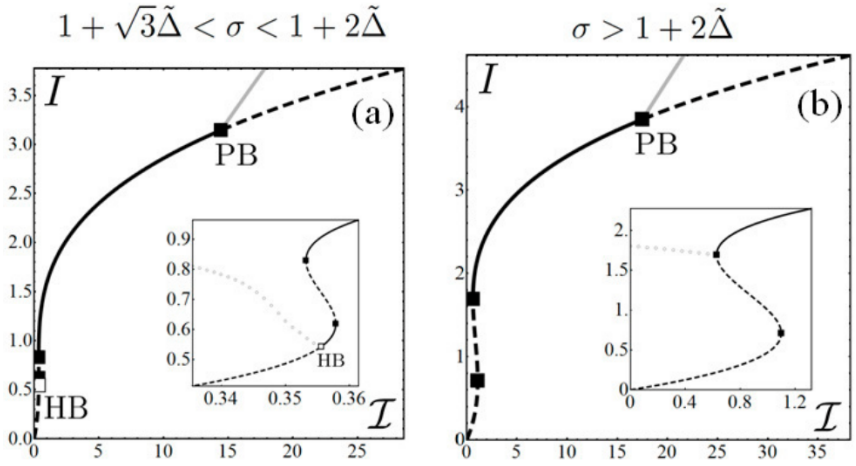

Fig. 2.2: The grey circles correspond to the mean value of $|\beta_s|^2$ (half the sum between its maximum and its minimum of oscillation). Note that there exist regions where stable stationary solutions and periodic orbits coexist, and that after the Hopf bifurcation is extinguished ($\sigma > 1 + 2\Delta$) the periodic orbits are connected directly to the upper turning point of the S–shaped curve.

Therefore, the condition $\mathrm{Re}\{\lambda_{\pm}^{\mathrm{I}}\} = 0$ can only be satisfied for

$$I = \sqrt{(1+\sigma)^2 + \Delta^2} \equiv I_{\mathrm{PB}}. \tag{2.13}$$

The fact that the instability appears without imaginary part in the $\lambda_{\pm}^{\mathrm{I}}$, and it is located in the upper branch of the S–shaped curve ($I_{\mathrm{PB}} > I_+$ for any value of the parameters), signals that it corresponds to a Pitchfork bifurcation where a non-symmetric stationary solution $\{\bar{\beta}_s = \sqrt{I_s}\exp(\mathrm{i}\varphi_s), \bar{\beta}_i = \sqrt{I_i}\exp(\mathrm{i}\varphi_i)\}$ with $I_s \neq I_i$ borns (as we have checked numerically, see the grey lines in Figures 2.1 and 2.2). This bifurcation is similar to the one introduced in [44], where we study the effects of a signal injection in the two-transverse-mode DOPO, and can be understood as a switching on of the dark mode. However, note that in this case the fluctuations of the bright and dark modes are not decoupled below threshold—see the linear stability matrix (2.11)—, what physically means that the quantum properties of the dark mode at the bifurcation will be very different from those of the dark mode in [44], and hence no perfect squeezing is likely to be found.

As for the second polynomial, its roots are given by

$$\lambda_{\pm}^{\mathrm{II}} = \sigma - 1 - 2I \pm \sqrt{I^2 - \Delta^2}. \tag{2.14}$$

Note that $\lambda_{\pm}^{\mathrm{II}} = 0$ for $I = I_{\pm}$, that is, the turning points of the S–shaped curve correspond to bifurcation points. It is then simple to check (for example numerically) that the whole middle branch connecting this instability points is unstable (see Figures 2.2a,b).

But $\lambda_{\pm}^{\mathrm{II}}$ has yet one more instability when

$$I = \frac{\sigma - 1}{2} \equiv I_{\mathrm{HB}}. \tag{2.15}$$

At this instability the eigenvalues become purely imaginary, in particular, $\lambda_{\pm}^{\mathrm{II}} = \pm \mathrm{i}\omega_{\mathrm{HB}}$ with $\omega_{\mathrm{HB}} = \sqrt{\Delta^2 - (\sigma-1)^2/4}$, and hence it corresponds to a Hopf bifurcation. Note that I_{HB} is negative for $\sigma < 1$, while ω_{HB} becomes imaginary for $\sigma > 1 + 2\Delta$, and hence the Hopf bifurcation only exists in the region $1 < \sigma < 1 + 2\Delta$. It is simple to check that I_{HB} is always below I_{PB} and I_-; in particular, it borns at $I = 0$ for $\sigma = 1$, and climbs the $\mathcal{I} - I$ curve as σ increases until it dies at $I = I_-$ for $\sigma = 1 + 2\Delta$ (see Figures 2.1b and 2.2a,b). The portion of the curve with $I < I_{\mathrm{HB}}$ is unstable, and no stationary solutions can be found there, as the stable states correspond in this case to periodic orbits (as we have checked numerically, see Figures 2.1b and 2.2a,b). This is also quite intuitive because when no injection is present, that is, for $\mathcal{I} = 0$, we know that the stable states of the OPO above threshold are the ones with the signal and idler beams oscillating at the non-degenerate frequencies $\omega_{\mathrm{s}} = \omega_0 + \Delta$ and $\omega_{\mathrm{i}} = \omega_0 - \Delta$, which in the picture we are working on means $\{\beta_{\mathrm{s}}(\tau) \propto \exp(-\mathrm{i}\Delta\tau), \beta_{\mathrm{i}}(\tau) \propto \exp(\mathrm{i}\Delta\tau)\}$.

This analysis proves that there exist regions in the parameter space where the frequencies of the signal and idler beams are locked to the degenerate one, and hence active–locking can be a good alternative to the self–locking technique already proposed for type II OPOs [41, 42].

From now on we will center our analysis in the Hopf bifurcation, which is the natural locking point of the system for $1 < \sigma < 1 + 2\Delta$, since by increasing the injection parameter $\mathcal{I}$ from zero, it is the point where signal and idler start oscillating at the same frequency.

3. QUANTUM ANALYSIS: SQUEEZING AND ENTANGLEMENT PROPERTIES.

3.1 Linearization of the Langevin equations

In this section we analyze the quantum properties of the system. The exhaustive analysis performed in our article [48] has shown that the strongest quantum correlations above the threshold ($\sigma > 1$) are achieved at the Hopf bifurcation, what is natural, since this is the point where the coherent part of the frequency-degenerate field is the smallest. For simplicity and in order to save space, we will particularize our quantum analysis to this point.

Let us start by rewriting the Langevin equations of the system in the bright-dark basis defined in (2.7). The corresponding stochastic amplitudes are given by

$$\beta_{\rm b} = \frac{1}{\sqrt{2}}(e^{-{\rm i}\varphi}\beta_{\rm s} + e^{{\rm i}\varphi}\beta_{\rm i}), \qquad \beta_{\rm d} = \frac{\rm i}{\sqrt{2}}(e^{-{\rm i}\varphi}\beta_{\rm s} - e^{{\rm i}\varphi}\beta_{\rm i}), \tag{3.1a}$$

$$\beta_{\rm b}^{+} = \frac{1}{\sqrt{2}}(e^{{\rm i}\varphi}\beta_{\rm s}^{+} + e^{-{\rm i}\varphi}\beta_{\rm i}^{+}), \qquad \beta_{\rm d}^{+} = -\frac{\rm i}{\sqrt{2}}(e^{{\rm i}\varphi}\beta_{\rm s}^{+} - e^{-{\rm i}\varphi}\beta_{\rm i}^{+}), \tag{3.1b}$$

and satisfy the Langevin equations:

$$\begin{aligned}\dot{\beta}_{\rm b} =& \sqrt{2\mathcal{I}}\cos\varphi - \beta_{\rm b} - \Delta\beta_{\rm d} + (\sigma - \beta_{\rm b}^2/2 - \beta_{\rm d}^2/2)\beta_{\rm b}^{+} \\ &+ g\sqrt{\sigma - \beta_{\rm b}^2/2 - \beta_{\rm d}^2/2}\eta_{\rm b}(\tau),\end{aligned} \tag{3.2a}$$

$$\begin{aligned}\dot{\beta}_{\rm b}^{+} =& \sqrt{2\mathcal{I}}\cos\varphi - \beta_{\rm b}^{+} - \Delta\beta_{\rm d}^{+} + (\sigma - \beta_{\rm b}^{+2}/2 - \beta_{\rm d}^{+2}/2)\beta_{\rm b} \\ &+ g\sqrt{\sigma - \beta_{\rm b}^{+2}/2 - \beta_{\rm d}^{+2}/2}\eta_{\rm b}^{+}(\tau),\end{aligned} \tag{3.2b}$$

$$\begin{aligned}\dot{\beta}_{\rm d} =& \sqrt{2\mathcal{I}}\sin\varphi - \beta_{\rm d} + \Delta\beta_{\rm b} + (\sigma - \beta_{\rm b}^2/2 - \beta_{\rm d}^2/2)\beta_{\rm d}^{+} \\ &+ g\sqrt{\sigma - \beta_{\rm b}^2/2 - \beta_{\rm d}^2/2}\eta_{\rm d}(\tau),\end{aligned} \tag{3.2c}$$

$$\begin{aligned}\dot{\beta}_{\rm d}^{+} =& \sqrt{2\mathcal{I}}\sin\varphi - \beta_{\rm d}^{+} + \Delta\beta_{\rm b}^{+} + (\sigma - \beta_{\rm b}^{+2}/2 - \beta_{\rm d}^{+2}/2)\beta_{\rm d} \\ &+ g\sqrt{\sigma - \beta_{\rm b}^{+2}/2 - \beta_{\rm d}^{+2}/2}\eta_{\rm d}^{+}(\tau),\end{aligned} \tag{3.2d}$$

where

$$\eta_{\rm b}(\tau) = \frac{1}{\sqrt{2}}[e^{-{\rm i}\varphi}\eta(\tau) + e^{{\rm i}\varphi}\eta^*(\tau)], \tag{3.3a}$$

$$\eta_{\rm d}(\tau) = \frac{\rm i}{\sqrt{2}}[e^{-{\rm i}\varphi}\eta(\tau) - e^{{\rm i}\varphi}\eta^*(\tau)], \tag{3.3b}$$

$$\eta_{\rm b}^+(\tau) = \frac{1}{\sqrt{2}}[e^{{\rm i}\varphi}\eta^+(\tau) + e^{-{\rm i}\varphi}\eta^{+*}(\tau)], \tag{3.3c}$$

$$\eta_{\rm d}^+(\tau) = -\frac{\rm i}{\sqrt{2}}[e^{{\rm i}\varphi}\eta^+(\tau) - e^{-{\rm i}\varphi}\eta^{+*}(\tau)], \tag{3.3d}$$

behave as real, independent noises.

These are a set of nonlinear differential equations with multiplicative noise, which can only be analyzed numerically without further approximations. In order to find analytical results, and as we advanced at the end of the first section, we perform one of such approximations, the well-known linearization approach. The method starts by writing the stochastic amplitudes as the classical solutions ($\bar\beta_j$) plus quantum fluctuations (b_j) as

$$\beta_{\rm b} = \bar\beta_{\rm b} + b_{\rm b}, \tag{3.4a}$$

$$\beta_{\rm b}^+ = \bar\beta_{\rm b}^* + b_{\rm b}^+, \tag{3.4b}$$

$$\beta_{\rm d} = \bar\beta_{\rm d} + b_{\rm d}, \tag{3.4c}$$

$$\beta_{\rm d}^+ = \bar\beta_{\rm d}^* + b_{\rm d}^+, \tag{3.4d}$$

where $\bar\beta_{\rm b} = \sqrt{2I}$ and $\bar\beta_{\rm d} = 0$. Assuming that the quantum fluctuations and noises are of order g and 1, respectively, we can now linearize the equations to first order in g, obtaining the system

$$\dot{\mathbf{b}} = \mathcal{L}\mathbf{b} + g\sqrt{\sigma - I}\boldsymbol{\eta}(\tau), \tag{3.5}$$

where

$$\mathbf{b} = {\rm col}(b_{\rm b}, b_{\rm b}^+, b_{\rm d}, b_{\rm d}^+), \qquad \text{and} \qquad \boldsymbol{\eta}(\tau) = {\rm col}[\eta_{\rm b}(\tau), \eta_{\rm b}^+(\tau), \eta_{\rm d}(\tau), \eta_{\rm d}^+(\tau)]. \tag{3.6}$$

In order to solve this linear system we resort to the eigensystem of the linear stability matrix $\mathcal{L}$, which we can find analytically. In particular, since this matrix is not hermitian, it possess a bi-orthonormal eigensystem defined by

$$\mathcal{L}\mathbf{v}_j = \lambda_j\mathbf{v}_j, \qquad \mathcal{L}^\dagger\mathbf{u}_j = \lambda_j^*\mathbf{u}_j, \qquad \mathbf{u}_j^\dagger\mathbf{v}_l = N_j\delta_{jl}; \tag{3.7}$$

The analytic form for of the eigenvectors and eigenvalues depends on whether I is smaller or larger than $|\Delta|$. From (2.15) and the discussion after, it is clear that $I \leq \Delta$ at the Hopf bifurcation, and hence, this is the case that we present here. The eigenvalues read

$$\lambda_1 = -1 - \sigma - \mathrm{i}\sqrt{\Delta^2 - I^2}, \tag{3.8a}$$
$$\lambda_2 = -1 - \sigma + \mathrm{i}\sqrt{\Delta^2 - I^2}, \tag{3.8b}$$
$$\lambda_3 = -1 + \sigma - 2I - \mathrm{i}\sqrt{\Delta^2 - I^2}, \tag{3.8c}$$
$$\lambda_4 = -1 + \sigma - 2I + \mathrm{i}\sqrt{\Delta^2 - I^2}, \tag{3.8d}$$

with corresponding eigenvectors ($\phi = \arctan\sqrt{\Delta^2/I^2 - 1} \in [0, \pi/2]$)

$$\mathbf{v}_1 = \mathrm{col}(e^{\mathrm{i}\phi/2}, -e^{\mathrm{i}\phi/2}, -e^{-\mathrm{i}\phi/2}, e^{-\mathrm{i}\phi/2}), \tag{3.9a}$$
$$\mathbf{v}_2 = \mathrm{col}(e^{-\mathrm{i}\phi/2}, -e^{-\mathrm{i}\phi/2}, -e^{\mathrm{i}\phi/2}, e^{\mathrm{i}\phi/2}), \tag{3.9b}$$
$$\mathbf{v}_3 = \mathrm{col}(e^{\mathrm{i}\phi/2}, e^{\mathrm{i}\phi/2}, -e^{-\mathrm{i}\phi/2}, -e^{-\mathrm{i}\phi/2}), \tag{3.9c}$$
$$\mathbf{v}_4 = \mathrm{col}(e^{-\mathrm{i}\phi/2}, e^{-\mathrm{i}\phi/2}, -e^{\mathrm{i}\phi/2}, -e^{\mathrm{i}\phi/2}), \tag{3.9d}$$

and

$$\mathbf{u}_1 = \mathrm{col}(e^{-\mathrm{i}\phi/2}, -e^{-\mathrm{i}\phi/2}, e^{\mathrm{i}\phi/2}, -e^{\mathrm{i}\phi/2}), \tag{3.10a}$$
$$\mathbf{u}_2 = \mathrm{col}(e^{\mathrm{i}\phi/2}, -e^{\mathrm{i}\phi/2}, e^{-\mathrm{i}\phi/2}, -e^{-\mathrm{i}\phi/2}), \tag{3.10b}$$
$$\mathbf{u}_3 = \mathrm{col}(e^{-\mathrm{i}\phi/2}, e^{-\mathrm{i}\phi/2}, e^{\mathrm{i}\phi/2}, e^{\mathrm{i}\phi/2}), \tag{3.10c}$$
$$\mathbf{u}_4 = \mathrm{col}(e^{\mathrm{i}\phi/2}, e^{\mathrm{i}\phi/2}, e^{-\mathrm{i}\phi/2}, e^{-\mathrm{i}\phi/2}), \tag{3.10d}$$

and normalizations

$$N_1 = -N_2 = N_3 = -N_4 = 4\mathrm{i}\sin\phi = 4\mathrm{i}\sqrt{1 - \frac{I^2}{\Delta^2}}. \tag{3.11}$$

Once the eigensystem is known, we solve the equations by defining the projections $c_j(\tau) = \mathbf{u}_j^\dagger \mathbf{b}(\tau)$, which evolve according to

$$\dot{c}_j = \lambda_j c_j + g\sqrt{\sigma - I}\,\mathbf{u}_j^\dagger \boldsymbol{\eta}(\tau), \tag{3.12}$$

and have therefore the long time term solution ($\tau \gg -\mathrm{Re}\{\lambda_j\}^{-1}\ \forall j$)

$$c_j(\tau) = g\sqrt{\sigma - I}\int_0^\tau d\tau_1 e^{\lambda_j(\tau-\tau_1)}\mathbf{u}_j^\dagger \boldsymbol{\eta}(\tau_1). \tag{3.13}$$

Now, as the projections $c_j(t)$ depend ultimately on the noises $\boldsymbol{\eta}(t)$, whose two-time correlators we know, see 1.38, we can easily calculate their correlation functions which, again in the long time term limit ($\tau, \tau' \gg -\mathrm{Re}\{\lambda_j\}^{-1}\ \forall j$) read

$$\langle c_j(\tau)c_l(\tau')\rangle = -\frac{g^2(\sigma - I)(\mathbf{u}_j^\dagger \mathbf{u}_l^*)}{\lambda_j + \lambda_l} \begin{cases} \exp[\lambda_l(\tau' - \tau)] & \tau' > \tau \\ \exp[\lambda_j(\tau - \tau')] & \tau' < \tau \end{cases}, \tag{3.14}$$

leading to the spectra

$$\tilde{C}_{jl}(\omega) = \int_{-\infty}^{+\infty} d\tau' e^{-\mathrm{i}\omega\tau} \langle c_j(\tau)c_l(\tau+\tau')\rangle = \frac{g^2(\sigma - I)D_{jl}}{(\lambda_j + \mathrm{i}\omega)(\lambda_l - \mathrm{i}\omega)}, \tag{3.15}$$

where we have defined the matrix D with elements $D_{jl} = \mathbf{u}_j^\dagger \mathbf{u}_l^*$, which has the simple form

$$D = \begin{pmatrix} 4I/\tilde{\Delta} & 4 & 0 & 0 \\ 4 & 4I/\tilde{\Delta} & 0 & 0 \\ 0 & 0 & 4I/\tilde{\Delta} & 4 \\ 0 & 0 & 4 & 4I/\tilde{\Delta} \end{pmatrix}. \tag{3.16}$$

Together with the also simple expression for the eigenvalues (3.8), these spectra will allow us to find the analytic results we are seeking for.

Note that since the eigenvalues are complex, the spectra are complex too for $j = l$, what means that the projections $c_j(\tau)$ cannot correspond in general to any physical observable such as, e.g., the quadratures of two modes with a given polarization. However, it is simple to show that simple linear combinations of them are indeed proportional to the quadratures of two modes with polarization $\boldsymbol{\varepsilon}_{\varphi\pm\pi/4}$ (remember the notation 1.42); in particular, we have

$$c_1 + c_2 = 2\mathrm{i}\sqrt{1 + I/\Delta}\,\delta y_{\varphi-\pi/4}, \tag{3.17a}$$

$$c_1 - c_2 = -2\sqrt{1 - I/\Delta}\,\delta y_{\varphi+\pi/4}, \tag{3.17b}$$

$$c_3 + c_4 = 2\sqrt{1 + I/\Delta}\,\delta x_{\varphi-\pi/4}, \tag{3.17c}$$

$$c_3 - c_4 = 2\mathrm{i}\sqrt{1 - I/\Delta}\,\delta x_{\varphi+\pi/4}, \tag{3.17d}$$

and hence, the noise spectra of the corresponding quadratures can be

evaluated as

$$V(\hat{Y}_{\varphi-\pi/4};\omega) = 1 - \frac{\tilde{C}_{11}(\omega) + \tilde{C}_{22}(\omega) + \tilde{C}_{21}(\omega) + \tilde{C}_{12}(\omega)}{2g^2(1 + I/\Delta)}, \tag{3.18a}$$

$$V(\hat{Y}_{\varphi+\pi/4};\omega) = 1 + \frac{\tilde{C}_{11}(\omega) + \tilde{C}_{22}(\omega) - \tilde{C}_{21}(\omega) - \tilde{C}_{12}(\omega)}{2g^2(1 - I/\Delta)}, \tag{3.18b}$$

$$V(\hat{X}_{\varphi-\pi/4};\omega) = 1 + \frac{\tilde{C}_{33}(\omega) + \tilde{C}_{44}(\omega) + \tilde{C}_{34}(\omega) + \tilde{C}_{43}(\omega)}{2g^2(1 + I/\Delta)}, \tag{3.18c}$$

$$V(\hat{X}_{\varphi+\pi/4};\omega) = 1 - \frac{\tilde{C}_{33}(\omega) + \tilde{C}_{44}(\omega) - \tilde{C}_{34}(\omega) - \tilde{C}_{43}(\omega)}{2g^2(1 - I/\Delta)}. \tag{3.18d}$$

In the next section we exploit these expressions to understand the entanglement properties of the system.

3.2 Squeezing/entanglement levels in the locking point

When there is no subharmonic injection, we know that there is (ideally) perfect entanglement between the signal and idler modes for $\sigma = 1$; as one moves above this threshold, the entanglement level is degraded more and more (although perfect amplitude correlations persist), and the signal and idler fields start oscillating at different frequencies. Our main intention with the injection is to lock the oscillation frequency of the signal and idler fields, what should contribute to make the observation and use of their entanglement simpler.

As we explained in section 1.2.4, a simple beam splitter transformation relates the entanglement between two modes, to the single-mode squeezing of two other modes. On the other hand, we saw in the previous section that the linearization technique naturally gives rise to a description of the quantum properties based on two modes with polarization $\boldsymbol{\varepsilon}_{\varphi\pm\pi/4}$. Moreover, the quadratures of these modes are easily proved to be proportional to weighted combinations of signal and idler quadratures,

$$x_{\varphi+\pi/4} = (x_{\mathrm{s}}^{\varphi+\pi/4} + x_{\mathrm{i}}^{-\varphi-\pi/4})/\sqrt{2}, \tag{3.19a}$$

$$y_{\varphi-\pi/4} = (x_{\mathrm{s}}^{\varphi+\pi/4} - x_{\mathrm{i}}^{-\varphi-\pi/4})/\sqrt{2}, \tag{3.19b}$$

$$y_{\varphi+\pi/4} = (y_{\mathrm{s}}^{\varphi+\pi/4} + y_{\mathrm{i}}^{-\varphi-\pi/4})/\sqrt{2}, \tag{3.19c}$$

$$-x_{\varphi-\pi/4} = (y_{\mathrm{s}}^{\varphi+\pi/4} - y_{\mathrm{i}}^{-\varphi-\pi/4})/\sqrt{2}, \tag{3.19d}$$

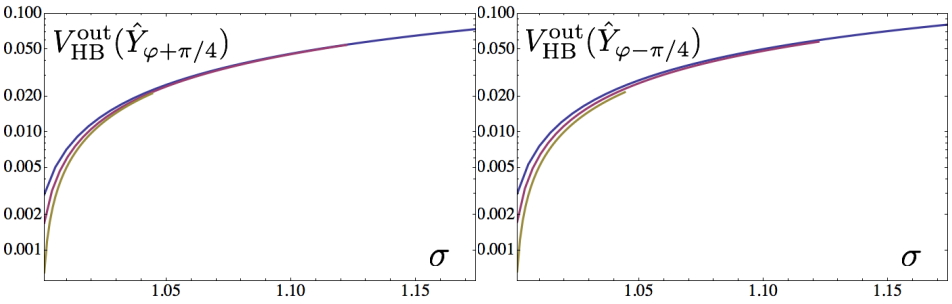

Fig. 3.1: Zero-frequency noise spectra of the $\hat{Y}$ quadrature of the $\varphi \pm \pi/4$ modes at the Hopf bifurcation. Three values of Δ have been chosen: 0.1 (blue), 0.07 (magenta) and 0.025 (yellow).

and hence, according to the criterion (1.20), the existence of squeezing in the quadratures of the $\varepsilon_{\varphi\pm\pi/4}$ modes indeed implies quantum correlations between the quadratures of the signal and idler modes, that is, entanglement. Therefore, in the following we study the squeezing levels that can be obtained in the $\varepsilon_{\varphi\pm\pi/4}$ modes at the Hopf bifurcation, which is the natural frequency-locking point of the system for small injections as explained in the previous section.

Particularizing expression (3.18) to the Hopf bifurcation where $I = (\sigma-1)/2$, and setting the noise frequency to zero, since it is easily proved that squeezing is larger for this choice, we get the following noise spectra

$$V_{\rm HB}(\hat{Y}_{\varphi\pm\pi/4}) = 1 - \frac{8(1+\sigma)[(3+\sigma)^2 + 2(\sigma\pm\Delta)^2 + 2(1\mp\tilde{\Delta})^2]}{[(3+\sigma)(1+3\sigma) + 4\Delta^2]^2}, \quad (3.20a)$$

$$V_{\rm HB}(\hat{X}_{\varphi\pm\pi/4}) = \frac{(3+\sigma)^2 + 4\Delta^2 \pm 4\Delta(\sigma-1)}{(\sigma-1\pm 2\Delta)^2}, \quad (3.20b)$$

where we remind that that the Hopf bifurcation exist only in the domain $1 < \sigma < 1+2\Delta$. In Figure 3.1, we show the zero-frequency noise spectrum of the $\hat{Y}_{\varphi\pm\pi/4}$ quadratures as a function of the pump injection σ for three different values of the detuning Δ. Note that large levels of squeezing are obtained at the Hopf bifurcation even when working up to 15% above threshold ($\sigma = 1.15$), proving that signal and idler have strong quantum correlations, even when the injection manages to lock their oscillation frequencies.

3.3 Quantum properties in a non-symmetric configuration.

In order to get analytical insight, up to now we have focused in the case in which signal and idler are detuned symmetrically with respect to the injected subharmonic frequency. In real experiments, such a symmetric configuration is in general not possible to achieve, since it requires unfeasible fine-tuning. Hence, in order for our locking method to be of use, it is important study whether our predictions persist when working out of such symmetric situation, what we do in this section.

The main difficulty when working out of the symmetric configuration is that we will not have analytic solution and stability analysis to rely on, and hence, we will need to resort to numerical tools to prove what we want. In particular, we will show that the Hopf instability is still present in the asymmetric case, as well as large levels of entanglement. However, since in this case we do not have analytical expressions to rely on, we will study the entanglement between signal and idler by computing their *logarithmic negativity*, which we introduce in appendix B.

Our starting point are again the normalized equations in which the pump has been adiabatically eliminated, which in the case of general signal and idler detuning take the form

$$\dot{\beta}_{\mathrm{s}} = \sqrt{\mathcal{I}} - (1 + \mathrm{i}\Delta_{\mathrm{s}})\,\beta_{\mathrm{s}} + \tilde{\beta}_{\mathrm{p}}\beta_{\mathrm{i}}^{+} + g\sqrt{\tilde{\beta}_{\mathrm{p}}}\eta(\tau), \tag{3.21a}$$

$$\dot{\beta}_{\mathrm{s}}^{+} = \sqrt{\mathcal{I}} - (1 - \mathrm{i}\Delta_{\mathrm{s}})\,\beta_{\mathrm{s}}^{+} + \tilde{\beta}_{\mathrm{p}}^{+}\beta_{\mathrm{i}} + g\sqrt{\tilde{\beta}_{\mathrm{p}}^{+}}\eta^{+}(\tau), \tag{3.21b}$$

$$\dot{\beta}_{\mathrm{i}} = \sqrt{\mathcal{I}} - (1 - \mathrm{i}\Delta_{\mathrm{i}})\,\beta_{\mathrm{i}} + \tilde{\beta}_{\mathrm{p}}\beta_{\mathrm{s}}^{+} + g\sqrt{\tilde{\beta}_{\mathrm{p}}}\eta^{*}(\tau), \tag{3.21c}$$

$$\dot{\beta}_{\mathrm{i}}^{+} = \sqrt{\mathcal{I}} - (1 + \mathrm{i}\Delta_{\mathrm{i}})\,\beta_{\mathrm{i}}^{+} + \tilde{\beta}_{\mathrm{p}}^{+}\beta_{\mathrm{s}} + g\sqrt{\tilde{\beta}_{\mathrm{p}}^{+}}[\eta^{+}(\tau)]^{*}, \tag{3.21d}$$

where we remind that

$$\tilde{\beta}_{\mathrm{p}} = \sigma - \beta_{\mathrm{s}}\beta_{\mathrm{i}}, \quad \tilde{\beta}_{\mathrm{p}}^{+} = \sigma - \beta_{\mathrm{s}}^{+}\beta_{\mathrm{i}}^{+}.$$

In order to study the quantum properties of the system, we apply again the linearization approach. The first step in the method consists in finding the classical configuration of the system, what we do numerically in this case. In particular, we first check that even in this asymmetric configuration, the classical version of this equations (found by setting the noises to zero and replacing the 'plus' stochastic amplitudes by the corresponding complex-conjugate ones) still possess a Hopf bifurcation above threshold ($\sigma > 1$). To this aim, at a given value of the pump parameter σ, we start from an

injection $\mathcal{I}$ large enough so that the system reaches a stationary solution $\bar{\beta}_{\mathrm{s,i}}$, and then decrease the injection gradually until the real part of one of the eigenvalues of the linear stability matrix gets as close to zero as we desire, checking that the imaginary part of the eigenvalue is non-zero. This proves that the Hopf instability is still present in this asymmetric case, and, moreover, we check that if we keep decreasing the injection, periodic orbits are found as the long-time term solution of the system. Hence, again we see that above threshold it is required a minimum value of the injection to lock the signal and idler frequencies.

Once we have identified the Hopf bifurcation, which again is the natural locking point of the type II OPO, we study its quantum properties by linearizing the Langevin equations (3.21). In particular, writing the stochastic amplitudes as

$$\beta_{\mathrm{s}} = \bar{\beta}_{\mathrm{s}} + b_{\mathrm{s}}, \tag{3.22a}$$
$$\beta_{\mathrm{s}}^{+} = \bar{\beta}_{\mathrm{s}}^{*} + b_{\mathrm{s}}^{+}, \tag{3.22b}$$
$$\beta_{\mathrm{i}} = \bar{\beta}_{\mathrm{i}} + b_{\mathrm{i}}, \tag{3.22c}$$
$$\beta_{\mathrm{i}}^{+} = \bar{\beta}_{\mathrm{i}}^{*} + b_{\mathrm{i}}^{+}, \tag{3.22d}$$

and keeping terms up to linear order in the quantum fluctuations and noises in Eq. (3.21), we obtain a linear system

$$\dot{\mathbf{b}} = \mathcal{L}\mathbf{b} + g\sqrt{|\bar{\beta}_{\mathrm{p}}|}\boldsymbol{\eta}(\tau), \tag{3.23}$$

with $\bar{\beta}_{\mathrm{p}} = \sigma - \bar{\beta}_{\mathrm{s}}\bar{\beta}_{\mathrm{i}}$ and

$$\mathbf{b} = \mathrm{col}(b_{\mathrm{s}}, b_{\mathrm{s}}^{+}, b_{\mathrm{i}}, b_{\mathrm{i}}^{+}), \tag{3.24a}$$
$$\boldsymbol{\eta}(\tau) = \mathrm{col}[e^{\mathrm{i}\varphi_{\mathrm{p}}}\eta(\tau), e^{-\mathrm{i}\varphi_{\mathrm{p}}}\eta^{+}(\tau), e^{\mathrm{i}\varphi_{\mathrm{p}}}\eta^{*}(\tau), e^{-\mathrm{i}\varphi_{\mathrm{p}}}\eta^{+*}(\tau)], \tag{3.24b}$$

where $\varphi_{\mathrm{p}} = \arg\{\bar{\beta}_{\mathrm{p}}\}$. This linear problem can be solved exactly in the same way as we did in the case of equation 3.5, that is, by finding the biorthonormal eigensystem of $\mathcal{L}$

$$\mathcal{L}\mathbf{v}_j = \lambda_j\mathbf{v}_j, \qquad \mathcal{L}^{\dagger}\mathbf{u}_j = \lambda_j^{*}\mathbf{u}_j, \qquad \mathbf{u}_j^{\dagger}\mathbf{v}_l = N_j\delta_{jl}, \tag{3.25}$$

and defining the projections $c_j(\tau) = \mathbf{u}_j^{\dagger}\mathbf{b}(\tau)$, which will obey decoupled first-order linear differential equations, so that it is straightforward to compute their spectral correlation matrix

$$\tilde{C}_{jl}(\omega) = \int_{-\infty}^{+\infty} d\tau' e^{-\mathrm{i}\omega\tau} \lim_{\tau\to\infty}\langle c_j(\tau)c_l(\tau+\tau')\rangle = \frac{g^2|\bar{\beta}_{\mathrm{p}}|\mathbf{u}_j^{\dagger}S\mathbf{u}_l^{*}}{(\lambda_j+\mathrm{i}\omega)(\lambda_l-\mathrm{i}\omega)}, \tag{3.26}$$

where S is the correlation matrix of the noises, whose elements are defined by the relation $\langle \eta_m(\tau)\eta_n(\tau')\rangle = S_{mn}\delta(\tau-\tau')$, so that

$$S = \begin{pmatrix} 0 & 0 & e^{2i\varphi_p} & 0 \\ 0 & 0 & 0 & e^{-2i\varphi_p} \\ e^{2i\varphi_p} & 0 & 0 & 0 \\ 0 & e^{-2i\varphi_p} & 0 & 0 \end{pmatrix}. \tag{3.27}$$

Hence, we see that the way of solving the problem is formally equivalent to what we did in the previous case, except for now the classical stationary solution $\bar{\beta}_{s,i}$ is only known numerically, and hence, so does the linear stability matrix $\mathcal{L}$ and its eigensystem.

On the other hand, we can characterize the state of the system by the covariance matrix, which was introduced for a single mode in Eq. (1.28). However, the type II OPO we are studying is described by two modes with orthogonal polarization, the signal and idler modes in particular, what means that we need to extend the definition of the covariance matrix to two modes [29, 30, 49]. Let us collect the quadratures of signal and idler in a vector $\hat{\mathbf{R}} = (\hat{X}_s, \hat{Y}_s, \hat{X}_i, \hat{Y}_i)$, and similarly for the corresponding normalized stochastic versions of the quadratures, $\mathbf{r} = (x_s, y_s, x_i, y_i)$. In this polarization basis, the two-mode spectral covariance basis of the light coming out of the resonator is defined by

$$V_{si}(\Omega) = \mathbb{1} + 2\gamma_s \int_{-\infty}^{+\infty} dt' \lim_{t\to\infty} M(t,t')e^{-i\Omega t'}. \tag{3.28}$$

where the elements of the normally-ordered two-time correlation matrix M are given by $M_{jl} = \langle :\{\delta\hat{R}_j(t), \delta\hat{R}_l(t'-t)\}:\rangle/2$. At the end of this section we explain how this two-mode covariance matrix allows for a characterization of the entanglement between the signal and idler modes. But before that, let's see how we can compute it from the solution that we found for the linearized problem, in particular from the spectral correlation matrix $\tilde{C}(\omega)$ of the projections.

First, note that in terms of averages of the normalized stochastic quadratures we are working with and the normalized noise frequency $\omega = \Omega/\gamma_s$, the previous expression can be rewritten as

$$V_{si}(\omega) = \mathbb{1} + \frac{2}{g^2}\tilde{M}(\omega), \tag{3.29}$$

where the elements of the normalized, normally-order spectral correlation

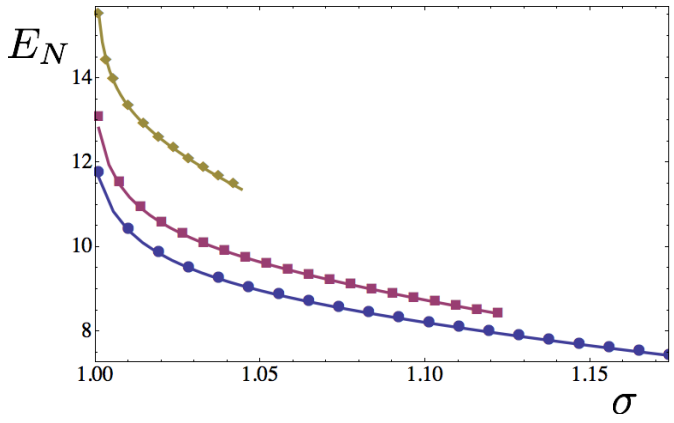

Fig. 3.2: Logarithmic negativity (E_N) as a function of the pump parameter σ at the Hopf bifurcation, which corresponds to the minimum value of the injection for which the oscillation frequencies of signal and idler get locked. The solid curves correspond to the analytical solution that we found for the symmetric case within the linearized theory, while the markers are found numerically for the asymmetric case as explained in the text. Three values of Δ have been chosen: 0.1 (blue), 0.07 (magenta) and 0.025 (yellow).

matrix $\tilde{M}$ are given by

$$\tilde{M}_{jl}(\omega) = \frac{1}{2}\int_{-\infty}^{+\infty} d\tau' e^{-\mathrm{i}\omega\tau'} \lim_{\tau\to\infty} \langle\{\delta r_j(\tau), \delta r_l(\tau'-\tau)\}\rangle. \tag{3.30}$$

Then, note that the relation between the quadrature fluctuations $\delta\mathbf{r}$ and the quantum fluctuations $\mathbf{b}$ can be written in matrix form as $\delta\mathbf{r} = \mathcal{R}\mathbf{b}$ with

$$\mathcal{R} = \begin{pmatrix} 1 & 1 & 0 & 0 \\ -i & i & 0 & 0 \\ 0 & 0 & 1 & 1 \\ 0 & 0 & -i & i \end{pmatrix}, \tag{3.31}$$

while defining the vector of projections $\mathbf{c} = \mathrm{col}(c_1, c_2, c_3, c_4)$ and the matrix of left-eigenvectors $\mathcal{U} = \mathrm{col}(\mathbf{u}_1^\dagger, \mathbf{u}_2^\dagger, \mathbf{u}_3^\dagger, \mathbf{u}_4^\dagger)$, we can write $\mathbf{b} = \mathcal{U}^{-1}\mathbf{c}$. Hence, we see that we can write the quadrature-vector in terms of the projection-vector as $\delta\mathbf{r} = \mathcal{R}\mathcal{U}^{-1}\mathbf{c}$, from which we get the normally-ordered spectral correlation matrix

$$\tilde{M}(\omega) = \frac{1}{2}\mathcal{R}\mathcal{U}^{-1}[\tilde{C}(\omega) + \tilde{C}^T(\omega)]\mathcal{U}^{-1T}\mathcal{R}^T. \tag{3.32}$$

Let us remark that this expression can be efficiently evaluated numerically once we have identified the classical stationary solution at the Hopf bifurcation, $\bar{\beta}_{\mathrm{s,i}}$, from which we derive the linear stability matrix $\mathcal{L}$, its eigensystem, and from it $\mathcal{U}^{-1}$ as well as the spectral correlation matrix $\tilde{C}(\omega)$. In the following we take $\omega = 0$ as this was the value of the noise frequency that lead to the largest levels of entanglement in the symmetric case.

Having the covariance matrix, we are now ready to analyze the entanglement between the signal and idler modes. In order to be numerically efficient, in this section we choose to quantify the entanglement between these two modes via the logarithmic negativity, which can be easily computed from the two-mode spectral covariance matrix [29, 30, 49], as we explain in Appendix B. In order to compare with the symmetric case, we proceed as follows. For every value of the pump parameter σ, we choose some distance between the signal and idler resonances, say $2\Delta > 0$. In the symmetric case, this means that we choose $\Delta_{\mathrm{s}} = -\Delta_{\mathrm{s}} = \Delta$. On the other hand, as a highly asymmetric case we choose $\Delta_s = \Delta + \Delta/2$ and $\Delta_i = \Delta - \Delta/2$. In Fig. 3.2 we compare the logarithmic negativity obtained in the symmetric (solid line) and asymmetric (markers) cases for the three values of Δ that we also chose in figure 3.1: 0.1 (blue), 0.07 (magenta) and 0.025 (yellow). Remarkably, we can see that, not only the entanglement levels are also high in the asymmetric case, but they coincide almost exactly with the ones of the symmetric case. This proves that entanglement properties of the system depend only on the distance between the signal and idler resonances, and not on how they are disposed with respect to the frequency of the subharmonic injection.

III

SPONTANEOUS, COLLECTIVE COHERENCE IN DRIVEN, DISSIPATIVE CAVITY ARRAYS

4. INTRODUCTION

4.1 Light-matter interaction. The one emitter laser

Quantum electrodynamics is the relativistic quantum field-theory that describes the interaction of light with matter. We will discuss a fully quantum theory of the atom-field interactions. For our proposes it is convenient to consider the atom as a two level system, where the electrons can populate two energy states, an excited state and the ground state. Our goal in this section is to explain how light interacts with an atom if isolated in a cavity with highly reflecting walls separating it efficiently from the external world.

In 1917, by studying the equilibrium properties of a gas of photons in a cavity, Albert Einstein postulated that there are three different ways that light can interact with matter (Fig. 4.1). The first process, stimulated absorption, begins with an incoming photon and an atom in the ground (lowest-energy) state, resulting in no outgoing photon and the atom in an excited (higher-energy) state. The second, spontaneous emission, is the reverse of this process; it begins with no incoming photon and the atom in an excited state and results in an outgoing photon and the atom in the ground state. This decay of the excited state is spontaneous: it occurs randomly. Stimulated emission seems more mysterious at first, as it describes emission in presence of another photon: if an excited atom as above is in presence of a photon with the frequency close to that of the atomic transition, then the atom decays towards its ground state emitting a clone photon of the original one, leaving two identical copies in the final state. The later is the main process behind the functioning of the laser.

Cavity quantum electrodynamics (cQED) was born from the idea that these radiative properties are not a property of the atom itself but of the coupled atom-radiation field system. Introducing the atom inside a cavity, the "modified" vacuum because the presence of mirrors would alter its radiative properties. That was the case, when Edward Mills Purcell discovered, in 1946, a spontaneous emission rate enhancement (Purcell effect).

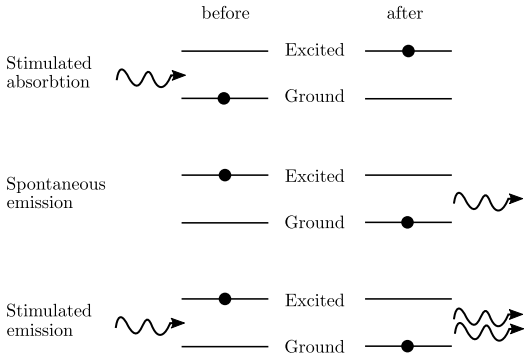

Fig. 4.1: Processes of the interaction between light and a two level atom.

Several years later, the first experimental work on inhibited spontaneous emission was done by Drexhage, Kuhn and Shafer (reviewed in [50]). But at that moment, the quality factors (Q [1]) of the cavities where not enough to alter the dynamical properties of the atom-field system (*weak-coupling*). With the better resonators which were subsequently developed, the coupling of the atom to one mode of the field has become a dominant effect in the system's evolution. The radiative properties in this *strong-coupling* regime radically differ from what is observed on an atom in free space. In this case, emitted photons could stay on the cavity until they are reabsorbed by its own emitter. Being this process dominant over the leakage of the photons out of the cavity, the photons enter in a whole sequence of absorptions and emissions known as *Rabi oscillations*, until their ultimate decay out of the cavity.

On the experimental side, the strong-coupling regime is now firmly established at the single and few photon level not only with atoms [51] but as well with *artificial atoms*, which are systems that behave by all means as an atom, e.g., superconducting qubits [52, 53], or semiconductor quantum dots [54–56]. We will join all these concepts under the name *emitter* or *two level system* (2LS).

On the theoretical side, the Jaynes-Cummings (JC) Hamiltonian, dis-

[1] The quality factor of a cavity is defined by

$$Q = \omega_a \tau$$

where ω_a is the cavity frequency and $\tau = 1/\Delta\omega$ is the photon lifetime, where $\Delta\omega$ is the cavity linewidth.

cussed in Appendix C, is now the most famous and simple example of quantum optics and cQED. It provides the fundamental picture of light-matter interactions at the ultimate quantum level[2]: when only one mode of light a (an harmonic oscillator, HO) is interacting with only one mode of matter σ (a 2LS). The JC Hamiltonian is (from now on we will take $\hbar = 1$),

$$H^{JC} = \omega_a a^\dagger a + \omega_\sigma \sigma^\dagger \sigma + g\left(a^\dagger \sigma + a\sigma^\dagger\right) \tag{4.1}$$

where $\omega_{a,\sigma}$ are the free energies for the modes and g is their coupling strength. In order to reach this Hamiltonian, two important approximations have been done: the dipole approximation, where one considers that the size of the atom (few Angstroms) is much smaller than the typical wavelength of the field (a few hundreds of nanometers), and the so called, rotating wave approximation, where the rapidly oscillating terms of the Hamiltonian are neglected (see Appendix C).

The model that we propose in this part of the thesis is conformed by several coupled identical systems widely known in the literature as the one emitter laser (OEL), which in the simplest description consist in a two level emitter inside an optical cavity. The OEL was firstly proposed and theoretically studied by Mu and Savage [57][3], with the aim of achieving lower thresholds for lasing. They encouraged experimentalist to bring the number of emitters in a conventional laser to unity. In a very high quality factor (Q), the emitter reaches the strong-coupling regime at the single excitation level. They showed that, in this regime, a single incoherently excited emitter (described below) can constitute the whole gain medium and populate singlehandedly the cavity with a very large number of photons. In order to describe it, we will use the Jaynes-Cummings Hamiltonian, but as we know, in all physical processes there is an associated loss mechanism, photons are dissipated due to the imperfect confinement of the light, and emitter excitations have finite lifetimes. We are going to explore the driven-dissipative regime of this structures, where photon losses are continuously compensated by pumping new photons into the cavity.

There are several ways in which a quantum theory of damping may be developed. We are going to use the so-called master equation, which is the equation of motion for the reduced density operator for a small system

[2] In this part of the thesis, as we will always work with operators, we will assume the notation $a \equiv \hat{a}$.

[3] widely studied in [58–62]

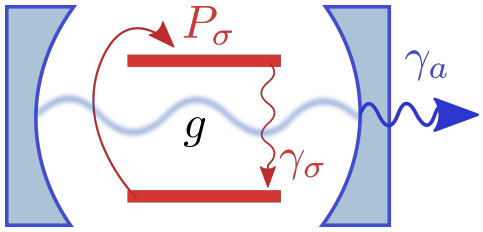

Fig. 4.2: Scheme of the one emitter laser explained in the text.

interacting with a large system, or a reservoir, having infinitely many densely spaced energy levels, which will represent the outside-of-the-cavity world.

As we can see in Fig 4.2, we will have three incoherent process; the cavity photons leaking at a rate γ_a, the spontaneous decay of the emitter at a rate γ_σ, and the incoherent excitation of the emitter at a rate P_σ [4]. We will neglect pure dephasing, due to the coupling of the 2LS with the thermally fluctuating environment, since it does not modify the results apart from increasing the decoherence that P_σ already induces. Finally the master equation reads

$$\partial_t \rho = -i\left[H^{JC}, \rho\right] + \gamma_a \mathcal{L}_a(\rho) + \gamma_\sigma \mathcal{L}_\sigma(\rho) + P_\sigma \mathcal{L}_{\sigma^\dagger}(\rho) \tag{4.2}$$

where the Liuvillian $\mathcal{L}_c(\rho)$ in the Lindblad form is

$$\mathcal{L}_c(\rho) = \frac{1}{2}(2c\rho c^\dagger - c^\dagger c\rho - \rho c^\dagger c) \tag{4.3}$$

with $c = \{a, \sigma, \sigma^\dagger\}$. In order to reach this equation there are some assumptions that have been done: The 2LS and the cavity weakly interact with the environment, a large bath that follows bosonic statistics in thermal equilibrium[5]. The later has a fast dynamics, i.e., every interaction process occurs so fast that doesn't leave any track on the bath and it is quickly forgotten. And finally, the system is assumed to be separable at the beginning (t=0).

With the master equation one can solve exactly the evolution of any expectation value of system operators ($O \equiv a^{\dagger n} a^m \sigma^{+\nu} \sigma^\mu$), but in practice, the complexity of this problem scales quickly with the number of photons

[4] This one differs from usual laser pumping in that the transition of the 2LS is not directly driven. It can be done in several ways, e.g., pumping to an upper level that naturally decays to the excited level of the 2LS.

[5] Actually, in the model we present here, we assume that the bath is at $T = 0^o K$

and it is a challenge for any computer. The calculations are done by allowing a maximum number of photons (a maximum number of states). But for a reasonable number of photons, still takes a lot of CPU time in computer grids, even more for a cavity array, which is the goal of this part of the thesis. In [63], they show that the cluster expansion method [64], which consist in breaking the correlators $\langle O \rangle$ to the smallest not-zero order, is a very good approximation in the lasing regime, even for several emitters inside a cavity. We will study the system in the stationary states, where photon pumping and losses balance each other in a *dynamical equilibrium*.

In order to understand some features of the cavity array model, we show in the next subsection the solutions of the one-emitter laser (Eq. 4.2) in the steady state under the cluster expansion approximation, as well as the main observables to detect if the OEL is in the lasing regime.

The one emitter laser

From the master equation of the one-emitter laser, Eq. 4.2, we can compute the equations for the dynamics of any correlator $\langle O \rangle \equiv \left\langle a^{\dagger n} a^m \sigma^{\dagger \nu} \sigma^{\mu} \right\rangle$. From $\langle O \rangle = \mathrm{Tr}(\rho O)$ we have

$$\begin{aligned} \partial_t \langle O \rangle =& \mathrm{Tr}(\partial_t \rho O) = \frac{1}{i\hbar} \left\langle \left[O, H^{JC} \right] \right\rangle \\ &+ \gamma_a \mathrm{Tr}\left(\rho \mathcal{L}_a(O)\right) + \gamma_\sigma \mathrm{Tr}\left(\rho \mathcal{L}_\sigma(O)\right) + P_\sigma \mathrm{Tr}\left(\rho \mathcal{L}_{\sigma^\dagger}(O)\right) \end{aligned} \tag{4.4}$$

where $\mathcal{L}_c(O)$ follows 4.3. Our purpose is to calculate the solution in the steady state ($\partial_t \langle O \rangle = 0$). We have three different types of non-zero correlators in the steady state:

$$\left\langle a^{\dagger n} a^n \right\rangle, \quad \left\langle a^{\dagger n-1} a^{n-1} \sigma^+ \sigma \right\rangle, \quad \text{and} \quad \left\langle a^{\dagger n} a^{n-1} \sigma \right\rangle, \tag{4.5}$$

We do not have any single operator correlators because the stochastic nature of pump makes $\langle a \rangle = 0$ (they are averaged over all phases). The equations for $n = 1$ provide the evolution of the number of cavity photons $n_a = \langle a^\dagger a \rangle$, the number of excitations $n_\sigma = \langle \sigma^\dagger \sigma \rangle$ and the photon assisted polarization $\left\langle \sigma a^\dagger \right\rangle$. The equations for the populations are

$$\frac{\partial n_a}{\partial t} = 2g \mathrm{Im}\left[\left\langle \sigma a^\dagger \right\rangle \right] - \gamma_a n_a \tag{4.6a}$$

$$\frac{\partial n_\sigma}{\partial t} = -2g \mathrm{Im}\left[\left\langle \sigma a^\dagger \right\rangle \right] - (\gamma_\sigma + 1) n_\sigma + P_\sigma, \tag{4.6b}$$

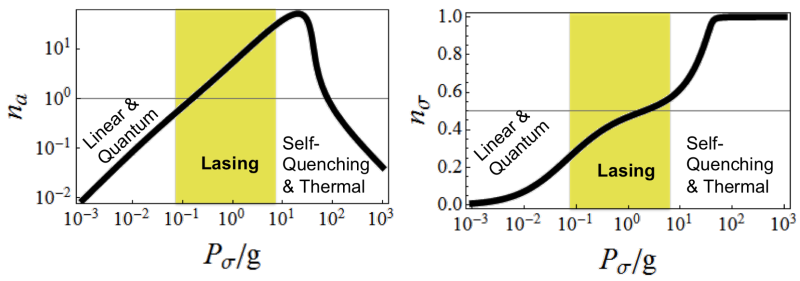

Fig. 4.3: For the parameters: $\gamma_a = 0.1$, $\gamma_\sigma = 0.01$, $\Delta = 0$, the populations n_a and n_σ versus the normalized incoherent pumping P_σ/g with the different regimes that the OEL can operate.

which only depend on $n = 1$ correlators. However, the photon assisted polarization depends on higher order correlators

$$\left(\frac{\partial}{\partial t} + \frac{\Gamma}{2} + i\Delta\right)\langle \sigma a^\dagger \rangle = ig\left(\left\langle \sigma^\dagger \sigma a a^\dagger \right\rangle - \left\langle \sigma \sigma^\dagger a^\dagger a \right\rangle\right) \tag{4.7}$$

where $\Delta = \omega_\sigma - \omega_a$ is the detuning and $\Gamma = P_\sigma + \gamma_\sigma + \gamma_a$.

We now apply cluster correlator expansion, which is proved to be accurate for $N > 1$ emitters in a single cavity [63]. This expansion consist in

$$\left\langle \sigma^\dagger \sigma a a^\dagger \right\rangle \approx \left\langle \sigma^\dagger \sigma \right\rangle \left\langle a a^\dagger \right\rangle \tag{4.8}$$

$$\left\langle \sigma \sigma^\dagger a^\dagger a \right\rangle \approx \left\langle \sigma \sigma^\dagger \right\rangle \left\langle a^\dagger a \right\rangle . \tag{4.9}$$

and going back to 4.7 we get for the populations 4.6

$$\frac{\partial n_a}{\partial t} = F\left(n_a(2n_\sigma - 1) + n_\sigma\right) - \gamma_a n_a, \tag{4.10a}$$

$$\frac{\partial n_\sigma}{\partial t} = -F\left(n_a(2n_\sigma - 1) + n_\sigma\right) - (\gamma_\sigma + P_\sigma)n_\sigma + P_\sigma, \tag{4.10b}$$

where

$$F = \frac{4g^2\Gamma}{\Gamma^2 + 4\Delta^2}, \tag{4.11}$$

In Fig 4.3 there is an example of the solutions for the populations, n_a and n_σ, versus the pump, P_σ, as predicted by Eqs. 4.10. In [61] there is a full description of the regimes at which the OEL operates, but for our proposes it will be enough to describe them briefly. *Linear* and *quantum regimes* [65–67], where the emitter is mainly in the ground state and the few

photon effects are dominant, *the lasing regime*, where the emitter population is around 0.5, the cavity can accumulate a great number of photons and the field becomes poissonian, and finally, the *self-quenching* and *thermal regimes* where the pumping drives the emitter to saturation reducing the number of photons until $n_\sigma \to 1$, where the field becomes thermal. In order to illustrate the behaviour of the OEL, although it cannot be calculated within our approximation, a good measurable quantity to differentiate this regimes is the second order correlation function, defined by

$$g^{(2)} = \left\langle a^{\dagger 2} a^2 \right\rangle / n_a^2 \tag{4.12}$$

that can be understood as the probability of detecting two photons with zero delay. Its value will be: $g^{(2)} < 1$ for quantum (few photon) regime, $g^{(2)} = 1$ in the lasing regime and $1 < g^{(2)} \leq 2$ for self-quenching and thermal statistics. In Fig. 4.4, computed with a quantum-jump Montecarlo [68] (taken from [69]), we can see the exact solution for $g^{(2)}$ and its dependence with the parameter Δ and the cavity leakage (γ_a) versus the incoherent pump (P_σ). As we can see, increasing γ_a decreases the size of lasing regime (white zone). On the other hand, for larger detunings we will create a larger "threshold" until we completely eliminate the lasing region. However to be completely sure that we are in lasing regime one should check that every higher order correlator functions, $g^{(n)}$[6], are equal to unity. In the following we present a more conclusive way to assure this fact. There is a feature that only happens when a 2LS is driven by a laser close to resonance (even if the laser is created by itself). It was first proposed by Mollow [70] that, at resonance, the emission spectra has a certain structure. This structure was later known as the *Mollow triplet* because of its three peaks. The physical origin of these peaks is the transitions between the dressed states of the Jaynes-Cumings Hamiltonian at high number of excitations (see Appendix C). As shown in Fig. 4.5, the two transitions between different types of dressed states become degenerate for the central peak (0), while transitions between the same type of dressed states give rise to the sidebands. The full expression of the resonant spectrum is given in [71].

Generalizations of the OEL model have been studied for two [72] and multiple emitters [66, 67, 73] or emitters supporting multi-exciton states [74].

[6] Defined by

$$g^{(n)} = \left\langle a^{\dagger n} a^n \right\rangle / n_a^n$$

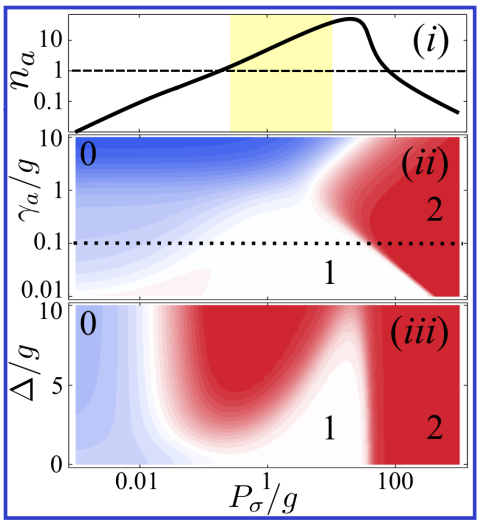

Fig. 4.4: (i) Cavity population n_a as a function of P_σ for $\gamma_a = 0.1$, $\gamma_\sigma = 0.01$ and $\Delta = 0$, with the lasing region highlighted in yellow. Below, contour plots of $g^{(2)}$ as a function of P_σ and (*ii*) γ_a at $\Delta = 0$, or (*iii*) Δ at $\gamma_a = 0.1g$, with $g^{(2)} > 1$ in red, $g^{(2)} = 1$ in white and $g^{(2)} < 1$ in blue.

4.2 Cavity-QED arrays in many body physics

One of the main results of this part of the thesis is that in arrays of OELs coupled via the exchange of photons show the main features of its constituents, i.e., lasing and its typical photoluminescence lineshape (PL), the Mollow triplet [61, 75], can be observed even when we are far out of resonance between emitter and cavity as a result of the emergence of collective photonic modes. On the other side, it is well known that several subsystems strongly interacting with each other will give rise to collective physics not present if you threat them separately. That is the field of study of *many body physics*.

We have already described a system in which one atom interacts with one mode of light. At most, Quantum Optics is concerned with the interaction of a few atoms and light quanta. The physics of such systems can usually be very well understood by ignoring collective effects and treating the interactions perturbatively. This is a much simpler and cleaner situation than the one encountered in the condensed matter context. There, strong interactions among the basic constituents, such as nuclei and electrons, lead to the emergence of completely new physics when one considers a

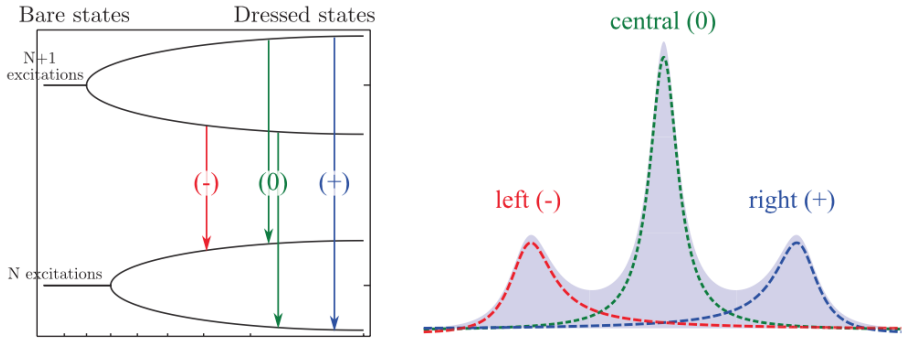

Fig. 4.5: (Taken from [71]) Origin of the peaks in the Mollow triplet: The three different freqencies are found in the four possible transitions between two Jaynes-Cummings rungs at high intensities.

mesoscopic or macroscopic number of interacting particles. Thus, even though the fundamental interactions between the constituent particles are usually known, it is challenging to fully describe the properties of such systems. The seemingly simplified models used to describe these correlations, e.g the Hubbard model, are extremely difficult to solve, and over the years some analytical and numerical methods have been developed. Together with these more "traditional" methods, in the recent years it was proposed that strongly correlated systems could be studied by means of quantum simulators [76], i.e., fabricated systems that can experimentally simulate the model Hamiltonian underlying the non-trivial properties of the physical systems under consideration. The advantages of this approach is twofold. First of all, it is possible to explore the properties of strongly correlated model Hamiltonians also in those regions of the phase diagram that are elusive to numerical an analytical investigations. Second, it allows testing the extent to which the model Hamiltonians under consideration are appropriate for treating the physical systems that they are supposed to describe or determining whether additional ingredients are necessary.

Quantum simulators have a relatively long and successful history. Probably the first fabricated systems to have these characteristics were Josephson junction arrays [77]. Also, cold atoms in optical lattices [3], proved to be excellent simulators for a large variety of strongly interacting Fermi and Bose systems. The topic of the present part of the thesis are the quantum simulators based on arrays of QED-cavities [78–80].

Cavity-QED arrays bring the possibility to realize strongly correlated

states of light and offer an implementation of a quantum simulator for lattice models. The first requirement for a quantum simulator is to act as a calculator specifically tailored to the solution of the model that it implements. The knowledge on the model gained with the quantum simulator can then be applied to all the other physical systems described by the same model. With respect to the implementation of a quantum simulator in an optical lattice the cavity array may offer the advantage that each site of the array can be addressed independently. The expectation values of the observables could then be measured directly from the light emitted by one cavity. More over, the cavity arrays can be implemented with several different experimental systems, and this may offer some advantages. They can operate at high temperatures (as compared to Josephson arrays and optical lattices) and they might allow exploration of a number of new equilibrium and nonequilibrium quantum phase transitions. On the other side, optical lattices seem unbeatable in terms of scalability and absence of imperfections.

Even though ground or thermal equilibrium states of the corresponding quantum many-body systems are challenging to generate in experiments, much of the initial attention has focussed on this regime [81–84]. The stationary states of coupled cavity arrays have received considerable attention in recent years, where coherent and strongly correlated phases have been discovered [85–87], but also analogies to quantum Hall physics [88] and topologically protected quantum states [89] have been discussed. In previous investigations in driven-dissipative regimes, the pump mechanism that injects photons into the array has been assumed to be a coherent drive at each cavity [85–89]. Therefore any phase-coherence between light fields in distant cavities that was seen in these studies can, at least in part, be attributed to the fixed phase relation between their coherent input drives. Here, in contrast, we show that such a coherence between distant cavities can build up spontaneously, triggered only by physical processes within the array. In this way, we address the question of whether a non-equilibrium superfluid or Bose Einstein condensate can develop in these structures. To this end, we consider a cavity array that is only driven by an incoherent pump which explicitly avoids any external source for any preferred phase relation between photons in different cavities.

We focus our analysis on the build-up of first-order coherence between the fields in distant cavities as this quantity is typically considered for investigating long range order and the emergence of superfluidity, e.g. in optical lattices [90]. As is it shown below, we find that collective correlations

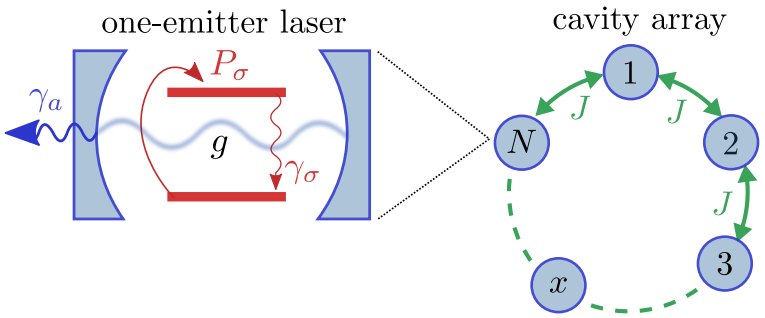

Fig. 4.6: The building block of the array, the one-emitter laser and the scheme of the total system in one dimension: a circular array of N coupled cavities containing single emitters.

indeed build up in our set-up when the cavities are in the lasing regime. These correlations decay faster than any power of the distance as the distance between the considered cavities tends to infinity for any dimension of the array. As intuitively expected, the associated correlation length increases with increasing photon tunneling between the cavities. For the interaction-dominated regime this increase is logarithmic, whereas it is a power law in the tunneling-dominated regime. Nonetheless, for any non-vanishing cavity decay rate, the correlation length always remains finite.

Related questions are of high relevance for ultra-cold atoms [91], ions [92], superconducting circuits [93] or exciton-polariton condensates [84]. For the latter, functional renormalization group approaches showed that, correlations at least decay exponentially in isotropic two-dimensional [94] but can be long range in three-dimensional systems [95].

Suitable experimental platforms for exploring our findings are superconducting circuit [83, 96], photonic crystal [97, 98], micro-pillar [99], or waveguide coupled cavities [100], where strong coupling regimes and coherent photon transfer between cavities have been demonstrated. See also the reviews [81, 83, 101].

4.3 Model

We consider an array of cavities, each of which interacts with a two level emitter, and is connected to adjacent cavities via photon tunneling. Our system, c.f. Fig. 4.6, is thus described by a Jaynes-Cummings-Hubbard Hamiltonian ($\hbar = 1$),

$$H = \sum_j H_j^{JC} + \sum_{<j,l>} J[a_j^\dagger a_l + a_l^\dagger a_j] \tag{4.13}$$

with $H_j^{JC} = \omega_a a_j^\dagger a_j + \omega_\sigma \sigma_j^\dagger \sigma_j + g(a_j^\dagger \sigma_j + a_j \sigma_j^\dagger)$, for each cavity j. We assume periodic boundary conditions and a homogeneous array with photon tunneling rate J so that all H_j^{JC} share the same photon frequency ω_a, emitter transition frequency ω_σ, and light-matter coupling g.

As for the OEL (subsection 4.1), the parameters of the system are: the emitter is excited with incoherent pump at a rate P_σ [102], the emitter spontaneously decay at a rate γ_σ, and the cavity photons in turn are lost at a rate γ_a from each cavity.

Similarly to Eq.4.2, the dynamics of our system, including these incoherent processes, follows the master equation,

$$\partial_t \rho = -i[H, \rho] + \sum_j [\gamma_a \mathcal{L}_{a_j} + \gamma_\sigma \mathcal{L}_{\sigma_j} + P_\sigma \mathcal{L}_{\sigma_j^\dagger}](\rho), \tag{4.14}$$

It is useful to introduce Bloch modes for the photons [103] to diagonalize the cavity part of Hamiltonian (Eq. 4.13). For a rectangular lattice of cavities of dimension m and edge length N, these modes read $p_{\vec{k}} = N^{-m/2} \sum_{\vec{r}} e^{i\vec{k}\cdot\vec{r}} a_{\vec{r}}$, where $\vec{r}$ is an m-dimensional lattice site index and written in terms of these Bloch modes, the Hamiltonian (Eq. 4.13) takes the form

$$H = \sum_{\vec{k}} \omega_{\vec{k}} p_{\vec{k}}^\dagger p_{\vec{k}} + \sum_{\vec{r}} \omega_\sigma \sigma_{\vec{r}}^\dagger \sigma_{\vec{r}} + \sum_{\vec{k},\vec{r}} (G_{\vec{k}\vec{r}} p_{\vec{k}} \sigma_{\vec{r}}^\dagger + \text{h.c.}), \tag{4.15}$$

with $\omega_{\vec{k}} = \omega_a + 2J \sum_{\alpha=1}^m \cos k_\alpha$, $G_{\vec{k}\vec{r}} = gN^{-m/2} e^{-i\vec{k}\cdot\vec{r}}$, and $k_\alpha = \frac{2\pi}{N}[-N/2 + l_\alpha]$ for N even or $k_\alpha = \frac{2\pi}{N}[-(N+1)/2 + l_\alpha]$ for N odd ($l_\alpha = 1, \ldots, N$). The Bloch modes form a band with their frequencies $\omega_{\vec{k}}$ distributed across the interval $[\omega_a - 2mJ, \omega_a + 2mJ]$. As easily seen, all modes $p_{\vec{k}}$ decay at the same rate γ_a. Hence, we have mapped our model to a set of independent harmonic modes that all couple to the same set of emitters with complex coupling constants $G_{\vec{k}\vec{r}}$. It is useful to define for each mode, the detuning $\Delta_{\vec{k}} = \omega_\sigma - \omega_{\vec{k}}$, the total decoherence rate $\Gamma = \gamma_a + P_\sigma + \gamma_\sigma$, the effective coupling $g_{\vec{k}}^{\text{eff}} = g/\sqrt{1 + (2\Delta_{\vec{k}}/\Gamma)^2}$, and the population transfer from the emitters to the mode (*Purcell rate*) $F_{\vec{k}} = 4(g_{\vec{k}}^{\text{eff}})^2/\Gamma$. Each Bloch mode can thus be driven by coherent excitation exchange with the N emitters.

In the lower pumping regimes, correlations can be expected to be shorter ranged. Let me explain in detail. Our approach is expected to yield accurate

results in the lasing and thermal regimes, where $P_\sigma > \gamma_\sigma, \gamma_a$ and the emitters are population inverted, $n_\sigma > 1/2$. As it shows the largest correlation length, we focus on the lasing regime in the main text. Yet in the low pumping regimes, complementary to the regimes where our considerations apply, one expects correlations to decay faster than in the lasing regime.

In the limit of vanishing pumping, where the emitter occupancies are very low, $n_\sigma \ll 1$, one can approximate the emitters by harmonic oscillators and our model maps to a set of coupled harmonic oscillators. In this exactly solvable, linear regime, the width of the Lorentzian distribution in Eq. (4.19) is larger than in the lasing regime and therefore correlations $\mathcal{C}(\vec{r})$ decay faster.

Moreover, increasing the pumping to transfer some non-negligible population to the cavities, $n_a \sim 1$, the array enters the quantum regime. The nonlinearity of the emitters acts as a repulsive on-site interaction between excitations in the cavity array. Similar to the equilibrium situation, this interaction will keep excitations from delocalizing across the array and correlations will remain short ranged [104]. It is important to note here, that the nonlinearity of a Jaynes-Cummings system scales as the square root of the photon number in the cavity, $\sqrt{n_a}$. The coupling between cavities, in turn, is quadratic in the photon operators $(Ja_j a_{j+1}^\dagger + \text{H.c.})$ so that its strength scales linearly with n_a. Hence for higher input powers and thus higher photon numbers n_a, the influence of the nonlinearity is weakened. As one enters the lasing regime, where our approach applies, one thus finds longer range correlations.

4.4 Rate Equations

Similarly for the one emitter case (subsection 4.1), from the above master equation, we derive a hierarchy of coupled equations of motion for correlators (see the Appendix D for details) starting with $n_\sigma = \left\langle \sigma_{\vec{r}}^\dagger \sigma_{\vec{r}} \right\rangle$ and $n_{\vec{k}} = \left\langle p_{\vec{k}}^\dagger p_{\vec{k}} \right\rangle$. We also apply the cluster-expansion method up to order two [64] to truncate the infinite set of equations. For the lasing and thermal regimes, this approximation can be expected to be very accurate, thanks to the weak and indirect interactions between modes or emitters, and it further allows us to assume

$$\left\langle \sigma_{\vec{r}}^\dagger \sigma_{\vec{s}} \right\rangle \approx n_\sigma \delta_{\vec{r},\vec{s}} \quad \text{and} \quad \left\langle p_{\vec{k}}^\dagger p_{\vec{q}} \sigma_{\vec{r}}^\dagger \sigma_{\vec{r}} \right\rangle \approx n_{\vec{k}} n_\sigma \delta_{\vec{k},\vec{q}} \tag{4.16}$$

where indexes $\vec{r}$ and $\vec{s}$ label emitters and $\vec{k}$ and $\vec{q}$ label Bloch modes. We have numerically verified the validity of this approximation by including correlations between emitters in distant cavities.

For the steady state we find

$$0 = -\gamma_a n_{\vec{k}} + F_{\vec{k}} n_{\vec{k}}(2n_\sigma - 1) + F_{\vec{k}} n_\sigma, \tag{4.17a}$$

$$0 = P_\sigma - (P_\sigma + \gamma_\sigma + F)n_\sigma - (2n_\sigma - 1)\tilde{F}, \tag{4.17b}$$

with $F = N^{-m}\sum_{\vec{k}} F_{\vec{k}}$ and $\tilde{F} = N^{-m}\sum_{\vec{k}} F_{\vec{k}} n_{\vec{k}}$. The polarizations are then given by

$$\left\langle p_{\vec{k}}^\dagger \sigma_{\vec{r}} \right\rangle = iG_{\vec{k}\vec{r}}(n_\sigma - n_{\vec{k}} + 2n_{\vec{k}} n_\sigma)/(\Gamma/2 + i\Delta_{\vec{k}}) \tag{4.18}$$

and the local cavity populations by $n_a = N^{-m}\sum_{\vec{k}} n_{\vec{k}}$. Eq. (4.17a) can be solved for $n_{\vec{k}}$ to find

$$n_{\vec{k}} = \frac{\kappa_\sigma \Gamma}{4} \frac{n_\sigma}{(\delta/2)^2 + \Delta_{\vec{k}}^2} \tag{4.19}$$

with $\delta^2 = \kappa_\sigma \Gamma\,[\Gamma/\kappa_\sigma - (2n_\sigma - 1)]$ and $\kappa_\sigma = 4g^2/\gamma_a$, the Purcell enhanced decay of an emitter through its local cavity [61]. The distribution of Bloch mode populations is thus a Lorentzian in $\Delta_{\vec{k}}$ with width δ.

The central quantity of interest in our investigation are the normalized correlations between cavity fields in distant cavities. Thanks to the translational invariance in the array (which leads to linear momentum conservation), the Bloch mode correlations vanish, $\left\langle p_{\vec{k}}^\dagger p_{\vec{q}} \right\rangle = \delta_{\vec{k},\vec{q}} n_{\vec{k}}$, and the cavity correlations are simply the Fourier transform of the Bloch mode populations $n_{\vec{k}}$,

$$\mathcal{C}(\vec{r}) = \frac{\left\langle a_{\vec{0}}^\dagger a_{\vec{0}+\vec{r}} \right\rangle}{\left\langle a_{\vec{0}}^\dagger a_{\vec{0}} \right\rangle} = \frac{1}{n_a N^m} \sum_{\vec{k}} e^{-i\vec{k}\cdot\vec{r}} n_{\vec{k}}\,. \tag{4.20}$$

In the following sections we study in detail how the emitters are correlated.

5. ASYMPTOTICS OF CORRELATIONS

We first summarize the main results concerning the asymptotics of the correlations between different cavities. Inserting Eq. (4.19) into Eq. (4.20), we find that the correlations $\mathcal{C}(\vec{r})$ decay faster than r^{-n} as $r \to \infty$, where $r = |\vec{r}|$, for any positive integer n and lattice dimension m, provided $\delta \neq 0$. The proof of this statement proceeds by showing, via multiple applications of the divergence theorem, that for any power n, $r^n \mathcal{C}(\vec{r}) \to 0$ as $r \to \infty$ (as we show below in Sec. 5.1). The only possibility for the system to become critical, in the sense that the correlation length of $|\mathcal{C}(\vec{r})|$ diverges, would be that δ vanishes, i.e. that $\Gamma/\kappa_\sigma = (2n_\sigma - 1)$. It is however easily seen that the last term in Eq. (4.17b) diverges for $N \to \infty$ unless $(2n_\sigma - 1) \to 0$, which, for $\delta = 0$, would imply $\gamma_a = 0$. We, therefore, conclude that any non-vanishing photon decay rate keeps the correlation length finite and thus prevents criticality. On the other hand, in the lasing regime, the higher the cavity quality the longer the correlation length, because a small δ narrows the distribution of the n_k around the resonant mode, corresponding to long correlations in real space (as illustrated in Sec. 5.2). These findings are in stark contrast to closed equilibrium systems where, according to the Mermin-Wagner-Hohenberg theorem [105, 106], arbitrarily long correlation lengths are ruled out for $m = 1, 2$ at non-zero temperatures.

5.1 Proof of fast decay of correlations

For proving the above statement, we consider the thermodynamic limit of a rectangular m-dimensional lattice of cavities, i.e., where infinitely many cavities are arranged in each lattice direction. We thus have a continuum of momentum modes and $\frac{1}{N^m}\sum_{\vec{k}}$ turns into an integral over the Brillouin Zone V_k formed by the m-dimensional cube extending from $-\pi$ to π in each direction. The field correlations are then given by

$$\mathcal{C}(\vec{r}) = \frac{1}{n_a\,(2\pi)^m} \int_{V_k} d^m k e^{-i\vec{k}\vec{r}} n(\vec{k}), \tag{5.1}$$

with $\vec{r}$ running on the lattice of m-dimensional vectors with integer coordinates.

For $\delta^2 > 0$, $n(\vec{k})$ is a continuous function of k defined on a finite domain, and therefore it is integrable over V_k. In this case the Riemann-Lebesgue lemma [107] ensures that $\mathcal{C}(\vec{r})$ decays to zero for $\vec{r} \to \infty$. The result we want to show is that this decay is actually faster than any power of r. The proof relies essentially on the fact that $n(\vec{k})$ depends on $\vec{k}$ through cosine functions of the components of $\vec{k}$. As such, $n(\vec{k})$ and all its derivatives are continuous and periodic functions of $\vec{k}$. By periodicity here we mean invariant with respect to translations by reciprocal lattice vectors, i.e. $n(\vec{k}) = n(\vec{k} + \vec{K})$, where the coordinates of $\vec{K}$ are integer multiples of 2π. In particular, on the surface of the BZ one finds pairwise opposite points, differing by a reciprocal lattice vector. It follows that in such points $n(\vec{k})$ has equal values, and the same is true for all its derivatives.

For the proof we denote by $\alpha = \{\alpha_1, \alpha_2 \dots \alpha_m\}$ a multi-index of natural numbers and by $|\alpha|$ the sum of its components $\alpha_1 + \dots \alpha_m$. We denote also by r^α the quantity $r_1^{\alpha_1} r_2^{\alpha_2} \dots r_m^{\alpha_m}$. The result we want to show is that for any α one has $r^\alpha \mathcal{C}(\vec{r}) \to 0$ when $r \to \infty$.

Indeed, multiplying the integral in Eq. (5.1) with r^α amounts to applying the derivative operator $(i\partial)^\alpha = i^{|\alpha|} \partial_1^{\alpha_1} \dots \partial_m^{\alpha_m}$ to the plane-wave factor $e^{-i\vec{k}\vec{r}}$ under the integral. By ∂_i we mean the derivative with respect to k_i. All these derivatives can be transferred upon $n(\vec{k})$ by repeatedly applying the divergence theorem. At each such step, Brillouin Zone surface integrals are generated. But each of these integrals vanishes, because it involves pairwise equal values of the integrand at the opposite points of the Brillouin Zone surface. The outer normals to the surface in such points have opposite orientation and this ensures the cancellation. Note that in this argument both the periodicity of the derivatives of $n(\vec{k})$ and that of $e^{-i\vec{k}\vec{r}}$ are required. The latter is ensured by $\vec{r}$ having integer coordinates.

After transferring all the derivatives one is left with

$$r^\alpha \mathcal{C}(\vec{r}) = \frac{(-i)^{|\alpha|}}{n_a \, (2\pi)^m} \int_{V_k} d^m k e^{-i\vec{k}\vec{r}} \partial^\alpha n(\vec{k}) \,. \tag{5.2}$$

Since the integrand is again a continuous function, the Riemann-Lebesgue lemma can be invoked again, ensuring that, indeed, $r^\alpha \mathcal{C}(\vec{r})$ goes to zero for large values of the argument. This concludes the proof.

The only possibility that the correlation length could diverge is thus a case where $(2n_\sigma - 1) = \Gamma/\kappa_\sigma$, for which $n_{\vec{k}} \propto \Delta_{\vec{k}}^{-2}$. For this case, however,

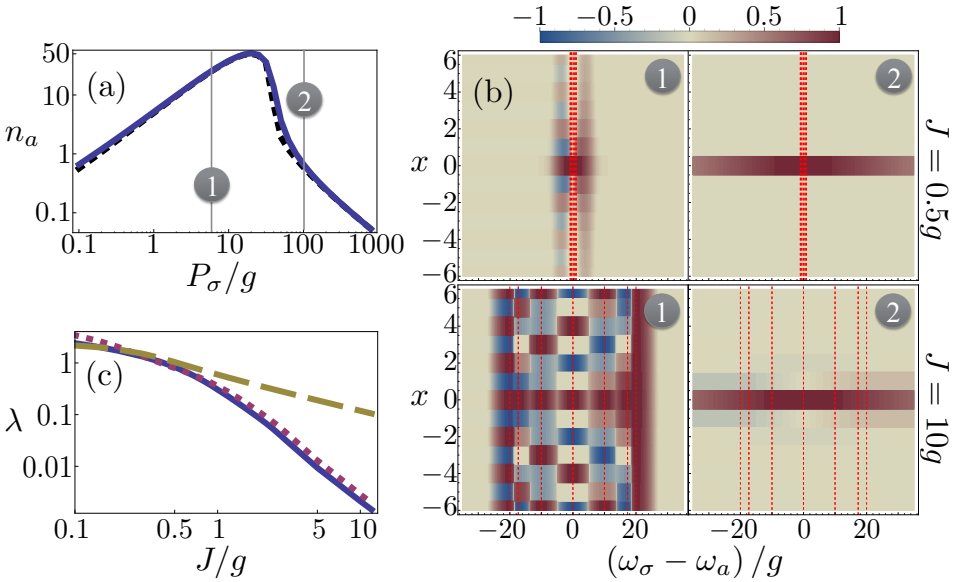

Fig. 5.1: (a) Cavity population n_a for $\omega_\sigma = \omega_a$ as a function of pump P_σ for $J = 0.5g$ (solid blue) and $J = 10g$ (dashed black), with $N = 12$, $\gamma_a = 0.1g$, $\gamma_\sigma = 0.01g$. (b) Corresponding first order correlations $\mathcal{C}(x)$ as a function of distance x and emitter frequency ω_σ at pump rates (1) and (2) in plot (a). Bloch mode resonances are plotted as vertical dashed red lines. (c) Inverse correlation lengths, λ, as obtained from fits (see main text) for $N = 108$, $P_\sigma = 5g$, and $\Delta = 0$ (solid), $\Delta = J$ (dotted) or $\Delta = 2J$ (dashed).

the last term in Eq. (4.17b), which reads $(2n_\sigma - 1)\frac{1}{n_a(2\pi)^m}\int_{V_k} d^m k F_{\vec{k}} n_{\vec{k}}$, diverges as long as $(2n_\sigma - 1) \neq 0$. The origin of this divergence is that $\Delta_{\vec{k}}^{-2}$ at least scales as $\Delta_{\vec{k}}^{-2} \propto (k_\alpha - \overline{k}_\alpha)^{-2}$ in the vicinity of a manifold $\overline{k}$ where $\Delta_{\vec{k}} = 0$ (if $\Delta_{\vec{k}} = 0$ occurs at the boundary of the integration volume the divergence is even more severe). We thus conclude that non-exponential decay or a divergent correlation length can only appear for $\delta = 0$ and $(2n_\sigma - 1) = 0$. Both conditions can only hold for $\gamma_a = 0$, i.e. if the photon decay vanishes.

5.2 Correlations in one dimension (1D)

We now examine correlations in a 1D chain, $\mathcal{C}(x)$ with $-N/2 \leq x \leq N/2$, Eq. (4.20), considering N to be a multiple of 4, so that the Bloch modes are distributed symmetrically around the cavity frequency. We first focus on $N = 12$ with $J = 0.5g$ or $10g$, for which we show n_a as a function of the pump in Fig. 5.1(a). Both cases undergo very similar and characteristic transitions into and out of lasing (c.f. Fig. 4.6(i)). We select two pumping rates representative of the lasing (1) and thermal (2) regimes and plot $\mathcal{C}(x)$ as a function of the detuning $\Delta = \omega_\sigma - \omega_a$ and the separation x between the cavities in Fig. 5.1(b). For $|\Delta| < 2J$, $\mathcal{C}(x)$ oscillates as $\cos(\overline{k}x)$, where $\overline{k}$ and $-\overline{k}$ are the (degenerate) modes closest to resonance with the emitters, i.e. $|\Delta| \approx 2J\cos\overline{k}$. The correlation length is longer in the lasing regime (1), increases for larger J and becomes maximal for $|\Delta| = 2J$ in each case, i.e., when the emitters are in resonance with the edges of the Bloch band. For $J = 10g$ it becomes larger than the finite size array of $N = 12$ considered here since the frequency separation between Bloch modes is so large that the emitters only populate one mode efficiently. Note that any decay of correlations is entirely due to destructive interference between different Bloch-mode contributions.

Let us now explore $|\Delta| \leq 2J$, where the emitters are on resonance with the Bloch band and the photonic modes are appreciably populated. For a long chain, $N \gg 1$, and large tunneling rates, $J \gg g$, analytical estimates can be found for the correlations $\mathcal{C}(x)$ (see the Appendix E). In agreement with Fig. 5.1, these show exponential decay modulated by an oscillation. We thus fit a function $f(x) = [c_1\cos(\nu x) + c_2\sin(\nu x)]\exp(-\lambda x)$ to $\mathcal{C}(x)$ in the entire range of tunneling rates J and extract the inverse correlation length, λ, from the fit (see the Appendix E for examples). Fig. 5.1(c) shows λ for three cases: $\Delta = 0$ (solid), $\Delta = J$ (dotted) and $\Delta = 2J$ (dashed) for a chain of $N = 108$ cavities, which has Bloch modes in resonance with the emitters for all considered values of Δ so that finite-size effects are suppressed. As a second main result of our work we observe a clear transition from the regime with $J < g$, where $\lambda \propto -\ln J$, to the regime $J > g$, where $\lambda \propto J^{-1}$ for $J \gg |\Delta|$ and $\lambda \propto J^{-1/2}$ for $2J = |\Delta|$. These behaviors are also found from analytical estimates for $N \to \infty$ (the details of the derivations are provided in the Appendix E).

6. LOCAL PROPERTIES IN 1D CHAINS

We present some experimentally observable and distinctive local signatures of the collective lasing regime in the array, as a function of Δ. In Fig. 6.1(a)–(i) we plot n_a and n_σ, computed from Eqs. (4.17), for various arrays. Each underlying Bloch mode n_k enters its own lasing regime at $\omega_\sigma = \omega_k$. Resonance results in the enhancement of n_a to a fixed value, given by the resonant one-emitter case n_a^{L}, while the emitter population decreases to $n_\sigma^{\mathrm{L}} \approx 1/2$ from its saturation value of 1 [1]. Note that these traits are independent of g, N and J once the system is strongly enough coupled to reach the lasing regime [108]. With these conditions we compare various arrays, i.e. $N = 4$, 12, 32 and $J/g = 0.5$, 10, 50, and the one-emitter laser (showing n_a only for that case), see Fig. 6.1. Interactions as small as $J \lesssim 0.5g$ (Fig. 6.1 upper row) are not enough to make a qualitative difference from the $N = 1$ case in the local populations [2]. The width in detuning of the apparent single broad resonance is given by $2\Delta_{\max} = \sqrt{P_\sigma(\kappa_\sigma - P_\sigma)}$ [3]. Increasing interactions, $J > g$ (other rows), splits the Bloch modes apart so that they can be selectively addressed by changing detuning. The excitation is distributed equally among the driven modes so, at resonance, $n_{k=0,\pi} = N n_a^{\mathrm{L}}$ and $n_{\pm k} = N n_a^{\mathrm{L}}/2$ for the other central modes. This results in a series of peaks for n_a of equal height n_a^{L} and width $2\Delta_{\max}$. When the width is smaller than the average separation between Bloch modes, approximately given by $4J/N$ (or $4J/(N-1)$ for odd N), a plateau forms in the populations that extends for $|\Delta| \leq 2J$, c.f. Fig. 6.1(f). At this point, increasing N does not affect the results qualitatively.

Another very distinctive feature of the collective lasing is provided by the emitter photoluminescence spectrum $S(\Gamma_d, \omega)$, where Γ_d is the detector linewidth. In order to compute it, we make the semiclassical approximation

[1] Also $g^{(2)} \approx 1$, although our rate equations do not provide this information

[2] The rate equations provide for this case an analytical solution, c.f. Eq. (10) in the Appendix D.

[3] Estimation obtained by solving $n_a \approx n_a^{\mathrm{L}}[1 - \frac{P_\sigma}{\kappa_\sigma}(1 + (\frac{2\Delta}{P_\sigma})^2)] = 0$ in the detuned one-emitter laser [61].

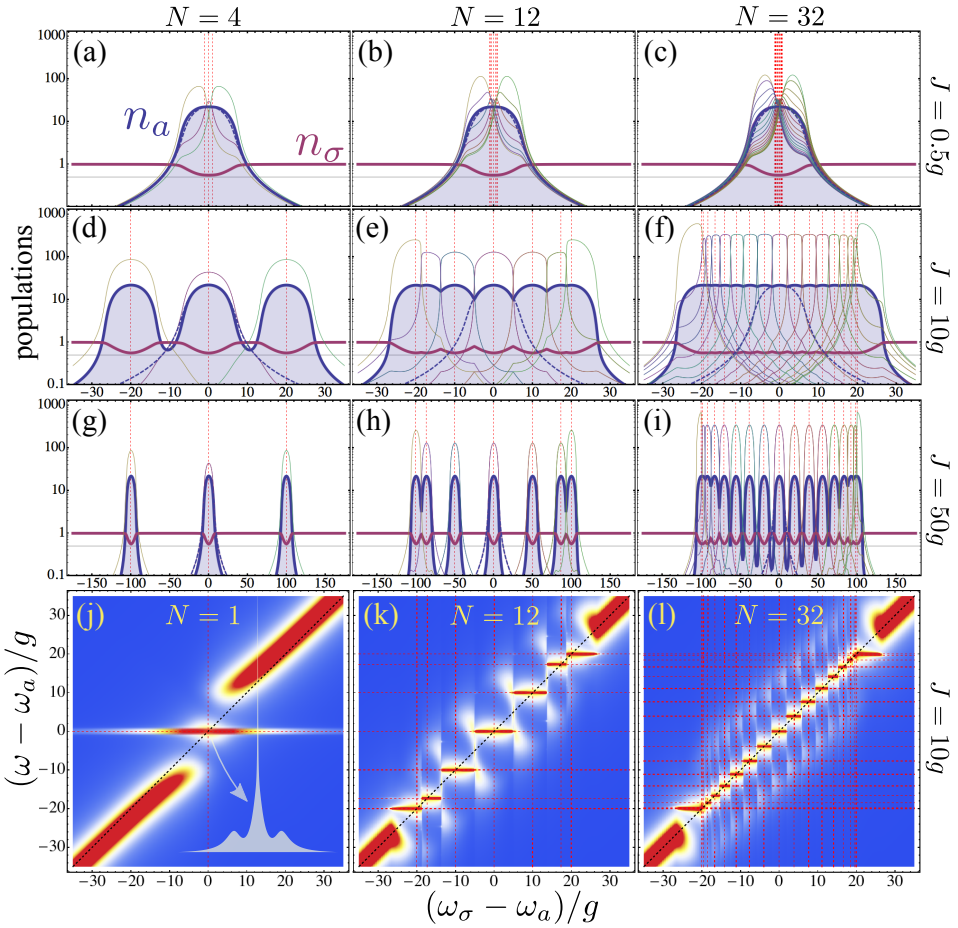

Fig. 6.1: (a)–(i) Populations of the different modes involved, when sweeping the emitter frequency ω_σ through the system resonances (vertical red dashed lines): n_a in solid and filled blue, n_σ in solid pink, the Bloch modes n_k with thin lines and n_a for the case $N = 1$ in dashed blue as a reference. (j) Emitter spectrum of emission for $N = 1$ and varying ω_σ, showing a Mollow triplet around resonance. In inset, the lineshape at resonance. In (k) and (l), the spectra for cases (e) and (f), respectively. We use a temperature color code which goes from blue (0) to red (maximum values). Parameters are $N = 4$, 12, 32 and $J = 0.5g$, $10g$, $50g$, varying as indicated. Also: $P_\sigma = 5g$, $\gamma_a = 0.1g$, $\gamma_\sigma = 0.01g$, $\Gamma_d = 0.3g$.

that consists substituting the cavity fields by a multimode laser that acts independently on each of the emitters. That is, we consider the approximated Hamiltonian

$$H_{\mathrm{ML}} = \sum_{\vec{r}} [\omega_\sigma \sigma^\dagger_{\vec{r}} \sigma_{\vec{r}} + \Omega(t)\sigma^\dagger_{\vec{r}} + \Omega^*(t)\sigma_{\vec{r}}], \tag{6.1}$$

where $\Omega(t) = \sum_{\vec{k}} g\sqrt{n_{\vec{k}}/N} e^{-i\omega_{\vec{k}} t}$ is the time-dependent multimode field. Additionally, the emitters are still being excited by the incoherent pump and decay, through the usual Lindblad forms.

There is no steady state for this approximated model (for $N > 1$) but a quasi-steady state, that is, an ever oscillating solution for the density matrix elements around a mean point. Such mean point is given (approximately) by the exact solution of the full master equation or the rate equations, which do have a steady state. That is, $\sum_{\vec{k}} G_{\vec{k}\vec{r}} \left\langle p_{\vec{k}} \sigma^\dagger_{\vec{r}} \right\rangle e^{-i\omega_{\vec{k}} t}$ is well estimated by $\Omega(t) \left\langle \sigma^\dagger_{\vec{r}} \right\rangle_{\mathrm{ML}}$, where $\langle\cdot\rangle_{ML}$ is the mean value obtained with the approximated master equation and Hamiltonian H_{ML} for the emitters only. The fact that the first term is $\vec{r}$-independent, compels $\Omega(t)$ to be $\vec{r}$-independent as well. We describe the resulting time-dependent dynamics in the following way: First, we solve the new master equation with H_{ML}, and obtain its time-dependent spectrum of emission [109, 110], $S_{\mathrm{ML}}(\Gamma_d, \omega, t)$, by coupling the emitter very weakly to another two-level system, which radiatively decays at a rate Γ_d, and plays the role of the detector. The population of this detector is exactly the time-dependent spectrum of our emitter [111]. Then, we take its average over time, once the quasi-steady state is reached, starting at a point in time which we call t_0: $S(\Gamma_d, \omega) \approx \int_{t_0}^{t_0+T} S_{\mathrm{ML}}(\Gamma_d, \omega, t)dt/T$. This is a very good approximation in the case $N = 1$ [61, 75] for which there is a simple analytical formula [112].

Despite the incoherent pump, a Mollow triplet forms [61, 75, 112, 113] whenever $\omega_\sigma = \omega_k$ for some k, thanks to the effective multi-Bloch-mode coherent drive $\Omega(t)$. In Fig. 6.1(j)–(l), we compare $N = 1$, 12 and 32, for varying Δ. The Rayleigh peak, produced by the elastically scattered cavity laser field, is pinned at the cavity frequency for a single mode excitation (j), with small linewidth given by the detector only Γ_d (as in this approximation the cavity has an infinitely long lifetime). In the multimode case, Figs. 6.1(k), (l), the Rayleigh peak jumps from Bloch mode to Bloch mode, depending on which one dominates, in correspondence with the population plateaus of Fig. 6.1(e), (f). The sidebands are positioned at $\omega_k \pm 2\sqrt{2}g\sqrt{n_a^{\mathrm{L}}}$, around resonance with a degenerate Bloch mode ω_k, and at $\omega_k \pm 2g\sqrt{n_a^{\mathrm{L}}}$, with

the edge modes. Therefore, high N and closely packed Bloch modes give rise to two Mollow continuous sidebands at $\omega_\sigma \pm 2\sqrt{2}g\sqrt{n_a^{\mathrm{L}}}$, extending over $|\Delta| \leq 2J$.

IV

DISSIPATIVE STRUCTURES IN OPTOMECHANICAL CAVITIES

7. INTRODUCTION

7.1 Classical and quantum phenomena in cavity optomechanics: Bistability, squeezing, cooling

The idea that light carries momentum and can therefore exert a pressure was first proposed by Kepler in the 17th century and later elaborated on by Newton. Maxwell's 1873 theory of light as electromagnetic waves implied that light does indeed carry both momentum and energy, but the predicted forces were so small that it was generally believed that radiation pressure effects could be ignored in macroscopic situations. The first unambiguous experimental demonstrations of the radiation pressure force predicted by Maxwell were performed, in 1901, using a light mill configuration [114, 115]. Some years later, in 1909, Einstein derived the statistics of the radiation pressure force fluctuations acting on a movable mirror, which allowed him to reveal the dual wave-particle nature of blackbody radiation. In pioneering experiments, both the linear and angular momentum transfer of photons to atoms and macroscopic objects were demonstrated in the decade of the 1930's by Frisch and Beth [116, 117]. This situation changed drastically, in the 1960's, with the invention of the laser. The high degrees of spectral purity and spatial coherence allowed laser beams to be focused to very small spot sizes, thus creating very high intensities over small areas, which was an open gate for new possibilities. That is the case of optomechanics, which comes from the interaction through radiation pressure between light and some mechanical degree of freedom.

To understand the effects of radiation pressure consider the simplest such device, a two-mirror system (Fabry-Perot cavity) in which one of its mirrors is movable according to the dynamics of a harmonic oscillator with frequency Ω_0 (Fig. 7.1). As is well known, the internal fields stored in a high-finesse Fabry-Perot cavity ($\mathcal{F}$ [1]) can be orders of magnitude greater than the input

[1] The cavity finesse is defined by $\mathcal{F} = \Delta_{\mathrm{FSR}}/\gamma$, where Δ_{FSR} is the frequency separation between modes of the cavity (free spectral range), and γ the leaking rate of photons out of the cavity

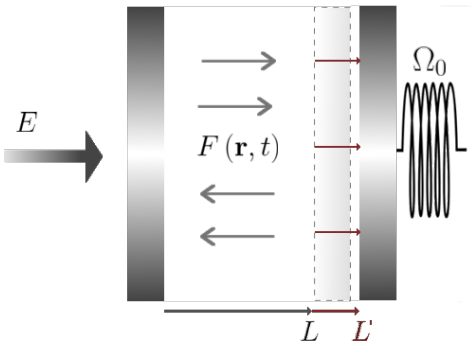

Fig. 7.1: Scheme of the optomechanical system explained in the text.

field injected (E). For sufficiently high internal fields radiation forces can change the physical length of the cavity ($L' > L$), and therefore, decrease the cavity frequency. In turn, any change in the cavity frequency will affect its internal field. Thus, radiation pressure forces introduce a nonlinearity in the two mirror system.

Since the middle 1980's, the subject has received a lot of attention due to its direct correspondence with systems with Kerr media [118], a system widely studied at that moment which consists in a cavity containing a nonlinear medium having an intensity dependent refractive index.

Besides that, the optomechanical cavity has the additional feature of having its own mechanical degrees of freedom, and the mechanical dynamics, as we will see, allows to study the transition between the classical and quantum descriptions as the quantum regime is nowadays experimentally accessible. In order to get a picture of the possibilities of optomechanical systems, next we explain some of its main classical and quantum features.

Classically, it is well known that Kerr nonlinearities provide a mean for making bistable optical devices. The first observation of a bistable response in optomechanics was reported in [119] in 1983. The system used was a plane Fabry-Perot interferometer in which one of its mirrors was suspended so that it could swing as a pendulum. Two years later, the full theoretical analysis was given in [120] for two and three mirror systems. In the later, the pendulum mirror was suspended between two fixed mirror, and therefore, radiation pressure forces acted from both sides.

During the 1990's, several aspects of quantum cavity optomechanical systems started to be explored theoretically. These include squeezing

of light [121, 122] and quantum non-demolition (QND) detection of light intensity [123] and [124]. But at that moment, the experimental state of the art was not advanced enough. We had to wait until 2012 to see the generation of squeezed light in cavity optomechanics [125]. On the other hand, [126] demonstrated that the state of the radiation field interacting with a macroscopic object can become nonclassical at a level deeper than simple squeezing. Namely, the appearance of EPR aspects (see section 1.2.2) on continuous variables in that system; as well as the possibility of entangling macroscopic oscillators exploiting radiation pressure (e.g., movable mirrors) was proposed in [127], which somehow brings quantum mechanics to our macroscopic world. In this direction, cooling of mechanical resonators close to their quantum ground state has become an important topic for various fields of physics in the last years [128–131]. Cooling has been achieved by exploiting in two different ways the radiation-pressure interaction between a mechanical mode and the intracavity field: (i) by back-action, or self-cooling, in which the off-resonant operation of the cavity results in a retarded back-action on the mechanical system and hence in a "self"-modification of its dynamics; and by cold-damping quantum feedback, where the oscillator position is measured through a phase-sensitive detection of the cavity output and the resulting photocurrent is used for a real-time correction of the dynamics.

As for actual optomechanical implementations, they come out in many different forms [11]: cavities with mirrors attached to cantilevers or suspended, whispery gallery mode resonators, drumshaped capacitors coupled to superconducting circuits, or localized mechanical modes in photonic crystal cavities, are some examples. For our current purposes, the most relevant implementation consists in a flexible membrane placed inside an optical cavity, where light will push it from both sides making it vibrate like a drum, as we will discuss towards the end of the chapter.

Summarizing, there are several different motivations that drive the rapidly growing interest into cavity optomechanics. On the one side, there is the highly sensitive optical detection of small forces, displacements, masses, and accelerations. On the other hand, cavity quantum optomechanics promises to manipulate and detect mechanical motion in the quantum regime using light, creating nonclassical states of light and mechanical motion. These tools will form the basis for applications in quantum information processing, where optomechanical devices could serve as coherent light-matter interfaces, for example to interconvert information stored in solid-

state qubits into flying photonic qubits. Another example is the ability to build hybrid quantum devices that combine otherwise incompatible degrees of freedoms of different physical systems. At the same time, it offers a route towards fundamental tests of quantum mechanics in an hitherto unaccessible parameter regime of size and mass.

7.2 Complex nonlinear phenomena in cavity optomechanics

In the previous section we have seen that optomechanical cavities are particularly attractive from a purely *quantum* point of view. However, this is not their only appealing. They are dynamical (dissipative) nonlinear optical cavities and as such, they can exhibit complex nonlinear phenomena beyond optical bistability. The can show complex temporal behaviour such as dynamical bifurcations, self-oscillations, chaotic dynamics, and also spatial (spatiotemporal) complexity such as spontaneous appearance of *dissipative structures*. From this viewpoint cavity optomechanics is a new system to add to the well established field of nonlinear dynamics with its well established mathematical (analytical and numerical) tools and techniques; however the possibility of observing these typically *macroscopic* phenomena near the border with the quantum world makes this special system particularly appealing.

Temporal complexity soon attracted attention in the cavity optomechanics community, but we shall not pay attention to these developments here (see [132–135]). In this regard we must also mention the theoretical analyses made on arrays of coupled optomechanical systems in which complex collective phenomena may also appear (see [136]). In this work, we concentrate on the possibility of observing dissipative structures in large area optomechanical cavities, a possibility that seemingly has not been considered prior to us (except in the frame of cold atomic gases [137–139]).

Extended nonlinear systems with large aspect ratios (much bigger in the transverse direction) tend to loose the spatial homogeneity when brought apart enough from thermal equilibrium. This is a universal phenomenon as it appears in all known spatial scales, from galaxy formation to morphogenesis (for which Turing formulated his celebrated reaction-diffusion model [140] that has since played a paradigmatic role in pattern formation) and consists in the appearance of a macroscopic order with specific spatial scales that leads to the formation of periodic or quasiperiodic structures such as fingerprints, the stripes on the skin of a tiger or zebra, the spots on the

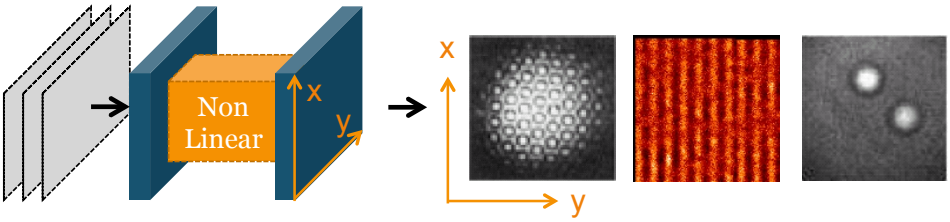

Fig. 7.2: Spontaneous symmetry breaking in the transverse plane. Hexagonal, striped patterns and localized structures (Figures taken from [150])

skin of a leopard, the dunes in a desert, long range structures that can also exhibit temporal complexity. But not only this, as also localized structures may appear, structures whose dynamics is somewhat independent from that of other separated structures within the same system. For general and well known introductions to the field of dissipative structures see [141–143].

The study of dissipative structures in optics goes back to the very early days of the laser era as laser cavities with large mirrors may sustain a large number of transverse modes whose combination leads to the formation of complicated patterns [144]. However during the late sixties and early seventies of the past century, and specially from 1975 on, when Haken's influential paper connecting the laser model and the Lorenz model appeared [145], the optics community concentrated on the understanding of complex temporal phenomena, specially chaos [146–148], and no real attention was paid to the issue of patterns from the point of view of nonlinear dynamics till the mid 1980's when several papers appeared connecting the mathematical description of nonlinear optical cavities with the broader field of pattern formation [149, 150]. The early predictions of optical vortices, hexagonal patterns, and localized structures were soon experimentally confirmed and the community concentrated mainly in the study of cavity solitons.

Cavity solitons are localized structures that can appear in nonlinear optical cavities and in order to define them let us reflect on how these systems must be. A very necessary and obvious condition for pattern formation is that the system under study can sustain a very large number of different spatial modes, hence nonlinear optical cavities must have a large enough transverse size (a large Fresnel number), or aspect ratio, for sustaining enough transverse modes. The most ideal possibility is that of having a single longitudinal mode cavity (so that we can forget about the

axial coordinate z) and having large plane mirrors on the $x-y$ plane and, interestingly, the experimental implementation of such system is perfectly possible [151]. This cavity is excited homogeneously, e.g. by injecting a suitable coherent plane-wave field in the cavity in the case of DOPOs or of Kerr or photorefractive cavities, or by pumping homogeneously as in lasers, in order to study *spontaneous* pattern formation. It is spontaneous because it spontaneously appears in systems that under plane illumination hold the symmetry under translational invariance in the transverse plane (x, y), Fig. 7.2. The patterns, or dissipative structures, form in the $x-y$ plane, stripes or hexagons being the most common ones. Localized structures manifest as local excitations of small size and they are termed cavity solitons when they can be locally addressed (written or erased) without affecting other neighboring localized structures. Such cavity solitons could have applications in information storage and manipulation and their study is a well established subfield [152, 153].

Here we shall address the problem of pattern formation in large aspect ratio optomechanical cavities by proposing mathematical models that could be experimentally implemented with present day technology. While here we keep our study at the classical level, what we demonstrate is that patterns and cavity solitons could be observed probably near the classical-quantum border and we leave to future work the study of the quantum properties of the structures, which we find interesting because quantum phenomena similar to those that have been predicted for degenerate optical parametric oscillators [36, 154, 155], and that cannot be experimentally observed with state of the art technology, could be finally observed in optomechanical cavities

7.3 Derivation of the model

In this section we explain the derivation of the equations of the multimode description of the system.

Consider now the situation in which the cavity is formed by two fixed–mirrors, with a locally deformable membrane placed somewhere between them. The latter can be thought of as a tense transparent membrane that can oscillate, forced by the intracavity radiation pressure, not only back and forth around its axial equilibrium position (center of mass motion) but also in its transverse degrees of freedom, vibrating like a drum in combinations of modes. The movement of the center of mass will be modelled

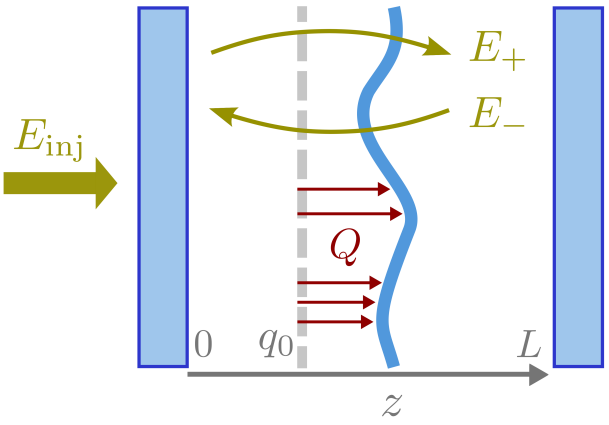

Fig. 7.3: Sketch of the system where $Q \equiv Q(\mathbf{r}, t)$, $E_{\text{inj}} \equiv E_{\text{inj}}(z, \mathbf{r}, t)$, $E_\pm \equiv E_\pm(z, \mathbf{r}, t)$

as a homogeneous mode (independent of the transverse coordinates) while the modes deforming the flatness of the membrane will be modelled as the nondispersive surface waves occurring in a tense membrane.

Energy is fed in to the cavity from the outside by injecting an optical monochromatic plane-wave ($E_{\text{inj}}(z, \mathbf{r}, t)$ with $\mathbf{r} = (x, y)$) through the partially transmitting mirror. We denote by $z = 0, L$ the planes (x, y) containing the coupling mirrors and $z = q_0$ the membrane surface at rest (i.e., in the absence of illumination). In Fig. 7.3 there is a sketch of the system. Two optical waves, $E_\pm(z, \mathbf{r}, t)$, travelling to the right/left are transmitted by and reflected from the membrane displacing it by $Q(\mathbf{r}, t)$.

We consider first the equation for the light field, which we derive following the usual approach of propagating the field along the resonator. We will assume that any modification of the field along a cavity roundtrip (due to diffraction and to transmission and reflection on the membrane or on the cavity mirrors) is small. This means that we are considering (i) short enough propagation distances (either geometrically small, or optically small: think of a quasi self-imaging resonator), and (ii) almost transparent membranes, with a very small reflectivity $\varrho \ll 1$. We treat the deformable membrane as a thin, lossless symmetric beam splitter, with (complex) transmission and reflection coefficients denoted by $\tau_\pm$ and $\varrho_\pm$, where the subscript refers to the side of the membrane (+ for right and − for left).

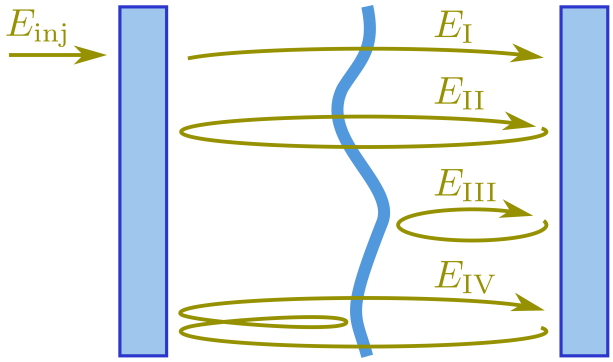

Fig. 7.4: Processes considered for the calculation of $E_+(L,\mathbf{r},t)$

As in any lossless beam splitter [156]

$$\arg(\varrho_+) + \arg(\varrho_-) - \arg(\tau_+) - \arg(\tau_-) = \pi, \tag{7.1}$$

while further for a symmetric one,

$$|\tau_\pm| = \tau, \quad |\varrho_\pm| = \varrho. \tag{7.2}$$

Remind that we consider $\varrho \ll 1$, hence $\tau = \sqrt{1-\varrho^2} = 1 + O(\varrho^2)$. We will denote by $r_{1,2}$ the reflection coefficients of the left/right cavity mirrors ($|r_{1,2}|^2$ are the corresponding reflectivities, which are assumed very close to unity: good cavity limit). The left(right) mirror is located at $z = 0\,(L)$, while in the asbence of illumination the membrane has an equilibrium position at $z = q_0$. In the presence of optical fields any point $\mathbf{r}$ of the membrane will be shifted along the cavity axis by $Q(\mathbf{r},t)$ from the equilibrium. We choose arbitrarily to derive the evolution equation for the field $E_+(L,\mathbf{r},t)$ impinging the right cavity mirror, which is assumed to be the outcoupling mirror, i.e. the one with larger (albeit small) transmission. The input field is assumed here to be injected through the left mirror (of smaller transmission), as this is the best setup for reducing deleterious effects of the vacuum noise in a double-sided cavity [18], even if we do not consider quantum effects in this work.

The presence of the intracavity membrane makes the problem a bit complicated because the field $E_+(L,\mathbf{r},t)$ is given, at any instant, as the superposition of infinitely many contributions, corresponding to waves that, after different combinations of transmissions and reflections paths, had left

the right mirror at previous times. However, as the membrane reflectivities $\varrho_{\pm}$ are assumed small, $E_+(L,\mathbf{r},t)$ can be approximated at any instant as the sum of just four partial waves, as sketched in Figure 7.4: (I) the injected field transmitted by the membrane (call it E_{I}), (II) the field that, after reflection on the right cavity mirror, has performed a full cavity roundtrip just by transmitting through the membrane (call it E_{II}); (III) the field that, after reflection on the right cavity mirror, relfects back from the right face of the membrane (call it E_{III}); and (IV), the field that, after transmission through the membrane and reflection on the left cavity mirror, has reflected from the left side of the membrane, reflected again from the left mirror, and finally transmitted by the membrane (call it E_{IV}). Any other partial wave has an amplitude on the order of ϱ^2 or smaller, which we neglect. Hence we write

$$E_+(L,\mathbf{r},t) = E_{\mathrm{I}}(\mathbf{r},t) + E_{\mathrm{II}}(\mathbf{r},t) + E_{\mathrm{III}}(\mathbf{r},t) + E_{\mathrm{IV}}(\mathbf{r},t)\,, \tag{7.3}$$

where the four partial waves can be written as

$$E_{\mathrm{I}}(\mathbf{r},t) = K_{\mathrm{I}}\mathcal{U}_L E_{\mathrm{inj}}(0,\mathbf{r},t-t_{\mathrm{c}}/2)\,, \tag{7.4a}$$
$$E_{\mathrm{II}}(\mathbf{r},t) = K_{\mathrm{II}}\mathcal{U}_{2L} E_+(L,\mathbf{r},t-t_{\mathrm{c}})\,, \tag{7.4b}$$
$$E_{\mathrm{III}}(\mathbf{r},t) = K_{\mathrm{III}}\mathcal{U}_{L_2} e^{-2\mathrm{i}k_{\mathrm{L}}Q(\mathbf{r},t-t_2)}_{L_2}\mathcal{U}_{L_2} E_+(L,\mathbf{r},t-2t_2)\,, \tag{7.4c}$$
$$E_{\mathrm{IV}}(\mathbf{r},t) = K_{\mathrm{IV}}\mathcal{U}_{L+L_1} e^{2\mathrm{i}k_{\mathrm{L}}Q(\mathbf{r},t-t_{\mathrm{c}}/2-t_1)}\mathcal{U}_{L+L_1} E_+(L,\mathbf{r},t-t_{\mathrm{c}}-2t_1)\,, \tag{7.4d}$$

with

$$K_{\mathrm{I}} = \sqrt{1-|r_1|^2}\tau_-, \qquad K_{\mathrm{II}} = r_2 r_1 \tau_+ \tau_-, \tag{7.5}$$
$$K_{\mathrm{III}} = r_2\varrho_+, \qquad K_{\mathrm{IV}} = r_1^2 r_2 \tau_+ \tau_- \varrho_-. \tag{7.6}$$

The operator

$$\mathcal{U}_d = \exp\left[\mathrm{i}(d/2k_{\mathrm{L}})\nabla_\perp^2\right] \tag{7.7}$$

with $\nabla_\perp^2 = \partial_x^2 + \partial_y^2$ accounts for diffraction in the paraxial approximation, corresponding to a propagation distance equal to d (see Appendix F). Here $L_1 = q_0$ and $L_2 = L - q_0$, $t_{1,2} = L_{1,2}/c$, and $t_{\mathrm{c}} = 2(t_1+t_2) = 2L/c$ is the cavity roundtrip time. The factors $e^{\pm 2\mathrm{i}k_{\mathrm{L}}Q(\mathbf{r},t)}$ model the phase front modification produced by the reflection on the membrane in the paraxial approximation.

Before continuing it is going to be useful to express the coefficients $K_{\rm II}$, $K_{\rm III}$ and $K_{\rm IV}$ in terms of the modulus and argument of $K_{\rm II}$ as

$$\begin{aligned} K_{\rm II} &= r\exp\left(\mathrm{i}\theta\right), \quad K_{\rm III} = K_+ r\exp\left(\mathrm{i}\theta\right), \quad K_{\rm IV} = K_- r\exp\left(\mathrm{i}\theta\right) \\ r &= \left|r_1 r_2 \tau_+ \tau_-\right|, \quad \theta = \arg\left(r_1\right) + \arg\left(r_2\right) + \arg\left(\tau_+\right) + \arg\left(\tau_-\right), \\ K_+ &= \frac{\varrho_+}{r_1\tau_+\tau_-}, \quad K_- = r_1\varrho_-. \end{aligned}$$

Note that $r = \left|r_1 r_2\right|\tau^2 = \left|r_1 r_2\right| + O\left(\varrho^2\right)$; if we express $\left|r_{1,2}\right| = \sqrt{1-T_{1,2}}$, with $T_{1,2}$ the transmission factor of mirror 1(2), then

$$r = 1 - \frac{1}{2}\left(T_1 + T_2\right) + O\left(\varrho^2\right), \tag{7.8}$$

if $T_i = O\left(\varrho\right)$, which we assume. Now note that $\arg\left(K_+\right) + \arg\left(K_+\right) = \arg\left(\varrho_+\right) + \arg\left(\varrho_-\right) - \arg\left(\tau_+\right) - \arg\left(\tau_-\right) = \pi$, see (7.1). Further, as only terms up to order ϱ will be considered in order to be consistent with (7.3),

$$K_+ = -\varrho\exp\left(-\mathrm{i}\beta\right), \quad K_- = \varrho\exp\left(\mathrm{i}\beta\right),$$

where $\beta = \arg\left(K_-\right)$.

We will denote the slowly varying complex amplitude of $E_+\left(L,\mathbf{r},t\right)$ as $A\left(\mathbf{r},t\right)$:

$$E_+\left(L,\mathbf{r},t\right) = \mathrm{i}\mathcal{V}A\left(\mathbf{r},t\right)e^{\mathrm{i}k_{\rm L}L - \mathrm{i}\omega_{\rm L}t}. \tag{7.9}$$

When the partial waves expressions (7.4) are introduced into (7.3) and all the fields are expressed in terms of the complex amplitude A we get, shifting time for convenience as $t \to t + t_{\rm c}$,

$$\begin{aligned} A\left(\mathbf{r},t+t_{\rm c}\right) - A\left(\mathbf{r},t\right) = \\ &\sqrt{1-\left|r_1\right|^2}\tau_-\mathcal{U}_L A_{\rm inj}\left(0,\mathbf{r},t+t_c/2\right) + \left(re^{\mathrm{i}\Psi}\mathcal{U}_{2L} - 1\right)A\left(\mathbf{r},t\right) \\ &- \varrho e^{\mathrm{i}\Psi} r\mathcal{U}_{L_2} e^{-2\mathrm{i}k_{\rm L}\left[\tilde{q}_0 + Q\left(\mathbf{r},t+t_{\rm c}-t_2\right)\right]}\mathcal{U}_{L_2}A\left(\mathbf{r},t+2t_1\right) \\ &+ \varrho e^{\mathrm{i}\Psi} r\mathcal{U}_{L+L_1} e^{2\mathrm{i}k_{\rm L}\left[\tilde{q}_0 + Q\left(\mathbf{r},t+t_2\right)\right]}\mathcal{U}_{L+L_1}A\left(\mathbf{r},t-2t_1\right), \end{aligned} \tag{7.9}$$

where we subtracted $A\left(\mathbf{r},t\right)$ from both sides for convenience, and we defined

$$\Psi = 2k_{\rm L}L + \theta, \quad \tilde{q}_0 = q_0 + \beta/2k_{\rm L}. \tag{7.10}$$

Note that the left hand side of Eq. (7.9) can be approimated by $t_{\rm c}\partial_t A\left(\mathbf{r},t\right)$, whenever its right hand side is small; more rigorously if it is of the form

$\mathcal{L}A(\mathbf{r},t)$, with $\mathcal{L}$ a small operator. Inspection of the equation shows that this happens in the physically relevant limit $\left(e^{\mathrm{i}\Psi}R\mathcal{U}_{2L}-1\right)=O(\varrho)$ and $\varrho\to 0$. Note that the first condition requires (i) $r=1-T/2$, with $T=O(\varrho)$, as we already assumed ($T=T_1+T_2$), (ii) $\Psi=2m\pi+\delta$, with δ an $O(\varrho)$ normalized detuning [its value is controled by the injection frequency; see (7.10)], and (iii) $\mathcal{U}_{2L}$ can be approximated as $1+\mathrm{i}(L/k_\mathrm{L})\nabla_\perp^2$, with the effect of the last term on the order of ϱ, which is effected by the choice of a sufficiently small value of L (small diffraction). Under these conditions, $e^{\mathrm{i}\Psi}$, r, $\mathcal{U}_{L_2}$, and $\mathcal{U}_{L+L_1}$ in the last two terms can be approximated by 1 (note that these terms already contain ϱ as a factor), as well as $A(\mathbf{r},t\pm 2t_1)$ can be set to $A(\mathbf{r},t)$ (note that $A(\mathbf{r},t\pm 2t_1)\simeq A(\mathbf{r},t)\pm 2t_1\partial_t A(\mathbf{r},t)$, but $2t_1\partial_t A(\mathbf{r},t)\leq t_\mathrm{c}\partial_t A(\mathbf{r},t)\sim\varrho$). Accordingly Eq. (7.9) can be approximated as

$$\begin{aligned}t_\mathrm{c}\partial_t A(\mathbf{r},t)=&A_0(\mathbf{r},t)-\frac{T}{2}A+\mathrm{i}\left(\delta+\frac{L}{k_\mathrm{L}}\nabla_\perp^2\right)A\\&+\varrho\left[e^{2\mathrm{i}k_\mathrm{L}[\tilde{q}_0+Q(\mathbf{r},t+t_2)]}-e^{-2\mathrm{i}k_\mathrm{L}[\tilde{q}_0+Q(\mathbf{r},t+t_\mathrm{c}-t_2)]}\right]A,\end{aligned}\tag{7.10}$$

where

$$A_0(\mathbf{r},t)=\tau_-\sqrt{T_1}\mathcal{U}_L A_\mathrm{inj}(0,\mathbf{r},t+t_\mathrm{c}/2)\tag{7.11}$$

is the injected field at the plane of the right mirror. Note that $A_0(\mathbf{r},t)\approx\sqrt{T_1}e^{i\arg(\tau_-)}A_\mathrm{inj}(0,\mathbf{r},t+t_\mathrm{c}/2)$. There remains making a last simplification, consisting in approximating $Q(\mathbf{r},t+t_\mathrm{c}\pm t_2)$ by $Q(\mathbf{r},t)$. Note that

$$Q(\mathbf{r},t+t_\mathrm{c}-t_2)\approx Q(\mathbf{r},t)+(t_c-t_2)\,\partial_t Q(\mathbf{r},t),\tag{7.12a}$$

$$Q(\mathbf{r},t+t_2)\approx Q(\mathbf{r},t)+t_2\partial_t Q(\mathbf{r},t),\tag{7.12b}$$

and the last term turns out to be on the order of ϱ or smaller. Hence, we get finally

$$\begin{aligned}\partial_t A(\mathbf{r},t)=&t_\mathrm{c}^{-1}A_0(\mathbf{r},t)-\gamma_\mathrm{c}A+\mathrm{i}\left(\frac{\delta}{t_\mathrm{c}}+\frac{L}{k_\mathrm{L}t_\mathrm{c}}\nabla_\perp^2\right)A\\&+\mathrm{i}\frac{2\varrho}{t_\mathrm{c}}\sin\left[2k_\mathrm{L}(\tilde{q}_0+Q)\right]A.\end{aligned}\tag{7.12}$$

where we introduced the cavity loss rate $\gamma_\mathrm{c}=T/2t_\mathrm{c}$.

Equation (7.12) describes the dynamics of the field amplitude A classically. If we want to treat the field quantum mechanically, (i) we just

substitute A and Q by two quantum fields, call them $\hat{A}$ and $\hat{Q}$, obeying standard equal-time commutation relations

$$\left[\hat{A}\left(\mathbf{r},t\right),\hat{A}^{\dagger}\left(\mathbf{r}',t\right)\right]=\delta^{2}\left(\mathbf{r}-\mathbf{r}'\right) \tag{7.13}$$

[157, 158] and

$$\left[\hat{Q}\left(\mathbf{r},t\right),\hat{P}\left(\mathbf{r}',t\right)\right]=\mathrm{i}\hbar\delta^{2}\left(\mathbf{r}-\mathbf{r}'\right), \tag{7.14}$$

with $\hat{P}=\sigma\partial_{t}\hat{Q}$ the momentum density field of the membrane (σ is the mass surface density of the membrane), and (ii) add a quantum noise term $+\sqrt{2\gamma_{\mathrm{c}}}A_{\mathrm{in}}\left(\mathbf{r},t\right)$ verifying

$$\left[\hat{A}_{\mathrm{in}}\left(\mathbf{r},t\right),\hat{A}_{\mathrm{in}}^{\dagger}\left(\mathbf{r}',t'\right)\right]=\delta^{2}\left(\mathbf{r}-\mathbf{r}'\right)\delta\left(t-t'\right) \tag{7.15}$$

Two independent noise terms should be added, according to the existence of two partially transmitting mirrors (double-sided cavity [18]), in the form $\sqrt{2\gamma_{\mathrm{c},1}}A_{\mathrm{in},1}\left(\mathbf{r},t\right)+\sqrt{2\gamma_{\mathrm{c},2}}A_{\mathrm{in},2}\left(\mathbf{r},t\right)$, with $\gamma_{\mathrm{c},i}=T_{i}/2t_{\mathrm{c}}$ ($\gamma_{\mathrm{c},1}+\gamma_{\mathrm{c},2}=\gamma_{\mathrm{c}}$); however if one of the mirrors has a transmissivity much larger than the other (here mirror 2 for convenience as it is the opposite to the one through which the external field in injected), then $\gamma_{\mathrm{c},2}\approx\gamma_{\mathrm{c}}$ and the first noise term can be neglected [18]. In this quantum mechanical treatment the operator $t_{\mathrm{c}}^{-1}\hat{A}^{\dagger}\left(\mathbf{r},t\right)\hat{A}\left(\mathbf{r},t\right)$ corresponds to the photon flux (number of photons per unit area per unit time) impinging the right cavity mirror.

Although we will not study here this quantum version of Eq. (7.12), we can use it to derive in a straightforward manner the evolution equation for the deformation field Q. For that we note that (the quantum version of) Eq. (7.12) derives from a Hamiltonian $H=H_{\mathrm{light}}+H_{\mathrm{membrane}}+H_{\mathrm{int}}$. The piece

$$H_{\mathrm{light}}=\hbar\int d^{2}r\hat{A}^{\dagger}\left(\mathbf{r},t\right)\left(-\frac{\delta}{t_{\mathrm{c}}}-\frac{L}{k_{\mathrm{L}}t_{\mathrm{c}}}\nabla_{\perp}^{2}\right)\hat{A}\left(\mathbf{r},t\right), \tag{7.16}$$

is the free intracavity light field Hamiltonian [157, 158] in the interaction picture (remind that the optical frequency ω_{L} has been removed from the evolution), where $\delta/t_{\mathrm{c}}=\left(\omega_{\mathrm{L}}-\omega_{\mathrm{c}}\right)$ and ω_{c} is the cavity longitudinal mode frequency closest to the injection frequency ω_{L}. H_{membrane} is the free membrane Hamiltonian (which we describe below). Finally

$$H_{\mathrm{int}}=-\hbar\int d^{2}r\frac{2\varrho}{t_{\mathrm{c}}}\sin\left[2k_{\mathrm{L}}\left(\tilde{q}_{0}+\hat{Q}\left(\mathbf{r},t\right)\right)\right]\hat{A}^{\dagger}\left(\mathbf{r},t\right)\hat{A}\left(\mathbf{r},t\right), \tag{7.17}$$

is the interaction Hamiltonian. From H_{int} we can derive the interaction term in the Heisenberg equation for the membrane's momentum

$$\begin{aligned}\partial_t \hat{P}(\mathbf{r},t)\Big|_{\text{int}} &= \frac{\mathrm{i}}{\hbar}\left[H_{\text{int}}, \hat{P}(\mathbf{r},t)\right] = \\ &= \frac{4\hbar k_{\text{L}}\varrho}{t_{\text{c}}}\cos\left[2k_{\text{L}}\left(\tilde{q}_0 + \hat{Q}(\mathbf{r},t)\right)\right]\hat{A}^{\dagger}(\mathbf{r},t)\,\hat{A}(\mathbf{r},t)\,, \end{aligned} \tag{7.17}$$

where the result follows from

$$\left[F\left(\hat{Q}(\mathbf{r}',t')\right), \hat{P}(\mathbf{r},t)\right] = \mathrm{i}\hbar\left(\partial F/\partial\hat{Q}\right)\delta^2(\mathbf{r}-\mathbf{r}')\,, \tag{7.18}$$

for any function F.

We choose the Hamiltonian for the membrane as

$$H_{\text{membrane}} = \int d^2r\left(\frac{P^2}{2\sigma} + \frac{\sigma v^2}{2}\left((\partial_x Q)^2 + (\partial_y Q)^2\right) + \frac{\sigma\Omega_m^2}{2}Q^2\right) \tag{7.19}$$

which models a membrane that can oscillate as a whole (homogeneous mode) at a frequency Ω_{m} and its characterized by its sound speed v and mass surface density σ. As we show in the experimental implementations chapter, the existence of such homogeneous mode turns out to be essential for pattern formation.

The momentum equation reads:

$$\begin{aligned}\partial_t \hat{P}(\mathbf{r},t) = &-\gamma_{\text{m}}\hat{P} + \sigma v^2\nabla_{\perp}^2\hat{Q} - \sigma\Omega_{\text{m}}^2\hat{Q} \\ &+ \frac{4\hbar k_{\text{L}}\varrho}{t_{\text{c}}}\cos\left[2k_{\text{L}}\left(\tilde{q}_0 + \hat{Q}(\mathbf{r},t)\right)\right]\hat{A}^{\dagger}(\mathbf{r},t)\,\hat{A}(\mathbf{r},t) + \xi(t)\end{aligned} \tag{7.19}$$

where the noise, $\xi(t)$, is an stochastic noise which account for the action of the thermal environment on to the membrane and satisfies the following statistical properties.

$$\langle\xi(t)\rangle = 0, \tag{7.20a}$$

$$\langle\xi(t)\xi(t')\rangle = (2n+1)\delta(t-t') + \frac{i\gamma_{\text{c}}}{\Omega}\delta'(t-t') \tag{7.20b}$$

Now we finally derive the classical expression for the displacement dynamics by identifying $\langle\hat{P}\rangle$ with classical P, $\langle\hat{Q}\rangle$ with classical Q, and $\langle\hat{A}\rangle$ with classical A. The final equation for themembrane can be written as (remember that $P = \sigma\partial_t Q$)

$$\partial_t^2 Q + \gamma_{\text{m}}\partial_t Q + \left(\Omega_{\text{m}}^2 - v^2\nabla_{\perp}^2\right)Q = \frac{4\varrho\hbar k_{\text{L}}}{\sigma t_{\text{c}}}\cos\left[2k_{\text{L}}\left(\tilde{q}_0 + \hat{Q}\right)\right]|A|^2\,. \tag{7.21}$$

As the membrane deformations Q are very small with respect to the optical wavelength, the trigonometric functions in the interaction terms can be written as

$$\sin\left[2k_{\mathrm{L}}\left(\tilde{q}_0+Q\right)\right]\approx\sin\left(2k_{\mathrm{L}}\tilde{q}_0\right)\left(1-2k_{\mathrm{L}}^2Q^2\right)+\cos\left(2k_{\mathrm{L}}\tilde{q}_0\right)2k_{\mathrm{L}}Q, \quad (7.22a)$$

$$\cos\left[2k_{\mathrm{L}}\left(\tilde{q}_0+\hat{Q}\right)\right]\approx\cos\left(2k_{\mathrm{L}}\tilde{q}_0\right)\left(1-2k_{\mathrm{L}}^2Q^2\right)-\sin\left(2k_{\mathrm{L}}\tilde{q}_0\right)2k_{\mathrm{L}}Q \quad (7.22b)$$

i.e., the coupling contains in general linear and quadratic terms in Q. Now, two important cases: (i) $\cos\left(2k_{\mathrm{L}}\tilde{q}_0\right)=\pm1$, and (ii) $\sin\left(2k_{\mathrm{L}}\tilde{q}_0\right)=\pm1$. In case (i)

$$\sin\left[2k_{\mathrm{L}}\left(\tilde{q}_0+Q\right)\right] \approx \pm2k_{\mathrm{L}}Q, \quad (7.23)$$

$$\cos\left[2k_{\mathrm{L}}\left(\tilde{q}_0+\hat{Q}\right)\right] \approx \pm\left(1-2k_{\mathrm{L}}^2Q^2\right)\approx\pm1, \quad (7.24)$$

(the linear coupling case). In case (ii)

$$\sin\left[2k_{\mathrm{L}}\left(\tilde{q}_0+Q\right)\right] \approx \pm\left(1-2k_{\mathrm{L}}^2Q^2\right), \quad (7.25)$$

$$\cos\left[2k_{\mathrm{L}}\left(\tilde{q}_0+\hat{Q}\right)\right] \approx \mp2k_{\mathrm{L}}Q, \quad (7.26)$$

(quadratic coupling). Note that in case (i) we neglect the quadratic term in (7.24) because it is a very small correction to the interaction term in Eq. (7.21). On the contrary in case (ii) the quadratic term in (7.25) must be retained as the first term (±1) just redefines the detuning δ and only the quadratic term couples the evolution of A to Q. Summarizing, the two limit cases we will analyze here read

Linear coupling case

$$\partial_tA\left(\mathbf{r},t\right)=t_{\mathrm{c}}^{-1}A_0\left(\mathbf{r},t\right)-\gamma_{\mathrm{c}}A+\mathrm{i}\left(\frac{\delta}{t_{\mathrm{c}}}+\frac{L}{k_{\mathrm{L}}t_{\mathrm{c}}}\nabla_\perp^2\right)A\pm\mathrm{i}\frac{4\varrho k_{\mathrm{L}}}{t_{\mathrm{c}}}QA, \quad (7.27)$$

$$\partial_t^2Q+\gamma_{\mathrm{m}}\partial_tQ+\left(\Omega_{\mathrm{m}}^2-v^2\nabla_\perp^2\right)Q=\pm\frac{4\varrho\hbar k_{\mathrm{L}}}{\sigma t_{\mathrm{c}}}\left|A\right|^2, \quad (7.28)$$

and

Quadratic coupling case

$$\partial_tA\left(\mathbf{r},t\right)=t_{\mathrm{c}}^{-1}A_0\left(\mathbf{r},t\right)-\gamma_{\mathrm{c}}A+\mathrm{i}\left(\frac{\delta_{\mathrm{eff}}}{t_{\mathrm{c}}}+\frac{L}{k_{\mathrm{L}}t_{\mathrm{c}}}\nabla_\perp^2\right)A\mp\mathrm{i}\frac{4\varrho k_{\mathrm{L}}^2}{t_{\mathrm{c}}}Q^2A, \quad (7.29)$$

$$\partial_t^2Q+\gamma_{\mathrm{m}}\partial_tQ+\left(\Omega_{\mathrm{m}}^2-v^2\nabla_\perp^2\right)Q=\mp\frac{8\varrho\hbar k_{\mathrm{L}}^2}{\sigma t_{\mathrm{c}}}Q\left|A\right|^2, \quad (7.30)$$

where $\delta_{\mathrm{eff}}=\delta\pm2\varrho/t_{\mathrm{c}}$ is an effective detuning.

7.3.1 Normalization

Before continuing, and in order to give a cleaner presentation, we introduce normalized and dimensionless time $\tau = \gamma_c t$ and spatial coordinates $r_i' = r_i/l_c$, where $(r_1, r_2) = (x, y)$ and the parameters

$$l_c = \frac{L}{k_L t_c \gamma_c}, \quad \Delta = \frac{\delta_{(\text{eff})}}{t_c \gamma_c}, \quad \Omega_0 = \frac{\Omega_m}{\gamma_c}, \quad \rho = \frac{v}{\Omega_m} \tag{7.31}$$

For the linear coupling case, we define the normalized variables,

$$Z = \frac{4\varrho k_L}{t_c \gamma_c} Q, \quad F = \frac{4\varrho k_L}{t_c \Omega_0}\sqrt{\frac{\hbar}{\gamma_c \sigma}} A, \quad E = \frac{4\varrho k_L}{t_c^2 \gamma_c \Omega_0}\sqrt{\frac{\hbar}{\gamma_c \sigma}} A_0 \tag{7.32}$$

that leave the equations in the next way,

$$\partial_\tau F = \left(-1 + i\Delta + i\nabla^2 \pm iZ\right) F + E, \tag{7.33a}$$

$$\partial_\tau^2 Z + \gamma \partial_\tau Z + \Omega_0^2 \left(1 - \rho^2 \nabla^2\right) Z = \pm \Omega_0^2 \left|F\right|^2, \tag{7.33b}$$

In the quadratic coupling case, the new variables will be

$$Z^2 = \frac{4\varrho k_L^2}{t_c \gamma_c} Q^2, \quad F = \frac{2k_L}{\Omega_0}\sqrt{\frac{\hbar\varrho}{t_c \sigma}} A, \quad E = \frac{2k_L}{\Omega_0 t_c \gamma_c}\sqrt{\frac{\hbar\varrho}{t_c \sigma}} A_0 \tag{7.34}$$

and the equations

$$\partial_\tau F = \left(-1 + i\Delta + i\nabla^2 \mp iZ^2\right) F + E, \tag{7.35a}$$

$$\partial_\tau^2 Z + \gamma \partial_\tau Z + \Omega_0^2 \left(1 - \rho^2 \nabla^2\right) Z = \mp 2\Omega_0^2 Z \left|F\right|^2, \tag{7.35b}$$

8. LINEAR COUPLING

In this section we assume that the intracavity membrane is placed in between a node and an antinode of the intracavity field. Hence, we start from the normalized equations of subsection 7.3.1,

$$\partial_\tau F = \left(-1 + i\Delta + i\nabla^2 \pm iZ\right) F + E, \tag{8.1a}$$

$$\partial_\tau^2 Z + \gamma\partial_\tau Z + \Omega_0^2 \left(1 - \rho^2\nabla^2\right) Z = \pm\Omega_0^2 \left|F\right|^2. \tag{8.1b}$$

It is important to mention that the $\pm$ can be absorbed as a change of sign in the Z, so from now on we will use the $'+'$ equations.

8.1 Homogeneous solutions and stability analysis.

We calculate the homogeneous steady state of these equation by putting all time and space derivatives to zero. We obtain that $\bar{Z} = \left|\bar{F}\right|^2 \doteq \bar{I}$, with

$$E^2 = \left[1 + \left(\Delta + \bar{I}\right)^2\right] \bar{I}, \tag{8.2}$$

(in the following an overbar denotes the homogeneous steady state). This equation predicts single-valued response for $\Delta > -\sqrt{3}$. And three-valued response for $\Delta < -\sqrt{3}$, where the characteristic curve, $\bar{I}$ vs. E, exhibits the well known S-shape, with the turning points located at $\bar{I}_\pm = \left(-2\Delta \pm \sqrt{\Delta^2 - 3}\right)/3$ (Fig. 8.1).

We perform the standard linear stability analysis by adding small plane wave perturbations around the homogeneous steady states ($\bar{F}$,$\bar{Z}$),

$$F = \bar{F} + \delta F e^{i\mathbf{k}\mathbf{r}'} e^{\lambda\tau}, \tag{8.3a}$$

$$F^* = \bar{F}^* + \delta F^* e^{i\mathbf{k}\mathbf{r}'} e^{\lambda\tau}, \tag{8.3b}$$

$$Z = \bar{Z} + \delta Z e^{i\mathbf{k}\mathbf{r}'} e^{\lambda\tau}, \tag{8.3c}$$

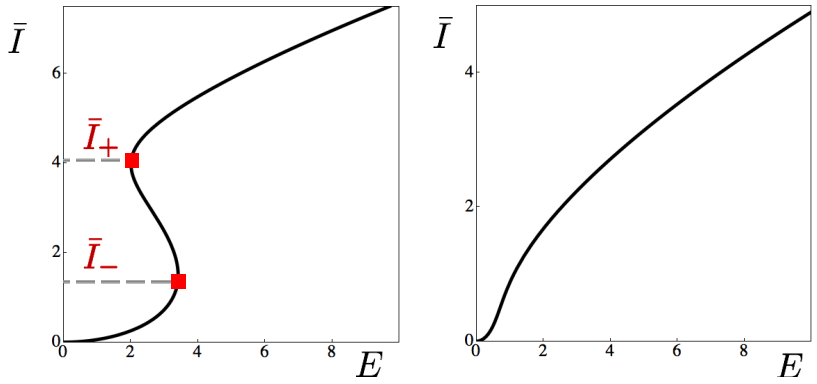

Fig. 8.1: Left, multivalued solution for $\Delta < -\sqrt{3}$. Right, univalued solution for $\Delta > -\sqrt{3}$

Substituting in Eqs. 8.1 we obtain the next equation system for the perturbations:

$$\lambda \delta F = \left(-1 + i\Delta_k + i\bar{Z}\right)\delta F + i\bar{F}\delta Z, \tag{8.4a}$$

$$\lambda\left(\lambda + \gamma\right)\delta Z = -\Omega_0^2\left(1 + \rho^2 k^2\right)\delta Z + \Omega_0^2\left(\bar{F}\delta F^* + \bar{F}^*\delta F\right), \tag{8.4b}$$

where $\Delta_k \equiv \Delta - k^2$. Because of the rotational invariance of the model equations, the stability of the solutions will no longer depend on $\mathbf{k}$ but in its module, k. From these equations, one can obtain a characteristic polynomial on λ ($C\left(k^2;\lambda\right) \equiv \sum_{n=0}^{4} c_n\left(k^2\right)\lambda^n = 0$). After simple algebra, we obtain $c_4 = 1$, $c_3 = 2 + \gamma$, and

$$c_2 = 1 + 2\gamma + \Omega_k^2 + \left(\Delta_k + \bar{I}\right)^2, \tag{8.5a}$$

$$c_1 = \gamma\left[1 + \left(\Delta_k + \bar{I}\right)^2\right] + 2\Omega_k^2, \tag{8.5b}$$

$$c_0 = 2\bar{I}\left(\Delta_k + \bar{I}\right)\Omega_0^2 + \left[1 + \left(\Delta_k + \bar{I}\right)^2\right]\Omega_k^2, \tag{8.5c}$$

where $\Omega_k^2 \equiv \Omega_0^2\left(1 + \rho^2 k^2\right)$. Whenever $\mathrm{Re}\{\lambda\} < 0$ for all k, the perturbation to the solutions will get smaller with time (τ) and the steady state will result stable, while if $\mathrm{Re}\{\lambda\} > 0$ for some k, will be unstable. The condition $\mathrm{Re}\{\lambda\} = 0$, thus, defines a possible instability, or bifurcation, which is met either when $\lambda = 0$ (static instability or Pitchfork bifurcation: $c_0 = 0$) or when $\lambda = \mathrm{i}\sqrt{c_1/c_3}$ (self-pulsing, or Hopf instability: $c_1 c_2 c_3 = c_4 c_1^2 + c_3^2 c_0$)[1].

[1] Also known as Routh-Hurwitz Theorem [146, 159]

On the other hand, when the bifurcation is associated with $k = 0$ the new state is spatially uniform (homogeneous instability), while if $k \neq 0$ the instability is pattern forming. This method allows us to know where are the (local) bifurcations and how the new solution will be in the vicinity of the bifurcation. As we go far beyond the bifurcation points, other instabilities of the new solutions could appear making our predictions no longer valid.

Pitchfork bifurcation. Let us consider first the static instabilities. The solutions of $c_0 = 0$, will be called the pattern forming instability or Pitchfork bifurcation intensity, which reads

$$\bar{I}_{PB} = \frac{-\Delta_k(2 + k^2\rho^2) \pm \sqrt{\Delta_k^2 - 3 - 4k^2\rho^2 - k^4\rho^4]}}{3 + k^2\rho^2} \tag{8.6}$$

This solution, for a fixed $k = 0$ and $\Delta < -\sqrt{3}$, gives the turning points of the S-shape solution ($\bar{I}_{\pm}$). Therefore, we conclude that the middle branch of the S, $\bar{I} \in [\bar{I}_-, \bar{I}_+]$, is always unstable. Allowing k to vary, pattern forming instabilities appear with a strong dependence on ρ.

As this bifurcation only depends on the parameters Δ and ρ, we are going to explain its behaviour on the <Δ,ρ> plane, Fig. 8.2. There are four relevant scenarios or regions, denoted by Roman numbers from (I) to (IV)[2].

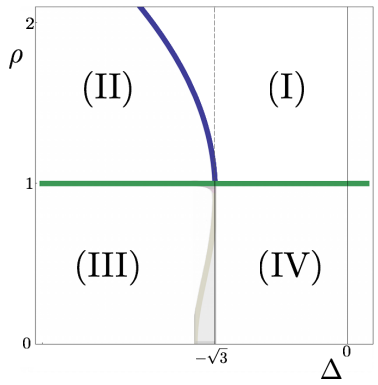

Fig. 8.2: ρ vs Δ map. $\rho = 1$ in green. ρ_1 in blue separating zones (**I**) and (**II**).

In the following, in order to give a full picture of this bifurcation, we are going explain in detail each one of the regions, but first lets say the meaning of the curves of the <Δ,ρ> plane plot, Fig. 8.2.

[2] Note that between regions (III) and (IV) there is a tiny shadowed region. This corresponds to more complicated phenomena displayed further in the text

The blue line, denoted here by

$$\rho_1^2 = 3\frac{2\sqrt{\Delta^2-3}-\Delta}{3+\Delta\left(\Delta+\sqrt{\Delta^2-3}\right)}, \tag{8.7}$$

is the value of ρ, which if lower, the Pitchfork bifurcation intensity, $\bar{I}_{PB}$, will present a local maximum as a function of k for $k \neq 0$. On the other hand, the green line, $\rho = 1$, represent whether or not $\bar{I}_{PB}$ is a real value that tends to infinity when k tends to infinity. So for $\rho \leq 1$, there will always be a pattern forming instability. Finally, as already explained, the black line at $\Delta = -\sqrt{3}$ separates the three valued solution from the uni valued. However, as we see in the following, does not necessarily delimit a region.

We illustrate in Fig. 8.3, the entrance and exit points of the bifurcations for each of the regions. In this plot, for each scenario we find, on the left, the steady solution of the system in a intensity ($\bar{I}$) vs injection amplitude (E) plot, which, if unstable, is showed in a dashed line. Remember that in the steady state $\bar{I} = \bar{Z}$, so any conclusion on the intensity will work on the displacement ($\bar{Z}$) as well. On the right, the condition for the Pitchfork bifurcation, $\bar{I}_{PB}$, is represented in a $\bar{I}$ vs k plot. Thus, the line in this plot separates stable from unstable solutions, and if there is any local maximum or minimum for $k \neq 0$ this instability will present spatial behaviour (patterns).

- Region (I). This region is the only one where there is no Pitchfork bifurcation. It is delimited below by $\rho = 1$, and, on the left, by ρ_1. Part of the region enters in the multivalued solution area ($\Delta < \sqrt{3}$). So here, we can only illustrate that the middle branch of this solution is unstable, Fig. 8.3.

- Region (II). Bounded by ρ_1 on the right and $\rho = 1$ underneath. It is specially interesting because, in the upper branch of the S-shape solution, there is pattern forming instability from $\bar{I}_+$ to $\bar{I}_{PB,+}$, which as coexisting with the stable lower branch, could lead to the formation of localized structures. We can see in Fig. 8.3, that $\bar{I}_{PB,+}$ corresponds to a maximum in the $\bar{I}$ vs k plot. The expression of $\bar{I}_{PB,+}$ is too lengthy to give it here but of its behaviour we can say that the closer is ρ to 1, the larger it is.

- Region (III). This region is delimited by $\rho = 1$ above and the shadowed zone (which will be explained later). In this case the situation is simple,

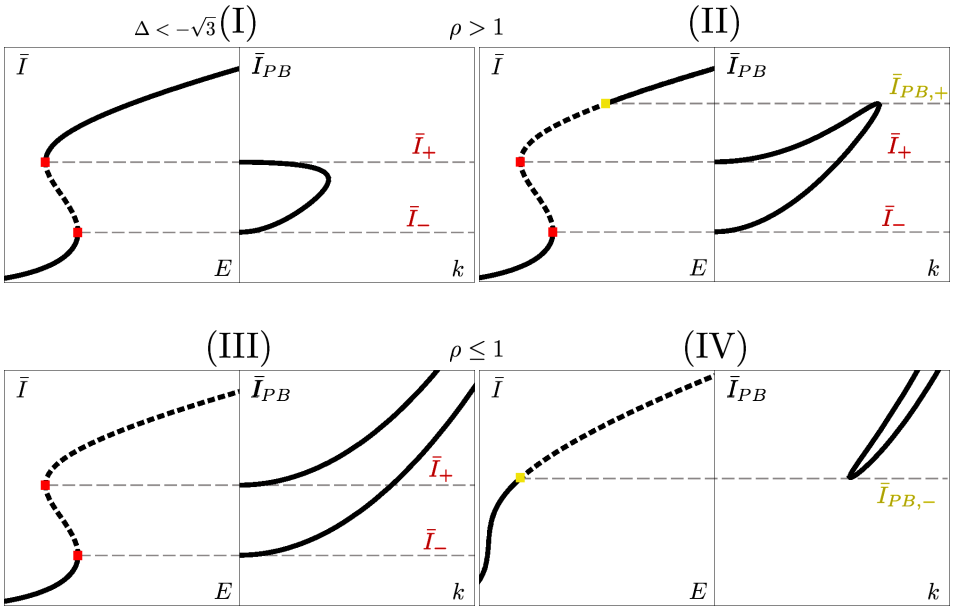

Fig. 8.3: Situation of the Pitchfork bifurcation. (I) There is no Pitchfork bifurcation. (II) There is a Pitchfork bifurcation between $\left[\bar{I}_+, \bar{I}_{PB,+}\right]$. (III) All the upper branch of the three valued solution is unstable. (IV) There is a Pitchfork bifurcation between $\left[\bar{I}_{PB,-}, \infty\right]$

all the upper branch of the three-valued solution is unstable, from the upper returning point $\bar{I}_+$ to ∞ (Fig. 8.3). In all the $\rho < 1$ regions, $\bar{I}_{PB}$ will tend to ∞ as $k \to \infty$.

- Region (IV). Another $\rho < 1$ region delimited also by $\Delta = -\sqrt{3}$. Is the only one where the solution is always univalued. In this case, a minimum of $\bar{I}_{PB}$ vs k arises. This pattern forming instability goes from $\bar{I}_{PB,-}$ to ∞. Also, the expression of $\bar{I}_{PB,-}$ is too lengthy to give it here, but in the same way to $\bar{I}_{PB,+}$, the closer is ρ to 1, the larger it is. For $\rho = 0$ it is constant and equal to 1.

Being mentioned the main scenarios of the Pitchfork bifurcation, we explain now, for completeness, the other regions that appear in the shadowed region between (III) and (IV).

We can find a zoom of the $-2 < \Delta < -\sqrt{3}$ zone in Fig. 8.4. The solution here is always multivalued. Two new situations appear separated

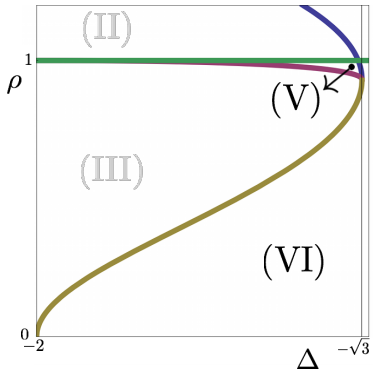

Fig. 8.4: Zoom of the ρ vs Δ map between $\Delta \in \left[-2, -\sqrt{3}\right]$.Two new zones appear (V) and (VI)

by two new curves. The yellow line corresponds to

$$\rho_3^2 = \frac{\sqrt{\Delta^2 - 3} - 2\Delta}{1 + \Delta^2}, \tag{8.8}$$

and indicates that a minimum for $\bar{I}_{PB}$ appears for some $k \neq 0$. The magenta line defined by

$$\rho_2^2 = 3\frac{2\sqrt{\Delta^2 - 3} + \Delta}{3 - \Delta\left(\Delta - \sqrt{\Delta^2 - 3}\right)}, \tag{8.9}$$

will be more comprehensive knowing about the description of region (IV), so we leave it for later. Al the curves, $\rho_{1,2,3}$, match at $\sqrt{3}/2$ because they separate regions which behaviour agree at this point.

- Region (V). This is the region where almost everything happens. Displayed in Fig. 8.5, the instability goes from $\bar{I}\epsilon\left[\bar{I}_+, \bar{I}_{PB,+}(\text{local})\right] \cup \left[\bar{I}_{PB,-}(\text{local}), \infty\right]$. Notice that $\bar{I}_{PB,-}$ is larger than $\bar{I}_{PB,+}$, but they touch each other at $\rho = \rho_2$, which is the curve where the local minimum of $\bar{I}_{PB}$ coincide with the local maximum.

- Region (VI). Delimited by ρ_3 and $\Delta = -\sqrt{3}$. As illustrated in Fig. 8.5, in region (V) a small portion of the lower branch of the S-shape solution can be unstable with a pattern forming instability.

Hopf bifurcation. Coming back to the main scenarios (I) to (IV), next we study the behaviour of the self-pulsing or Hopf bifurcation. As the

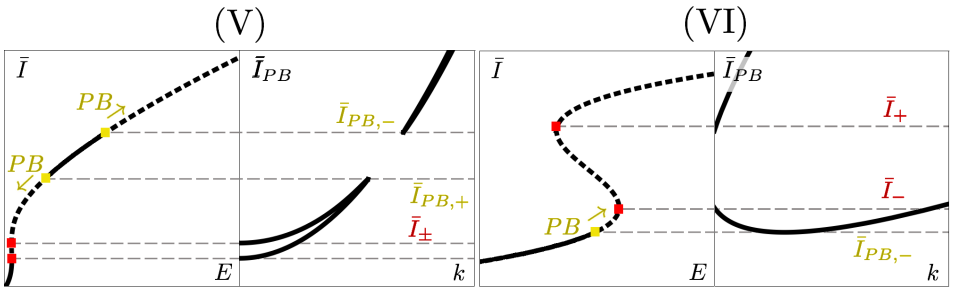

Fig. 8.5: Situation of the Pitchfork when $\Delta\epsilon\left[-2,-\sqrt{3}\right]$. (V) A small portion of the lower branch of the bistability is unstable in $\left[\bar{I}_{PB,-},\bar{I}_{-}\right]$. All the upper branch is unstable. (VI) Zones (II) and (IV) coexist, unstable between $\left[\bar{I}_{+},\bar{I}_{PB,+}(\text{local})\right]\cup\left[\bar{I}_{PB,-}(\text{local}),\infty\right]$

expression is lengthy and difficult to manage we are going to study it at the physical limit, $\gamma \ll \Omega_0$ (the mechanical oscillations are of high-Q) and $\gamma \ll 1$ (the damping rate of the mirror oscillations is much smaller than the cavity damping rate). In this limit, the unstable self pulsing part will cover the range $\bar{I}_{\text{HB},-}$ to ∞. Depending on Δ this bifurcation can be homogeneous for $\Delta < \Delta_{HB}$ or self pulsing patterns for $\Delta > \Delta_{HB}$. Under the related approximations, Δ_{HB} its always positive. In Fig. 8.6 we have, in gray, the

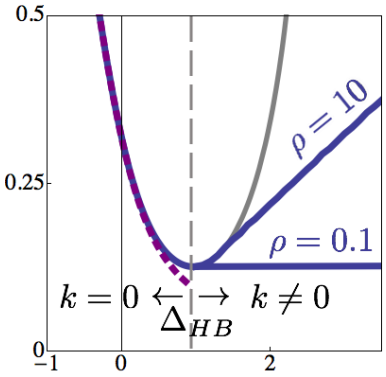

Fig. 8.6: In grey, the condition for the Hopf for $k = 0$. In blue the entering point of the Hopf bifurcation. In order to see the dependence of the $k \neq 0$ part with ρ, two cases are plotted, $\rho = 0.1$ and $\rho = 10$. In dashed magenta, our approximation. $\Omega = 1$, $\gamma = 0.1$, $\rho = 1.13$

condition for the Hopf bifurcation with $k = 0$, and in blue the entering

point of the bifurcation, $\bar{I}_{\mathrm{HB},-}$. Be aware that in the $k \neq 0$ part there is a strong dependence on ρ (the larger the steeper is this curve). When the Hopf is homogeneous ($\Delta < \Delta_{HB}$), the entering point of the bifurcation can be approximated by (magenta dashed line)

$$2\bar{I}_{\mathrm{HB},-} = \sqrt{\Delta^2 + \gamma\left(1+\Omega_0^2\right)^2/\Omega_0^2} - \Delta. \tag{8.10}$$

This solution, independent of ρ, is always growing with γ and with Ω (when $\Omega > 1$). When the solution is multivalued ($\Delta < -\sqrt{3}$), it is always larger than the upper returning point $\bar{I}_+$, and tends to it when $\Delta \to \infty$. So, for large negative detunnings, almost all the upper branch will have self pulsing solutions.

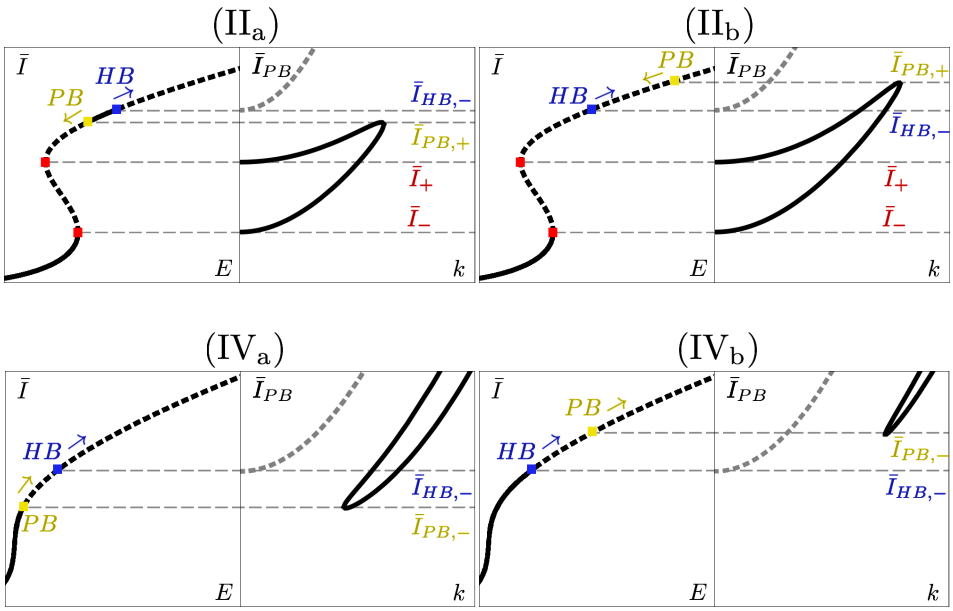

Fig. 8.7: Location of the Hopf in relation with the Pitchfork. The case (II$_a$), is the only one where the Hopf and the Pitchfork don't share a region. In (II$_b$) all the upper branch is unstable and The Pitchfork and the Hopf are crossed and act in opposite direction. In region (IV) where there is no bistability we have again to scenarios. In (IV$_a$) both bifurcations act in the same direction and the Hopf is higher than the Pitchfork. Finally in (IV$_b$) both bifurcations act in the same direction and the Pitchfork is above the Hopf. In this case there are two possibilities: for $\Delta < \Delta_{HB}$ where $I_{HB,-}$ is at $k = 0$ and for $\Delta > \Delta_{HB}$ where $I_{HB,-}$ is at $k \neq 0$.

Now we shall think where the Hopf is located in relation with the Pitchfork. This question makes sense when there is a entering (or exiting) point of the Pitchfork bifurcation. Taking this into account, the regions (II) and (IV) will have two different behaviours, labelled with letters a or b, which will correspond to the cases where the Hopf is above or below the Pitchfork bifurcation respectively, Fig. 8.7.

It is important to mention that all the $\Delta \geq \Delta_{HB}$ part is included as a special case of ($\mathrm{IV_b}$) because the Hopf for $k \neq 0$ is always below the beginning of the Pitchfork. Note that, as we already explained, the self pulsing instability always acts in the same direction, from $\bar{I}_{\mathrm{HB},-}$ to ∞.

Again, for completeness, if we consider the shadowed zone between $-2 < \Delta < -\sqrt{3}$ including the self-pulsing or Hopf bifurcation, under the same approximations as before (Eq. 8.10), we find three more scenarios illustrated in Fig. 8.8 where the Hopf can be in three places, below $\bar{I}_{PB,+}$ ($\mathrm{V_b}$), between this and $\bar{I}_{PB,-}$ ($\mathrm{V_a}$) or above everything ($\mathrm{V_c}$). However, in region (V), the Pitchfork will always be lower than the Hopf, which as we know, it is always above the upper returning point of the S-Shape solution.

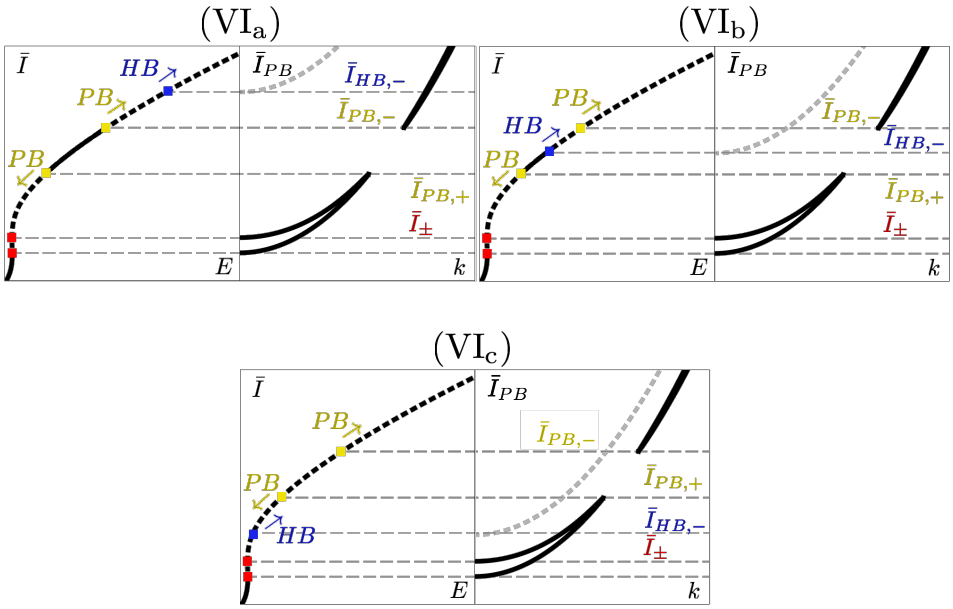

Fig. 8.8: Location of the Hopf in relation with the Pitchfork: below $\bar{I}_{PB,+}$ ($\mathrm{VI_b}$), between this and $\bar{I}_{PB,-}$ ($\mathrm{VI_a}$) or above everything ($\mathrm{VI_c}$).

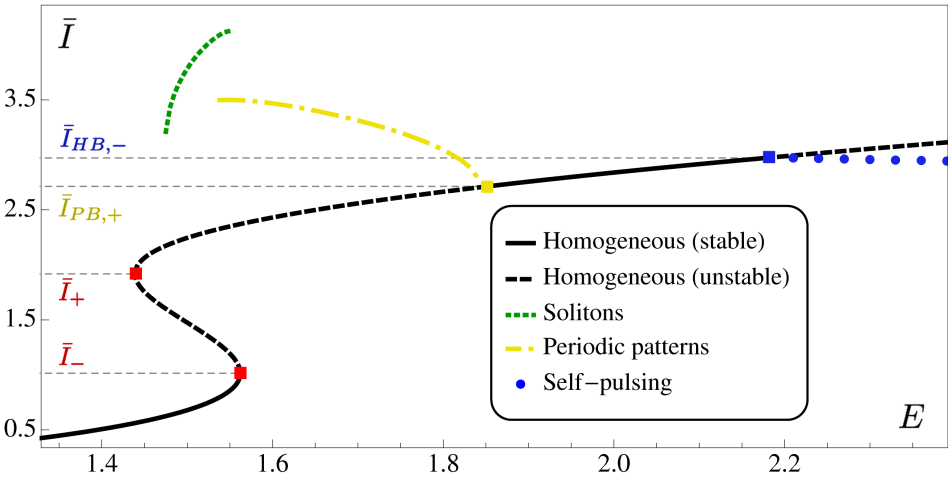

Fig. 8.9: Simulation for region ($\mathrm{II_a}$). Parameters: $\Delta = -2.2$, $\rho = 1.13$, $\Omega = 10$, $\gamma = 0.1$. Evolution with the injection of the peaks of the static pattern forming instabilities: periodic patterns (in dashed-dotted yellow), solitons (in dotted green) and the mean in time of the self-pulsing solutions (in blue filled circles)

8.2 Numerical simulation

We perform a numerical simulation using the split-step method [160], explained in detail in Appendix H. Firstly, as they are intrinsic to the method, we are going to solve the problem with periodic boundary conditions. Later, we will show some examples with fixed boundaries and illumination with finite transverse extension.

All the simulations are started with a small amount of noise around 0 for all the variables. We have checked that all the analytical predictions from the linear stability analysis can be reproduced. We find patterns within all the regions of the parameter space delimited by pattern forming instabilities: regions Fig: 8.2 (II,III,IV) and, when they coexist with a static homogeneous solution (bistability), we find solitons, regions (II,III).

The cavity solitons can be excited by using an injected field with a transverse Gaussian profile, with the appropriate height and width, in the injection amplitude during a short period of time at the beginning of the simulation. After that, if we continue with plane illumination the soliton will still be a stable solution of the system. If the transversal extension is large enough, it is possible to plug several solitons in any position wanted. Any

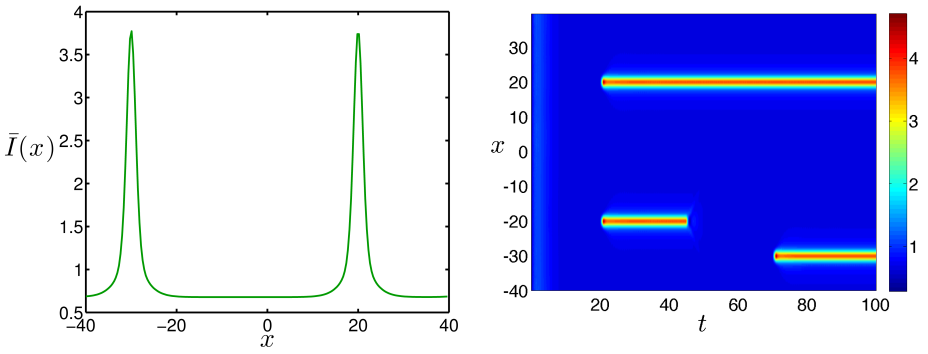

Fig. 8.10: Solitons in ($\mathrm{II_a}$). Parameters: $\Delta = -2.2$, $\rho = 1.13$, $\Omega = 10$, $\gamma = 0.1$ and injection amplitude of $E = 1.5$. The chosen time step is $h = 0.01$. On the right, position (x) versus time (t) contour plot, where the color code represents the intracavity intensity ($\bar{I}(x)$). The simulation is started with a small amount of noise around 0 in the variables and a flat profile in the injection. At $t = 20$ two solitons are turned on including for 100 steps two appropriate gaussians at $x = \pm 20$ in the injection amplitude. Then we turn off the soliton at $x = -20$ and after a while turn another one at $x = -30$ obtaining what we have on the left side.

chosen soliton can be turned off through a Gaussian profile with negative amplitude in the injection amplitude centered at the position of the selected soliton, again, for a short period of time. In order to see these features and others we choose to show in detail the case ($\mathrm{II_a}$), where all the instabilities are present and differenced. As we can see in Fig. 8.9, we have a bistability between a homogenous solution and a pattern forming instability, which goes from $\bar{I}_{PB,+}$ to $\bar{I}_{+}$. On the other hand, a homogeneous self pulsing instability occupies form $\bar{I}_{HB,-}$ to ∞. In the figure, the information of the numerical calculation is coded in the next way: in dashed-dotted yellow, the peaks of the periodic patterns, in dotted green, the peak of the soliton (or solitons), and in blue filled circles, the mean value around which oscillate the self-pulsing solutions.

An example of the solitons is showed in Fig. 8.10. On the right, we can see the time evolution of the intracavity intensity $\bar{I}(x)$ in a position x versus time t contour plot, where t is the number of steps (n_t) times the size of the step (h). The simulation is started with a small amount of noise around 0 in the variables and a plane profile in the injection. At $t = 20$ two solitons are turned on including just for 100 steps two appropriate Gaussians at

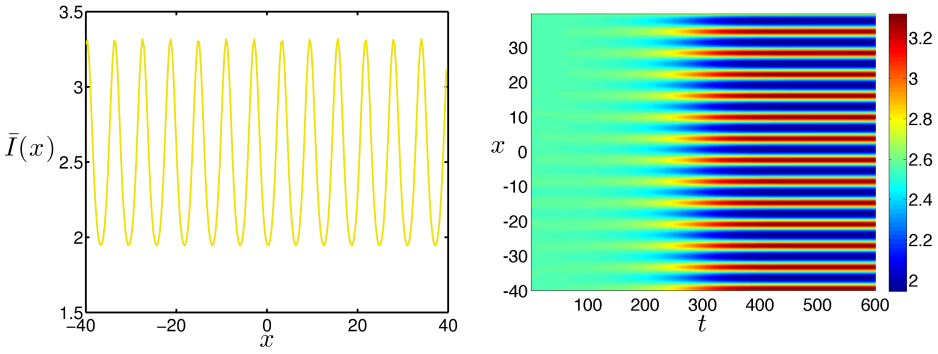

Fig. 8.11: Patterns in ($\mathrm{II_a}$). Parameters: $\Delta = -2.2$, $\rho = 1.13$, $\Omega = 10$, $\gamma = 0.1$ and injection amplitude of $E = 1.7$. Full time simulation.

$x = \pm 20$ in the amplitude injection. Then we go back to plane illumination and, as expected, the solitons still exist. Also, in order to illustrate the erasing of solitons, we turn off the soliton at $x = -20$ and, after a while, turn on another one at $x = -30$ obtaining what we have on the left side in Fig. 8.10.

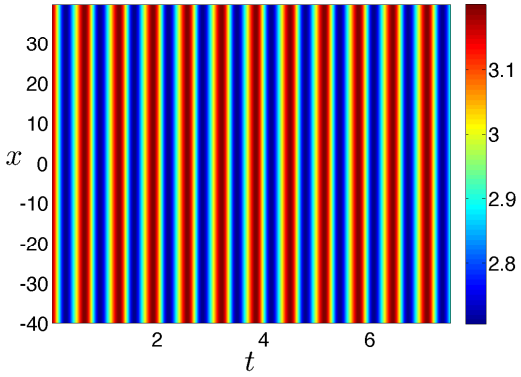

Fig. 8.12: Homogeneous Hopf in region ($\mathrm{II_a}$). Parameters: $\Delta = -2.2$, $\rho = 1.13$, $\Omega = 10$, $\gamma = 0.1$ and injection amplitude of $E = 2.3$. Only represented the last 750 steps of the simulation

An example of periodic patterns is shown in Fig. 8.11. On the left the final result of the time evolution represented on the right side. In this case,

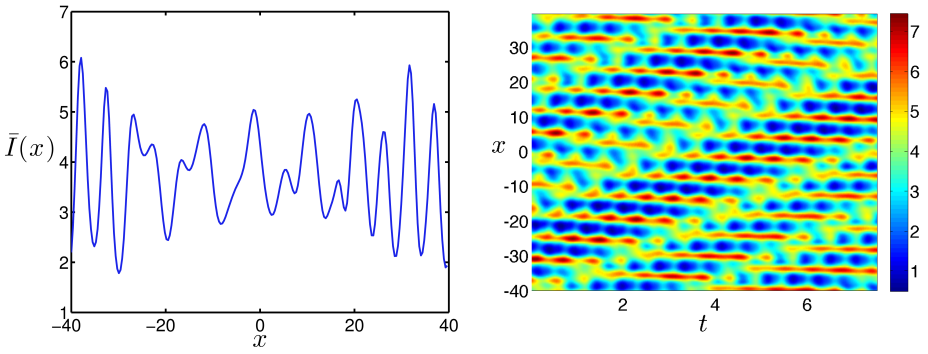

Fig. 8.13: Deep inside the Hopf in region ($\mathrm{II_a}$). Parameters: $\Delta = -2.2$, $\rho = 1.13$, $\Omega = 10$, $\gamma = 0.1$ and injection amplitude of $E = 15$. Only represented the last 750 steps of the simulation

the simulation has been started with plane illumination at $E = 1.7$ and small amount of noise for the variables. We arrive to static patterns at a time approximately 20 times larger than to reach solitons.

The homogeneous self pulsing instability from $\bar{I}_{HB,-}$ is also reached at large times and it behaves as a flat line oscillating in time represented in Fig. 8.12. When we go deep inside any Hopf bifurcations our predictions about the spatial behaviour are no longer valid and we find no homogeneous nor periodic solutions as Fig. 8.13.

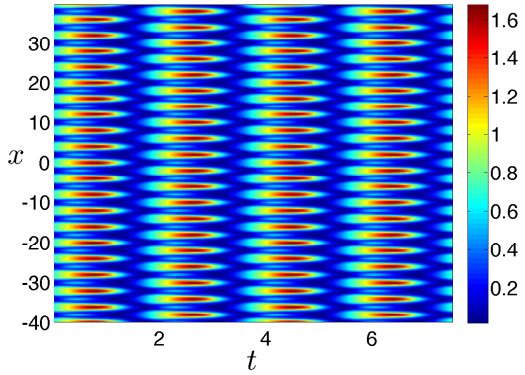

Fig. 8.14: Simulation for region ($\mathrm{IV_b}$). Parameters: $\Delta = 4 > \Delta_{HB}$, $\rho = 0.85$, $\Omega = 1$, $\gamma = 0.1$ and injection amplitude of $E = 2.2$. Only represented the last 750 steps of the simulation

As we have seen in previous chapter, all but one of the cases for Hopf bifurcations are homogeneous. There is only one case for self-pulsing patterns: ($\mathrm{IV_b}$) with $\Delta > \Delta_{HB}$ shown in Fig. 8.14.

All the rest of regions analysed in the stability analysis above, have equivalent features to those that have been explained in this section, so we won't go on detail on them.

When two solitons are close enough, they are attracted one to each other becoming only one (Fig. 8.15). To bring them together we include a small gradient in the injection amplitude whose maximum is at $x = 0$.

All that has been related also occur for finite illumination along the transverse dimension, which is simulated by including a supergaussian in the injection amplitude below any other profile. With this consideration, all the features of the system can be replicated. In Fig. 8.16 there are examples of the static structures (a soliton injected at $x = 10$ on the left side and periodic patterns on the right side). Also in Fig. 8.17, we have an example of the homogeneous Hopf for finite illumination. This illumination as is intrinsically inhomogeneous because of the walls of the supergaussian, just far from them we can recover the homogeneous case.

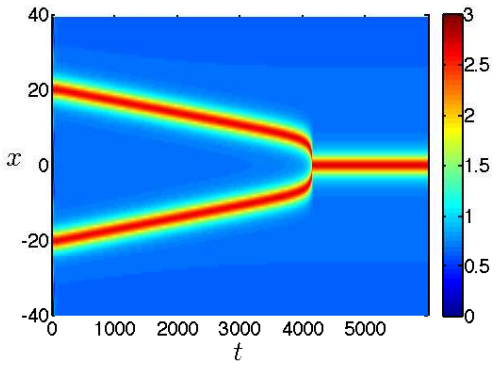

Fig. 8.15: Clash of solitons. Parameters: $E = 1.5$, $\Delta = -2.2$, $\rho = 1.13$, $\Omega = 10$, $\gamma = 0.1$. we include an small gradient in the injection amplitude whose maximum is at $x = 0$. As the solitons are attracted to bigger intensities they get closer until they are combined in one.

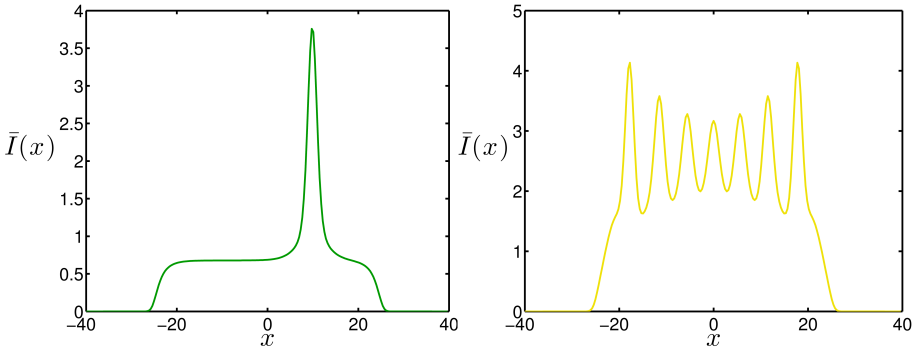

Fig. 8.16: Simulation for region ($\mathrm{II_a}$) with finite illumination. Parameters: $\Delta = -2.2$, $\rho = 1.13$, $\Omega = 10$, $\gamma = 0.1$ and injection amplitude of $E = 1.5$ and 1.7.

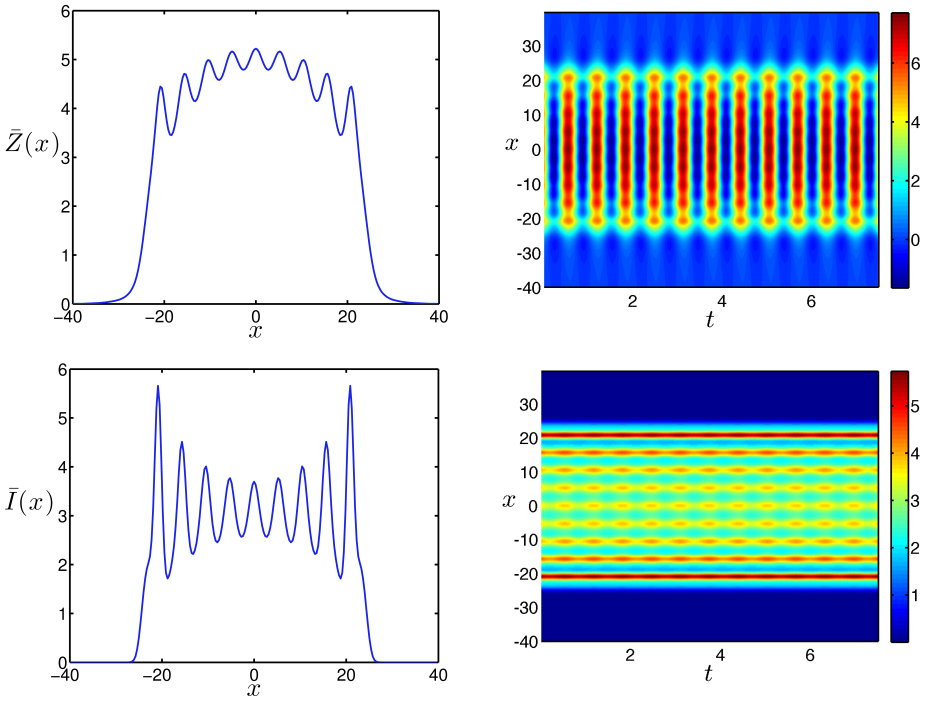

Fig. 8.17: Simulation for region ($\mathrm{II_a}$) with finite illumination inside the Hopf bifurcation. Parameters: $\Delta = -2.2$, $\rho = 1.13$, $\Omega = 10$, $\gamma = 0.1$ and injection amplitude of $E = 2.2$.

9. QUADRATIC COUPLING

In this section we assume that the intracavity membrane is placed at a node of the intracavity field. Hence, we start from the normalized equations of subsection 7.3.1,

$$\partial_\tau F = \left(-1 + i\Delta + i\nabla^2 \mp iZ^2\right) F + E, \tag{9.1a}$$

$$\partial_\tau^2 Z + \gamma\partial_\tau Z + \Omega_0^2\left(1 - \rho^2\nabla^2\right) Z = \mp 2\Omega_0^2 Z\left|F\right|^2, \tag{9.1b}$$

The interesting phenomena of this equations, which we show in the following, arise when selecting the sign $'+'$ in $'\mp'$. Choosing $'-'$ the equation for the displacement will behave as a damped harmonic oscillator and its solutions will tend to zero.

9.1 Homogeneous solutions and stability analysis

the homogeneous steady state verifies the equations

$$E^2 = \left[1 + \left(\Delta + \bar{Z}^2\right)^2\right]\bar{I}, \tag{9.2a}$$

$$h\bar{Z} = 2\bar{I}\bar{Z}, \tag{9.2b}$$

where $\bar{I} = \left|\bar{F}\right|^2$. We find two homogeneous steady states, the trivial solution

$$\left\{\bar{I} = \frac{E^2}{1+\Delta^2}, \bar{Z} = 0\right\}, \tag{9.3}$$

and the symmetric solution for Z

$$\left\{\bar{I} = \frac{1}{2}, \bar{Z} = \pm\sqrt{\pm\sqrt{2E^2 - 1} - \Delta}\right\}, \tag{9.4}$$

which exist from $E^2 \geqslant (1+\Delta^2)/2$ for positive Δ and from $E^2 \geqslant 1/2$ for negative Δ. In the later case, $\Delta < 0$, the response exhibited is four-valued

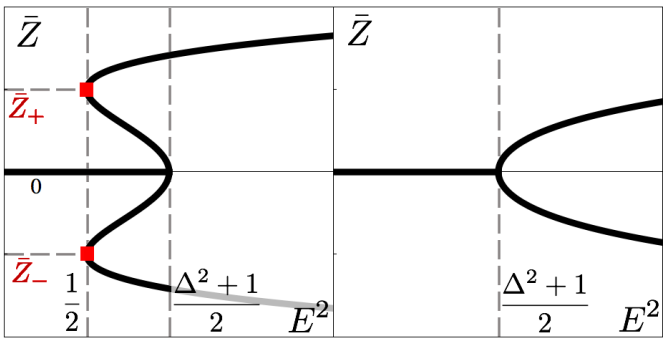

Fig. 9.1: $\bar{Z}$ vs E^2. Left, Σ-shape solution with $\Delta < 0$. Right, C-shape solution with $\Delta > 0$.

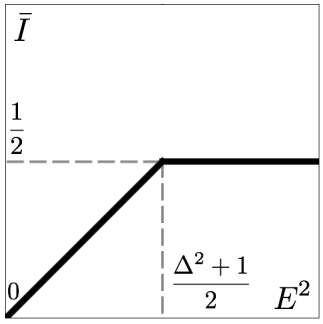

Fig. 9.2: $\bar{I}$ vs Δ for every case. Valid for $\Delta < 0$ and $\Delta > 0$

or Σ-shaped and its returning points will be at $\bar{Z} = 0$ and $\bar{Z}_\pm = \pm\sqrt{-\Delta}$. As shown in Fig. 9.1 on the left side, the solutions will coexist for $1/2 \geqslant E^2 \geqslant (1+\Delta^2)/2$. On the contrary, for positive delta, $\Delta > 0$, the symmetric solution will be bi valued or C-shaped and it will occupy different injection interval than the trivial solution.

Along this chapter we will find a lot of similarities between the quadratic and the linear coupling cases. However, at this moment we can already point out one of their main differences: now we will have the multivalued solutions only in the displacement, and not on the field intensity, which we will have a very simple solution for every case (Fig. 9.2).

As in previous chapter, we perform a standard linear stability analysis by adding small plane wave perturbations around the homogeneous steady

states $(\bar{F},\bar{Z})$ in the next way:

$$F = \bar{F} + \delta F e^{i\mathbf{k}\mathbf{r}'} e^{\lambda\tau}, \tag{9.5}$$

$$Z = \bar{Z} + \delta Z e^{i\mathbf{k}\mathbf{r}'} e^{\lambda\tau}, \tag{9.6}$$

By substituting in the Eqs. 7.3.1 we obtain the next system:

$$\left\{\lambda + \left[1 - i\left(\Delta - k^2 + \bar{Z}^2\right)\right]\right\}\delta F = 2i\bar{Z}\bar{F}\delta Z, \tag{9.7a}$$

$$\left\{\lambda\left(\lambda+\gamma\right) + \Omega_0^2\left(h + k^2\rho^2\right) - 2\Omega_0^2\bar{I}\right\}\delta Z = \\ +2\Omega_0^2\bar{Z}\left(\bar{F}\delta F^* + \bar{F}^*\delta F\right). \tag{9.7b}$$

where $k = |\mathbf{k}|$. By eliminating the variables, an eigenvalues equation for λ and k is got. If we plug the trivial solution (Eq. 9.3) in it, we obtain

$$0 = \lambda\left(\lambda+\gamma\right) + \Omega_0^2\left(h + k^2\rho^2 - 2\bar{I}\right), \tag{9.8}$$

that for $\lambda = 0$ predicts a bifurcation for

$$\bar{I} = \frac{1 + k^2\rho^2}{2}. \tag{9.9}$$

which is minimum at $k = 0$. Therefore, it corresponds a homogeneous bifurcation that makes the trivial state unstable just when it connects with the symmetric solution, at $E^2 = (1 + \Delta^2)/2$. The stability of the latter is given by the fourth order polynomial: $C\left(k^2;\lambda\right) \equiv \sum_{n=0}^{4} c_n\left(k^2\right)\lambda^n = 0)$, where after simple algebra we obtain: $c_4 = 1$, $c_3 = 2 + \gamma$

$$c_2 = 1 + 2\gamma + \Omega_k^2 + (\bar{Z}^2 + \Delta_k)^2, \tag{9.10a}$$

$$c_1 = \gamma\left[1 + \left(\bar{Z}^2 + \Delta_k\right)^2\right] + 2\Omega_k^2, \tag{9.10b}$$

$$c_0 = 4\bar{Z}^2\left(\bar{Z}^2 + \Delta_k\right)\Omega_0^2 + \left[1 + \left(\bar{Z}^2 + \Delta_k\right)^2\right]\Omega_k^2, \tag{9.10c}$$

where $\Omega_k^2 \equiv \Omega_0^2\rho^2k^2$.

Pitchfork bifurcation. Let us consider first the static instabilities. The solutions for $c_0 = 0$ are:

$$\bar{Z}_{PB}^2 = \frac{-\Delta_k(2 + k^2\rho^2) \pm \sqrt{4\Delta_k^2 - 4k^2\rho^2 - k^4\rho^4]}}{4 + k^2\rho^2} \tag{9.11}$$

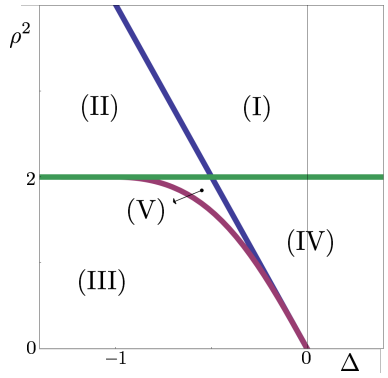

Fig. 9.3: ρ^2 vs Δ map. $\rho^2 = 2$ in green. $\rho^2 = \rho_1^2 = -4\Delta$ in blue. And $\rho^2 = \rho_2^2 = -4\Delta/(\Delta^2 + 1)$

which for a fixed $k = 0$ and $\Delta < 0$ are the returning points of the Σ-shape solution $\bar{Z}_\pm = \pm\sqrt{-\Delta}$. Therefore, the branches between $\bar{Z}_+$ and $\bar{Z}_-$ of the homogeneous solution are unstable. Allowing k to vary, pattern forming instabilities appear with a strong dependence on ρ.

As in the linear coupling model, this static bifurcation only depends on Δ and ρ^2, so we will, again, explain its behaviour on the $< \Delta, \rho^2 >$ plane[1], Fig. 9.3. In this case, we find that there are five relevant scenarios or regions that, as expected, are closely related to the ones in the linear coupling case[2]. We will also denote them by Roman numbers from (I) to (V).

In the following, in order to have a full picture of this bifurcation, we are going to explain in detail each one of the regions, but first, let us explain the meaning of the lines of the $< \Delta, \rho >$ plane plot, 9.3. The blue line corresponds to $\rho_1^2 = -4\Delta$, and is the value of ρ, which if lower, $\bar{Z}_{PB}$ will present a local maximum as a function of k for $k \neq 0$. On the other hand, the green line, $\rho^2 = 2$, represent whether or not $\bar{Z}_{PB}$ tends to infinity as a real value when $k \to \infty$. So for $\rho^2 < 2$ there will always be a pattern

[1] Note that here, in contrast with the linear coupling case the plot is with ρ^2.

[2] Although there is a relation one to one in both coupling cases, remember that in the linear coupling case there was a sixth scenario (VI) in which part of the lower branch of the multivalued solution was unstable. We won't be seeing this in the quadratic coupling model as the trivial solution ($\bar{Z} = 0$ and $\bar{I} = \frac{E^2}{1+\Delta^2}$) is always stable until it connects with the non trivial solution.

forming instability. The magenta line denoted by

$$\rho_2^2 = -\frac{4\Delta}{1+\Delta^2}. \tag{9.12}$$

represents a special feature which will be explained later. Finally, the black line at $\Delta = 0$ separates regimes where there is coexistence between solutions and those where there is not.

We illustrate, in Fig. 9.4, the entrance and exit points of the bifurcations for each of the regions. For each scenario, we find in this plot, on the left, the steady solution of the system in a displacement ($\bar{Z}$) vs injection amplitude (E) plot, which if unstable, is showed in a dashed line. Besides, by only showing $Z \geq 0$ we can study all the features of this case, which will be closely related with the ones of the S-shape of linear coupling, but in this case, we will have an extra characteristic, as the solution is symmetric, any bifurcation that you find for positive Z is also present for negative Z and, in both cases, the trivial solution ($\bar{Z} = 0$) plays the role of the S-shape solution's lower branch in the linear coupling case. Therefore and, as all the features are due to the shape of the displacement, not the intensity, from now on we will describe all the bifurcations only showing $Z \geq 0$. On the right, we represent the condition for the Pitchfork bifurcation, $\bar{Z}_{PB}$, versus k.

- Region (I). This region is the only one where there is no Pitchfork bifurcation. It is delimited below by $\rho^2 = 2$, and, on the left, by ρ_1. We illustrate the part inside the multivalued region ($\Delta < 0$) in Fig. 9.4.

- Region (II). Bounded by ρ_1 on the right and $\rho^2 = 2$ underneath. There is pattern forming instability from $\bar{Z}_+$ to $\bar{Z}_{PB,+}$, which as coexisting with the stable trivial solution will lead to the formation of localized structures, as in the linear coupling case. We can see in Fig. 9.4, that $\bar{Z}_{PB,+}$ corresponds to a maximum in the $\bar{Z}$ vs k plot. The expression of $\bar{Z}_{PB,+}$ is too lengthy to give it here but in order to give some insight , it will be larger as ρ^2 gets closer to 2.

- Region (III). This region is delimited by $\rho^2 = 2$ above and the magenta, ρ_2. In this case all the upper branch is unstable, from the upper returning point $\bar{I}_+$ to ∞ (Fig. 8.3).

- Region (IV) Delimited by ρ_1 and $\rho^2 = 2$. also by $\Delta = -\sqrt{3}$. It is shared between coexistence and not coexistence of solutions. In this

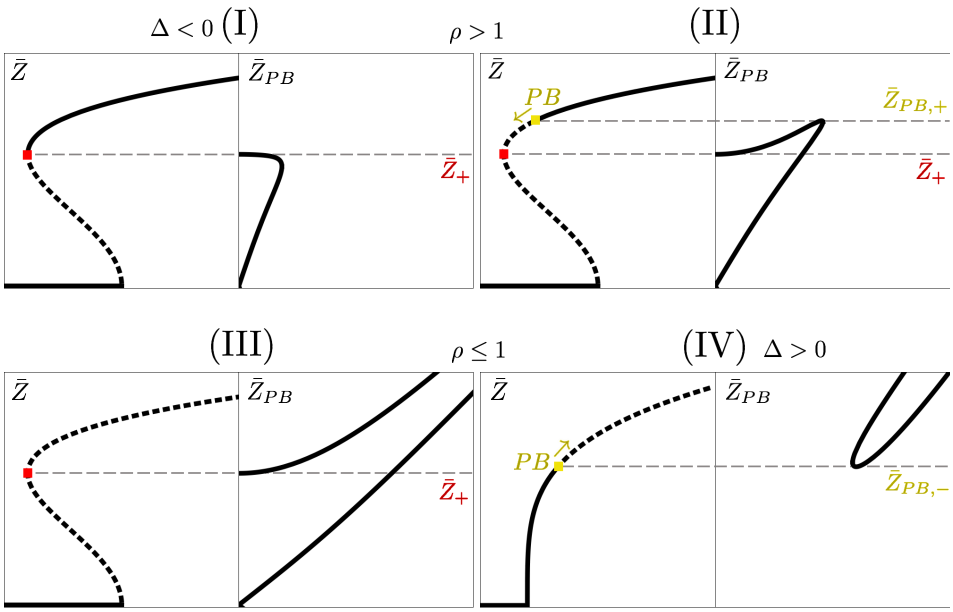

Fig. 9.4: Situation of the Pitchfork bifurcation. (I) There is no Pitchfork bifurcation. (II) There is a Pitchfork bifurcation between $\left[\bar{Z}_+, \bar{Z}_{PB,+}\right]$. (III) All the upper branch of the multivalued solution is unstable. (IV) There is a Pitchfork bifurcation between $\left[\bar{Z}_{PB,-}, \infty\right]$

case, a minimum of $\bar{Z}_{PB}$ vs k arises. This pattern forming instability goes from $\bar{Z}_{PB,-}$ to ∞. Also, the expression of $\bar{I}_{PB,-}$ is too lengthy to give it here but it is larger as ρ^2 increases getting closer to 2.

- Region (V) This region is in between $\rho^2 = 2$, ρ_1 and ρ_2. As we can see in Fig. 9.5, the features of regions (II) and (IV) are in (V). The pattern instability occupies $\bar{Z} \in \left[\bar{Z}_+, \bar{Z}_{PB,+}(\text{local})\right] \cup \left[\bar{Z}_{PB,-}(\text{local}), \infty\right]$.

Hopf bifurcation. Now lets study the behaviour of the self-pulsing instability. We will call the entering point of the Hopf $Z_{HB,-}$ and the existing point $Z_{HB,+}$, so between $Z_{HB,+} > Z > Z_{HB,-}$ we will be inside the bifurcation with a time pulsing solution. As it depends on all the parameters of the model (ρ, Ω_0, γ and Δ), the expression is lengthy and difficult to manage, so we will study first the physical limit, $\gamma \ll \Omega_0$ (the mechanical oscillations are of high-Q) and $\gamma \ll 1$ (the damping rate of the mirror oscillations is much smaller than the cavity damping rate). In this

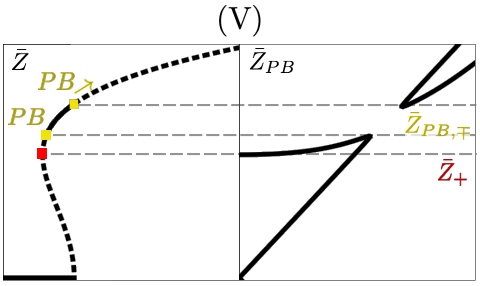

Fig. 9.5: Scenario (V). There is a Pitchfork bifurcation between $\bar{Z} \in \left[\bar{Z}_+, \bar{Z}_{PB,+}(\text{local})\right] \cup \left[\bar{Z}_{PB,-}(\text{local}), \infty\right]$.

limit $Z_{HB,+}$ goes to infinity and $Z_{HB,-} = \bar{Z}_+$ for $\Delta < 0$ and $Z_{HB,-} = 0$ for $\Delta > 0$. So all the symmetric solution will be unstable.

9.2 Numerical simulation

We perform a numerical simulation using the split-step method (Appendix H). Firstly, as they are intrinsic to the method, we are going to solve in periodic boundary conditions. Later, we will show some examples with fixed boundaries and illumination with a finite transverse extension.

Exactly as in the linear coupling case, all the simulations are started with a small amount of noise around 0 for all variables. We have checked that all the analytical predictions from the linear stability analysis can be reproduced. We find patters within all the regions of the parameter space delimited by pattern forming instabilities: regions (II − V) and, when they coexist with the trivial stable homogeneous solution (bistability), we find solitons in regions (II-III) and (V).

Solitons are excited exactly in the same way as in the linear coupling case.

As for the limit $\gamma \ll \Omega_0$ and $\gamma \ll 1$ the Hopf bifurcation occupies the whole branch ($Z_{HB,-} = \bar{Z}_+$) we are going to show an example out of this regime where the Pitchfork ant the Hopf can be well differentiated. In Fig. 9.6 we can see in a $\bar{Z}$ vs E^2 plot the coexistence of static patterns (in dashed-dotted yellow) with an homogeneous solution ($\bar{Z} = 0$) which provides the appearance of solitons (in dotted green). In this case, the solitons branch will have its own Hopf bifurcation and, therefore, the maximum and minimum of the time evolution of the peak is represented in this figure. In this case, we will also have an inhomogeneous self pulsing instability from $\bar{I}_{HB,-}$ where

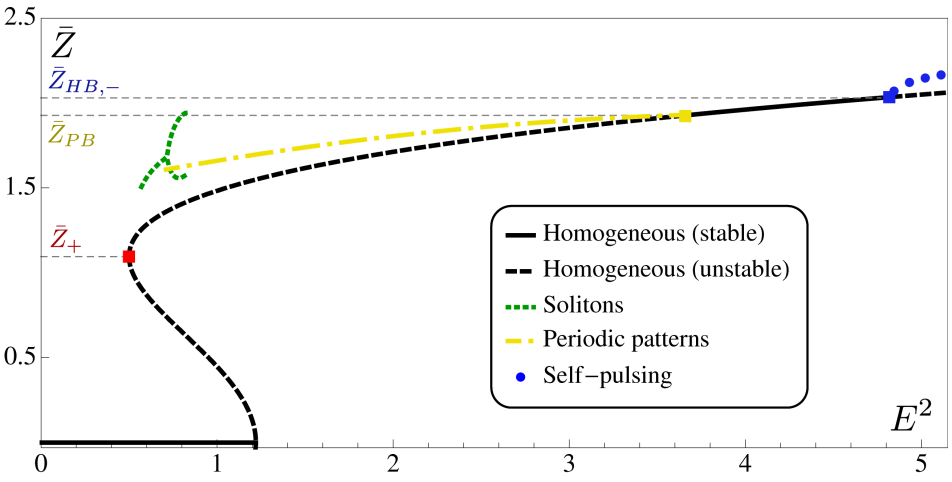

Fig. 9.6: Simulation for region ($\mathrm{II_a}$). Parameters: $\Delta = -1.2$, $\rho = 1.476$, $\Omega = 0.4$, $\gamma = 1$. Evolution with the injection of the peaks of the static pattern forming instabilities: periodic patterns (in dashed-dotted yellow), solitons (in dotted green, maximum and minimum of the peak if necessary) and the mean in time of the self-pulsing solutions (in blue filled circles)

the mean in time of the self-pulsing solutions are plotted in blue filled circles. All these features are also represented for the intracavity intensity in Fig. 9.7.

An example of the solitons is showed in Fig. 9.8 for the displacement in upper row and for the intracavity intensity in the lower row. On the right, we can see the time evolution in a position x versus time t contour plot. The simulation is started with a small amount of noise around 0 in the variables and a flat profile in the injection. Including two appropriate gaussians at $x = \pm 20$ in the amplitude injection we finally turn on two solitons at $t = 1100$. Then we turn off the soliton at $x = -20$ and after a while turn another one at $x = -30$ obtaining what we have on the left side. We can not choose whether the soliton will belong to the positive or negative branch of the displacement, that only depends on the initial noise. We have studied what happens when two solitons collide. Once we have formed them using the anterior criteria, we include a small gradient in the injection amplitude whose maximum is at $x = 0$. As the solitons are attracted to bigger intensities they get closer until we arrive to a time independent solution. At this moment we remove the gradient in the

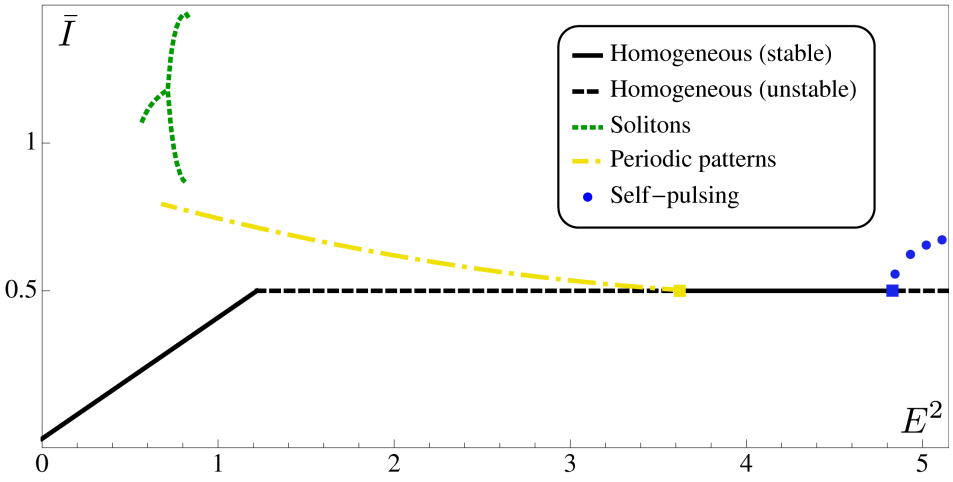

Fig. 9.7: Simulation for region ($\mathrm{II_a}$). Parameters: $\Delta = -1.2$, $\rho = 1.476$, $\Omega = 0.4$, $\gamma = 1$. Evolution with the injection of the peaks of the static pattern forming instabilities: periodic patterns (in dashed-dotted yellow), solitons (in dotted green, maximum and minimum of the peak if necessary) and the mean in time of the inhomogeneous self-pulsing solutions (in blue filled circles)

injection illuminating again with a flat profile. As shown in Fig. 9.9a, we have found that they repel when they have opposite sign an they attract when they have the same sign Fig. 9.9b.

Also, an example of periodic patterns is in Fig. 9.10. On the left the final result of the time evolution represented on the right side. In this case the simulation has been started at plane $E^2 = 2$ in Fig. 9.6 forcing a domain wall at $x = 0$. In Fig. 9.11 the inhomogeneous Hopf is illustrated. On the left the final result of the time evolution represented on the right side. In this case the simulation has been started with plane injection at $E^2 = 5$, obtaining patterns that are moving to the right with time. If we force a domain wall in this situation we have to go far from them in order to fulfil the predictions.

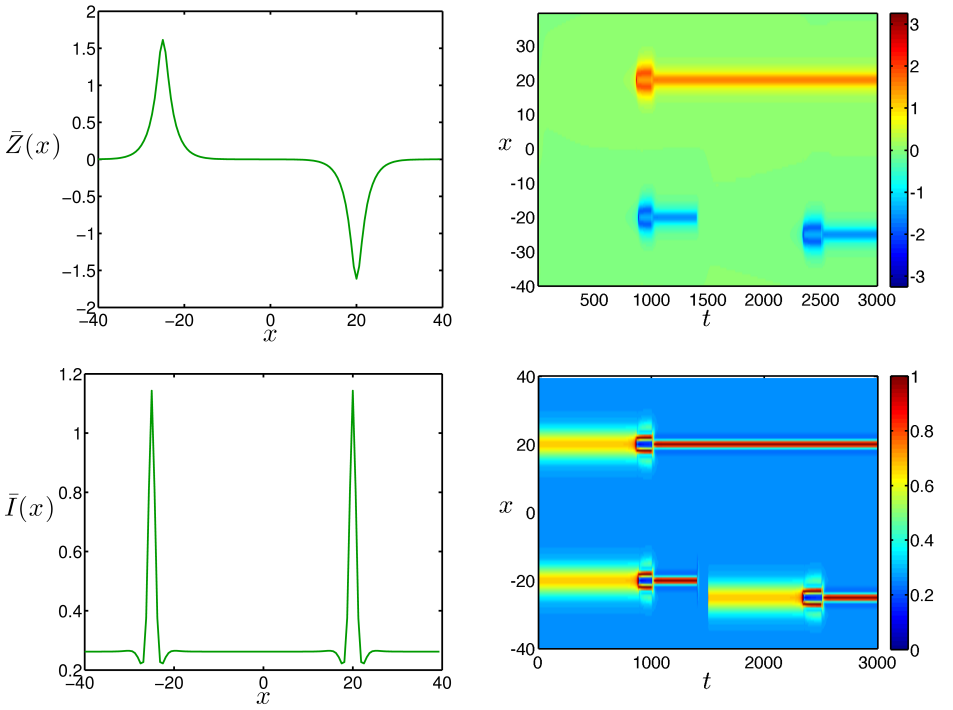

Fig. 9.8: Solitons for the displacement in upper row and for the intracavity intensity in the lower row. On the right, we can see the time evolution in a position x versus time t contour plot, and on the left, its final result. Parameters: $E^2 = 0.9$ $\Delta = -1.2$, $\rho = 1.476$, $\Omega = 0.4$, $\gamma = 1$. We plug the solitons maintening a gaussian of 0.5 height over a flat line at E and $\sigma = 3$ for 10^5 steps. We can also erase them and turn them on in another place

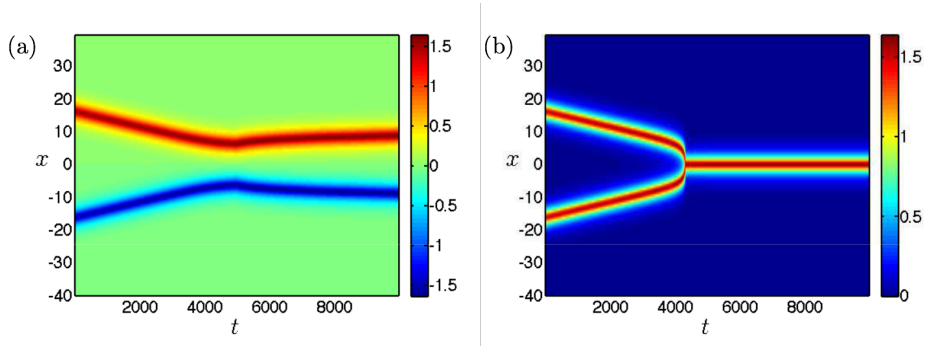

Fig. 9.9: Clash of solitons of (a) opposite sign and (b) the same sing for $\bar{Z}$. Parameters: $E^2 = 0.9$, $\Delta = -1.2$, $\rho = 1.476$, $\Omega = 0.4$, $\gamma = 1$. We include an small gradient in the injection amplitude whose maximum is at $x = 0$. As the solitons are attracted to bigger intensities they get closer until we arrive to a time independent solution. At this moment we remove the gradient in the injection illuminating again with a flat profile.

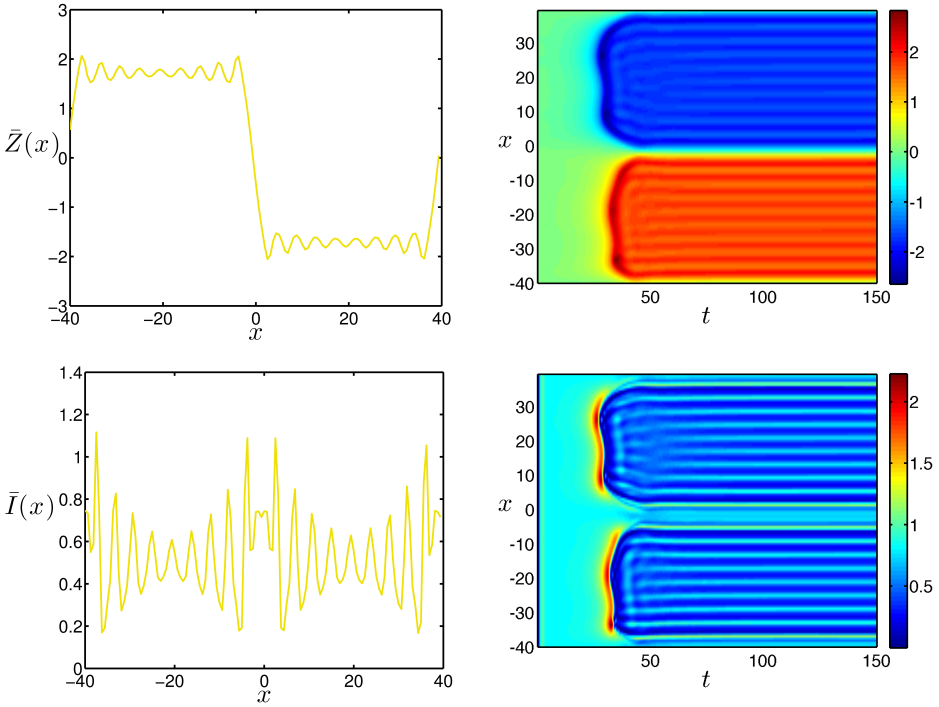

Fig. 9.10: Patterns. Parameters: $E^2 = 2$, $\Delta = -1.2$, $\rho = 1.476$, $\Omega = 0.4$, $\gamma = 1$.

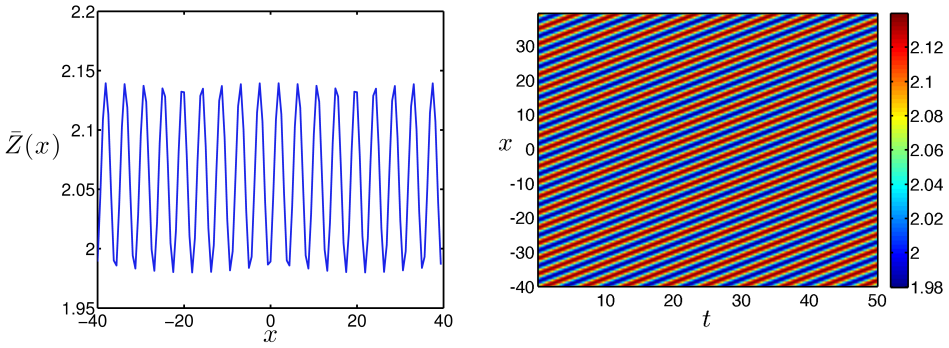

Fig. 9.11: Travenling rolls originated at the Hopf bifurcation. Parameters: $E^2 = 5$, $\Delta = -1.2$, $\rho = 1.476$, $\Omega = 0.4$, $\gamma = 1$.

10. EXPERIMENTAL IMPLEMENTATION

State-of-the-art optomechanical setups allow for the use of silicon nitride membranes both as intracavity elements dispersively coupled to the light contained in the resonator [161–168] or directly as end mirrors, hence sensitive to radiation pressure [169–171]. However, in all the experiments to date the membrane is held by a frame, what means that the boundary conditions are fixed and no true mechanical homogeneous mode exists, so that they are described by our model equations with $\Omega_{\mathrm{m}} = 0$, what prevents the existence of 2D patterns. A most relevant conclusion of our numerical study is that the models above cease to exhibit patterns as soon as the homogeneous mode is removed. Even if it is a conclusion reached through the numerical analysis, this has been extensive enough for us to affirm that the existence of a mechanical homogeneous mode is a necessary condition for spatial instabilities to occur, what is important to keep in mind when proposing realistic implementations of the models as we pass to do now.

In the following we show that provided that only a single membrane mode is excited in one of the transverse directions (say y), these same setups allow for the study of the phenomenology predicted in this thesis in 1D along the orthogonal direction (x). Let's consider our normalized optomechanical models (section 7.3.1) without the homogeneous mode (substituting $(1 - \rho^2\nabla^2)$ with $-\rho^2\nabla^2$), for which the equation of motion of the noninteracting normalized membrane's displacement field $Z_{2\mathrm{D}}(\bar{\mathbf{r}}, \tau)$[1] is

$$\partial_\tau^2 Z_{2\mathrm{D}} + \gamma \partial_t Z_{2\mathrm{D}} - \Omega^2 \rho^2 \nabla^2 Z_{2\mathrm{D}} = 0, \tag{10.1}$$

which is the left hand side of the equations 7.33 and 7.35[2]. Now we supplement this equation with the chosen boundary conditions in the x direction, and fixed ones in the y direction, $Z_{2\mathrm{D}}(\bar{x}, \bar{y} = \pm\bar{L}_y, t) = 0$ in particular (note that we take $\bar{y} = 0$ in the center of the membrane). Under

[1] The overbar, again, denotes the normalization to l_c.

[2] Note that the normalization is different between coupling models

such conditions the normal modes in the y axis are given by

$$u_n(\bar{y}) = \sqrt{\frac{2}{\bar{L}_y}} \times \begin{cases} \cos \bar{k}_n \bar{y} & n \in \text{odd} \\ \sin \bar{k}_n \bar{y} & n \in \text{even} \end{cases}, \tag{10.2}$$

where $n = 1, 2, ...$ and $\bar{k}_n = n\pi/\bar{L}_y$. Therefore, in general the displacement field can be written then as

$$Z_{2\mathrm{D}}(\bar{\mathbf{r}}, t) = \sum_{n=1}^{\infty} u_n(\bar{y}) Z_n(\bar{x}, t), \tag{10.3}$$

where $Z_n(\bar{x}, t)$ is the displacement field along the $\bar{x}$ axis, associated to the n'th $\bar{y}$-mode. Let us assume that only the fundamental mode is excited, so that $Z_n(\bar{x}, t) = \delta_{n1} Z(\bar{x}, t)$, denoting by $Z(\bar{x}, t)$ its corresponding displacement field along the $\bar{x}$ direction. Projecting the equation of motion into this fundamental mode, $\bar{u}_1(\bar{y})$, we then get

$$\partial_\tau^2 Z + \gamma \partial_\tau Z + \underbrace{\Omega^2 \rho^2 \bar{k}_1^2}_{\Omega_{1\mathrm{D}}^2} Z - \underbrace{\Omega^2 \rho^2}_{\Omega_{1\mathrm{D}}^2 \rho_{1\mathrm{D}}^2} \partial_{\bar{x}}^2 Z = 0, \tag{10.4}$$

which is an equation of motion for the displacement field in the $\bar{x}$ direction, but with an effective homogeneous mode which oscillates at frequency $\Omega_{1\mathrm{D}} = \Omega \rho \bar{k}_1 = \pi(v/\gamma_\mathrm{c} l_\mathrm{c})/\bar{L}_y$ and with effective 1D rigidity parameter $\rho_{1\mathrm{D}} = \bar{k}_1^{-1} = \bar{L}_y/\pi$. Hence, we see that an original 2D model with no homogeneous mode, can lead to an effective 1D model with homogeneous solutions provided that only one mode (the fundamental mode in this derivation) is excited along one of the transverse directions.

In summary, we have argued how a 2D membrane in which only one mode is excited along one of the transverse directions can give rise to an effective 1D model of the type we want. The assumption that only the fundamental mode is excited in the y direction, leads to the result that the effective rigidity parameter $\rho_{1\mathrm{D}}$ in the x direction is controlled solely by the width of the membrane in the y direction (in units of the optical diffraction length l_c), while the effective frequency of the homogeneous mode $\Omega_{1\mathrm{D}}$ in the x direction depends additionally on the speed of sound (in units of the product of the cavity decay rate and diffraction length, $\gamma_\mathrm{c} l_\mathrm{c}$). A choice of the system parameters according to this simple picture already allows us to find regions of pattern formation, as we pass to describe in more detail now.

Before continuing it is important to say that there is an alternative of the experimental realization for the optomechanial model. In this case,

we don't have to renounce to the homogenous mode because the device that we propose intrinsically has it. It consists in an an array of weakly coupled mirrors all of them fixed to a wall with identical springs. A full demonstration of the discrete model and numerical simulations are given in appendix G.

10.1 Details about the numerical simulation of the proposed implementation

In the main text we showed two examples of structures appearing when numerically simulating the quasi-1D implementation explained in the previous section, what indeed proves that patterns can be observed with it. Let us here give details about the actual parameters used for the quasi-1D simulations, although, patterns can be easily found wherever they are expected to appear in the bifurcation diagram.

Let us first remark that in this case we have not assumed the existence of a prior homogeneous mode, that is, we have numerically simulated the equations

$$\partial_\tau F = \left[-1 + \mathrm{i}\left(\Delta + \nabla^2 + Z^\mu\right)\right] F + E, \tag{10.5a}$$

$$\partial_\tau^2 Z + \gamma \partial_\tau Z - \Omega^2 \rho^2 \nabla^2 Z = \Omega^2 Z^{\mu-1} |F|^2, \tag{10.5b}$$

Note that in both sets of equations Ω can be eliminated with the change $\Omega\rho \to \rho$, $\Omega F \to F$, and $\Omega E \to E$, but we have decided to keep it just so the definition of normalized fields and parameters is the same as in the main text. This equation is supplemented with fixed boundary conditions at the rectangular frame of the membrane, that is, $Z(\pm\bar{L}_x/2, \bar{y}) = 0 = Z(\bar{x}, \pm\bar{L}_y/2)$, which we directly impose in the split-step method. Of course, $\bar{L}_x$ and $\bar{L}_y$ are the dimensions of the membrane along the x and y directions, respectively, normalized to the diffraction length l_c. Note that the case of previous sections corresponds to the ideal situation of having an infinite membrane along x, while in this section we want precisely to prove numerically that even in the case of having finite length along x, the patterns predicted by the ideal model can be found as long as the membrane is long enough to be able to hold the computed solutions.

In Fig. 10.1.(a) we show a soliton obtained from the linear model ($\mu = 1$), expected to appear wherever bistability is present and the upper branch is unstable because of the static pattern forming bifurcation, in this case, region (III) (Fig. 8.3). In the same scenario, with larger injections, we

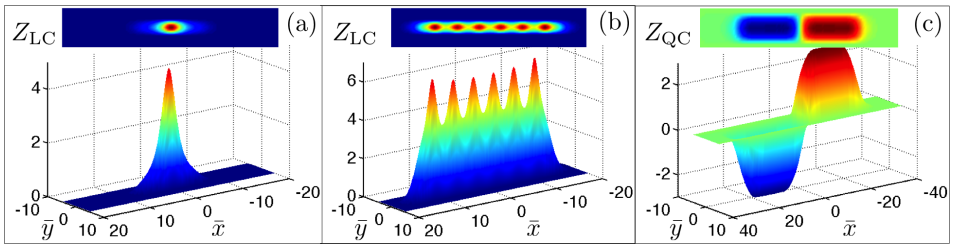

Fig. 10.1: We show a soliton (a) and patterns (b) for the linear coupling case, and a domain wall (c) for the quadratic coupling case.

can obtain the patterns shown in Fig. 10.1.(b). In order to be in this region, we have chosen the following parameters in (10.5): $\Omega = 10$, $\gamma = 0.1$, $\rho = 1$, $\Delta = -2.2$. In addition we have chosen widths $\bar{L}_y = 3.125$ and $\bar{L}_x = 40$ for the membrane, and a quasi-plane injection of finite width given by the supergaussian profile $E(\bar{\mathbf{r}}) = E_0 \exp[-(\bar{x}^{20}/2\sigma_x^{20}) - (\bar{y}^{20}/2\sigma_y^{20})]$, with $\sigma_x = 7$, $\sigma_y = 3$, and $E_0 = 1.45$ for the soliton and $E_0 = 2.50$ for the patterns . Note that for these choices, the effective 1D parameters become $\rho_{1\rm D} = 3.125/\pi \approx 0.995$ and $\Omega_{1\rm D} = \Omega/\rho_{1\rm D} \approx 10.05$, according to the simple analysis of the previous section when only the fundamental mode is excited in the y axis.

On the other hand, in Fig. 10.1.(c) we show a domain wall expected to appear in the quadratic model ($\mu = 2$) when the nontrivial homogeneous stationary solutions with opposite signs coexist, which occurs in region (IV) of Fig. 9.4 just before the pitchfork bifurcation. In this case we have simulated equations (10.5), choosing $\Omega = \sqrt{0.1}$, $\gamma = 0.1$, $\rho = 1$, $\Delta = 5$, $\bar{L}_y = 6.25$ and $\bar{L}_x = 80$, and the same kind of supergaussian illumination as before, but with $\sigma_x = 7.5$, $\sigma_y = 3$, and $E_0 = 6.8$. These parameters lead effective 1D ones $\rho_{1\rm D} = 6.25/\pi \approx 2$ and $\Omega_{1\rm D} = \Omega/\rho_{1\rm D} \approx 0.16$. Let us remark that we haven't chosen a larger value of Ω because otherwise the Hopf bifurcation tends to the point where the trivial and nontrivial solutions connect, making it impossible to find stationary solutions above that point (although it is possible to find dynamic ones, such as pulsing domain walls).

V

CONCLUSIONS

In this final chapter we will give a brief description of the methodology and results presented in this thesis.

In the first part, we have proposed a way to achieve locking at the degenerate frequency of the down-converted fields in a type II optical parametric oscillator. We applied a master equation approach, using the corresponding stochastic equations to study the system. In the classical limit, we have studied the stability of the static solutions finding, among others, a self-pulsing bifurcation which provides, just at the beginning of the instability, the locking point above threshold at which the down-converted modes become degenerate. Finally, by computing the covariance matrix we have studied the squeezing and entanglement properties of the system, finding good levels for both at the locking point, even when working out of the idealized symmetric case that we analyzed for analyticity.

In the second part, we have studied an array of coupled cavities, each one interacting strongly with a two level emitter. From the master equation in the Bloch mode basis, we have directly calculated the equations for the correlators, which we have split to the lowest order non-zero correlators, obtaining equations for the populations. We reached two main conclusions. First, we have seen that correlations build-up in the cavity array and decay exponentially as the distance between cavities tends to infinity for any dimension of the array. As intuitively expected, the associated correlation length increases by increasing photon tunneling between cavities. We also find that the collective coherence manifest strongly in the local cavity properties such as intensity and spectrum of emission. In particular, lasing and its typical photoluminescence lineshape, the Mollow triplet, can be observed far out of resonance between the emitter and the cavity, what we explained as a result of the appearance of collective photonic modes.

In the third part, we have proposed a multimode optomechanical system in a membrane in the middle configuration. We have studied the two characteristic situations in which the frequency shift felt by the cavity field depends linearly and quadratically on the membrane's displacement, what is accomplished by properly positioning the membrane inside the cavity. After the derivation of the model equations, we have performed a stability analysis of the homogeneous steady states from which we have predicted a variety of bifurcations. Special attention has been paid to the inhomogeneous ones that lead to the formation of patterns. Through a numerical analysis, we have seen how static patterns and solitons arise, as well as self-pulsing solutions. One of the main conclusions of this work

is that, for the appearance of these structures, a homogeneous mode is needed, that is, the possibility of inducing a homogeneous displacement of the membrane under plane illumination. Although a clamped membrane does not have such a homogeneous mode (the frame imposes fixed boundary conditions), we have proposed an experimental implementation in which the membrane behaves according an effective model with an homogeneous mode in one dimension. Under these considerations, all the predicted solutions have been found. Also, an alternative experimental realization based on coupled oscillators is presented in the Appendix G, where the homogeneous mode is directly implemented in the device.

APPENDIX

A. NOTIONS OF QUANTUM MECHANICS.

For our proposes is enough to know how to treat quantitatively a single-mode field, being the multimode a straight forward extension of it [46].

By solving Maxwell equations inside a cavity with perfectly conducting walls, one can find that the Hamiltonian H for a single mode field with frequency ω, is formally equivalent to a harmonic oscillator of unit mass, where the electric and magnetic fields, apart from some scale factors, play the roles of canonical position and momentum.

$$H = \frac{1}{2}(p^2 + \omega^2 q^2), \tag{A.1}$$

Through the quantization of the one dimensional harmonic oscillator [172] we exchange the canonical variables q and p for the classical system by their operator equivalents $\hat{q}$ and $\hat{p}$ which satisfy the canonical commutation relation $[\hat{q}, \hat{p}] = i\hbar$.

$$\hat{H} = \frac{1}{2}(\hat{p}^2 + \omega^2 \hat{q}^2), \tag{A.2}$$

The operators $\hat{q}$ and $\hat{p}$ are Hermitian and therefore correspond to observable quantities. However, it is convenient, to introduce the non-Hermitian (and therefore non-observable) annihilation ($\hat{a}$) and creation ($\hat{a}^\dagger$) operators through the combinations

$$\hat{a} = (2\hbar\omega)^{-1/2}(\omega\hat{q} + i\hat{p}) \quad \text{and} \quad \hat{a}^\dagger = (2\hbar\omega)^{-1/2}(\omega\hat{q} - i\hat{p}) \tag{A.3}$$

which satisfy the commutation relation $[\hat{a}, \hat{a}^\dagger] = 1$. The Hamiltonian operator takes the form

$$\hat{H} = \hbar\omega\left(\hat{a}^\dagger\hat{a} + \frac{1}{2}\right). \tag{A.4}$$

The operator product $\hat{a}^\dagger\hat{a}$ is Hermitian and has a special significance and is called the *number operator*, which is denoted as $\hat{n} = \hat{a}^\dagger\hat{a}$. The Hamiltonian has the eigenvalues $\hbar\omega\left(n + \frac{1}{2}\right)$ where n is an integer ($n = 0, 1, 2, ..., \infty$).

The eigenstates are written as $|n\rangle$ and are known as number of *Fock states*, which are eigenstates of the number operator

$$\hat{n}\,|n\rangle = n\,|n\rangle\,. \tag{A.5}$$

The ground state of the oscillator (or vacuum state of the field mode) is defined by

$$a\,|0\rangle = 0 \tag{A.6}$$

From Eqs. A.4 and A.6 we see that the energy of the found state is given by $\langle 0|\,H\,|0\rangle = \hbar\omega/2$. The operators $\hat{a}$ and $\hat{a}^\dagger$ are lowering and raising operators for the harmonic oscillator ladder of eigenstates. In terms of photons they represent the annihilation and creation of a photon; hence the terminology, annihilation and creation operators. Application of the creation and annihilation operators to the number states yield

$$\hat{a}\,|n\rangle = \sqrt{n}\,|n-1\rangle \quad \text{and} \quad \hat{a}^\dagger\,|n\rangle = \sqrt{n+1}\,|n+1\rangle\,. \tag{A.7}$$

The state vectors for the higher excited states may be obtained from the vacuum by successive application of the creation operator

$$|n\rangle = \frac{(\hat{a}^\dagger)^n}{\sqrt{n!}}\,|0\rangle\,, \quad n = 0, 1, 2... \tag{A.8}$$

The number states are orthogonal

$$\langle n|m\rangle = \delta_{mn} \tag{A.9}$$

and complete

$$\sum_{n=0}^{\infty} |n\rangle\,\langle n| = 1 \tag{A.10}$$

Since the norm of these eigenvectors is finite, they form a complete set of basis vectors for a Hilbert space.

Coherent states: A more appropiate basis for many optical fields are the coherent states. The coherent states have an indefinite number of photons which allows them to have a more precisely defined phase than a number state where the phase is completely random. The product of the uncertainty in amplitude and phase for a coherent state is the minimum allowed by the uncertainty principle. In this sense they are the closest quantum mechanical states to a classical description of the field. We shall outline the basic properties of the coherent states below.

Coherent states can be obtained as eigenstates of the non-Hermitian annihilation operator $\hat{a}$. Clearly, these eigenstates can not be expected to be necessarily real. Let $|\alpha\rangle$ be such a state, with the complex number α denoting its eigen value. By definition, we thus have

$$\hat{a}\,|\alpha\rangle = \alpha\,|\alpha\rangle \tag{A.11}$$

Whatever $|\alpha\rangle$ it can be decomposed in the basis $\{|n\rangle\}$, which means

$$|\alpha\rangle = e^{-|\alpha|^2/2} \sum_{n=0}^{\infty} \frac{\alpha^n}{\sqrt{n}}\,|n\rangle \tag{A.12}$$

and using A.8 we can recast it as

$$|\alpha\rangle = \mathcal{D}(\alpha)\,|0\rangle\,, \quad \mathcal{D} \equiv e^{\alpha a^\dagger - \alpha^* a} \tag{A.13}$$

Thus, formally, the coherent state can be generated from the lowest (ground) state $|0\rangle$ by acting upon it with the operator $\mathcal{D}(\alpha)$ known as the *displacement operator*. Consider now the scalar product of two coherent states $|\alpha\rangle$ and $|\beta\rangle$

$$\langle\alpha|\beta\rangle = \exp\left(-\frac{|\alpha|^2}{2} + \alpha^*\beta - \frac{|\beta|^2}{2}\right) \tag{A.14}$$

we thus have

$$|\langle\alpha|\beta\rangle|^2 = e^{-|\alpha-\beta|^2} \tag{A.15}$$

which is small for $|\alpha - \beta|^2 \gg 1$, but never zero, i.e., the coherent states are non-orthogonal. However, the farther from each other (on the complex plane) the eigenvalues α and β are, the more "orthogonal" (less overlap) the two state are, but each state still contains all of the others. Thus the set of coherent states $\{|\alpha\rangle\}$ is continuous, normalized, but not orthogonal and they form an overcomplete basis, which is easily shown by noting that

$$1 = \int |\alpha\rangle\,\langle\alpha|\,\frac{d^2\alpha}{\pi} \tag{A.16}$$

B. LOGARITHMIC NEGATIVITY.

In this Appendix we explain how to compute the logarithmic negativity from a given two-mode covariance matrix V of a Gaussian state [29, 30, 49], e.g., the covariance matrix of the signal and idler modes that we have derived in 3.29. These quantity provides a measure of the entanglement levels between the two modes.

The Peres-Horodecki criterion [173] establishes that the state will separable only when the partial transposition of the bi-partite state leads to a well defined state (that is, a trace-one density operator with positive eigenvalues). The logarithmic negativity simply measures how much this criterion for separability is violated. In phase space, partial transposition is equivalent to a change of sign in the momentum of one of the modes. Hence, the first step to evaluate the logarithmic negativity consists in applying such change in the covariance matrix through the matrix

$$Z = \begin{pmatrix} 1 & 0 & 0 & 0 \\ 0 & 1 & 0 & 0 \\ 0 & 0 & 1 & 0 \\ 0 & 0 & 0 & -1 \end{pmatrix}, \tag{B.1}$$

leading to the covariance matrix of the partially-transposed state

$$\tilde{V} \equiv ZVZ. \tag{B.2}$$

Let us rewrite this matrix in the block form

$$\tilde{V} = \begin{pmatrix} A & C \\ C^T & B \end{pmatrix}. \tag{B.3}$$

where $A = A^T$, $B = B^T$, and C are 2x2 matrices. The positivity of the corresponding Gaussian state can be studied through the so-called *symplectic eigenvalues* $\nu_\pm$, which defining $\Delta(\tilde{V}) = \det A + \det B + 2 \det C$, can be found as

$$\nu_\pm^2 = \frac{\Delta(\tilde{V}) \pm \sqrt{\Delta^2(\tilde{V}) - 4 \det \tilde{V}}}{2}. \tag{B.4}$$

In particular, the covariance matrix $\tilde{V}$ will correspond to a physical Gaussian state only if both symplectic eigenvalues are larger or equal than one. The logarithmic negativity is then defined simply as

$$E_N = \sum_j F(\nu_j) \tag{B.5}$$

where

$$F(x) = \begin{cases} -\log x & x < 1 \\ 0 & x \geq 1 \end{cases}. \tag{B.6}$$

C. JAYNES-CUMMINGS MODEL.

The JCM is a paradigmatic model for light-atom interaction [46, 174]. Originally proposed in 1963, it has received a lot of attention especially after the different experimental implementations during the 90's.

Dipolar Hamiltonian The Hamiltonian that describes an electron bound to a nucleus under the usual Coulomb interaction $\Phi_{\text{coul}}(\hat{\mathbf{r}})$ in the presence of external fields is:

$$\hat{H}(\mathbf{r},t) = \frac{1}{2m}\left[\hat{\mathbf{p}} + e\mathbf{A}(\hat{\mathbf{r}},t)\right]^2 - e\Phi(\hat{\mathbf{r}},t) - e\Phi_{\text{coul}}(\hat{\mathbf{r}}) \tag{C.1}$$

where $\mathbf{A}(\hat{\mathbf{r}},t)$ and $\Phi(\hat{\mathbf{r}},t)$ are the vector and scalar potentials respectively of the external field (note that they depends on the quantized variables $\hat{p}$ and $\hat{r}$) and where -e is the electron charge, e taken to be positive and m its mass. The fields themselves are given by

$$\mathbf{E}(\hat{\mathbf{r}},t) = -\nabla\Phi(\hat{\mathbf{r}},t) - \frac{\partial\mathbf{A}(\hat{\mathbf{r}},t)}{\partial t} \tag{C.2}$$

$$\mathbf{B}(\hat{\mathbf{r}},t) = \nabla\times\mathbf{A}(\hat{\mathbf{r}},t) \tag{C.3}$$

and are invariant under the gauge transformations

$$\Phi'(\hat{\mathbf{r}},t) = \Phi(\hat{\mathbf{r}},t) - \frac{\partial\chi(\hat{\mathbf{r}},t)}{\partial t} \tag{C.4}$$

$$\mathbf{A}'(\hat{\mathbf{r}},t) = \mathbf{A}(\hat{\mathbf{r}},t) + \nabla\chi(\hat{\mathbf{r}},t) \tag{C.5}$$

assuming that $\nabla\mathbf{A}(\hat{\mathbf{r}},t) = 0$ that corresponds to a particular value of the vector potential, denoted by $\mathbf{A}_\perp(\hat{\mathbf{r}},t)$ (the transverse vector potential), which is particularly well adapted to problems in quantum optics, we now introduce a second gauge which is the Göppert-Mayer gauge defined by

$$\chi(\hat{\mathbf{r}},t) = -(\hat{\mathbf{r}} - \mathbf{r}_0)\hat{\mathbf{A}}_\perp(\mathbf{r}_0,t) \tag{C.6}$$

This transformation privileges the position of the nucleus r_0. It leads to the Göppert-Mayer potentials

$$\Phi'(\hat{\mathbf{r}},t) = \Phi_{\text{coul}}(\hat{\mathbf{r}}) - (\hat{r}-r_0)\frac{\partial}{\partial t}\hat{\mathbf{A}}_\perp(\mathbf{r}_0,t) \tag{C.7}$$

$$\mathbf{A}'(\hat{\mathbf{r}},t) = \mathbf{A}(\hat{\mathbf{r}},t) - \hat{\mathbf{A}}_\perp(\mathbf{r}_0,t) \tag{C.8}$$

recalling that the electric fiel associated with the applied radiation is $\mathbf{E}(\hat{\mathbf{r}},t) = -\partial_t\mathbf{A}(\hat{\mathbf{r}},t)$ and introducing the electric dipole operator of the atom $\hat{\mathbf{d}} = q(\hat{\mathbf{r}}-\mathbf{r}_0)$, the hamiltonian finally becomes the well known *dipolar hamiltonian*

$$\hat{H} = \hat{H}_0 - \hat{\mathbf{d}}\cdot\hat{\mathbf{E}}(\mathbf{r}_0,t) \tag{C.9}$$

where $\hat{H}_0 = (\hat{\mathbf{p}} - q\mathbf{A}'(\hat{\mathbf{r}},t))^2/2m - e\Phi_{\text{coul}}(\hat{\mathbf{r}})$. Now we make the *long wavelentgh approxiamtions*, which consist in consider that the potential that feels the whole atom (electron + nucleous) is the same that feels the nucleus, i.e, the wavelength of light is much bigger than the size of the atom. This enables us to replace $\hat{\mathbf{A}}'_\perp(\mathbf{r},t)$ by $\hat{\mathbf{A}}'_\perp(\mathbf{r}_0,t)$ which from C.8 is 0. Leaving the free hamiltonian as

$$\hat{H}_0 = \hat{\mathbf{p}}^2/2m - e\Phi_{\text{coul}}(\hat{\mathbf{r}}) \tag{C.10}$$

Jaynes Cummings Model We need the quantum expression of the electric field and of the dipole moment. The electric field for a single mode field at point $\mathbf{r}_0$ is given by

$$\hat{\mathbf{E}}(\mathbf{r}_0,t) = i\left(\frac{\hbar\omega_a}{2\epsilon_0 V}\right)\mathbf{e}\left[\hat{a}e^{i\mathbf{k}\mathbf{r}_0 - i\omega_a t} - \hat{a}^\dagger e^{-i\mathbf{k}\mathbf{r}_0 + i\omega_a t}\right] \tag{C.11}$$

where $\mathbf{e}$ is the polarization unit vector. Under the long wavelength approximation $|\mathbf{k}\mathbf{r}_0| \ll 1$ we can replace

$$\hat{\mathbf{E}}(\mathbf{r}_0,t) \approx \hat{\mathbf{E}}(t) = i\left(\frac{\hbar\omega_a}{2\epsilon_0 V}\right)\mathbf{e}\left[\hat{a}e^{-i\omega_a t} - \hat{a}^\dagger e^{i\omega_a t}\right] \tag{C.12}$$

which in the Schodinger picture is

$$\hat{\mathbf{E}} = i\mathcal{E}\mathbf{e}\left(\hat{a} - \hat{a}^\dagger\right) \tag{C.13}$$

with $\mathcal{E} = (\hbar\omega/2\epsilon_0 V)^{1/2}$.

For the dipole moment we have to define the excited $|e\rangle$ and ground $|g\rangle$ states of the atom and the atomic transition operators $\sigma^\dagger = |e\rangle\langle g|$ and $\sigma = |g\rangle\langle e|$ which can change the state to the excited or ground state

$$\sigma^\dagger|g\rangle = |e\rangle\,, \quad \sigma|e\rangle = |g\rangle \tag{C.14}$$

and obey the Pauli spin algebra

$$\left[\sigma^\dagger, \sigma\right] = |e\rangle\langle e| - |g\rangle\langle g| = \sigma_z, \quad \left[\sigma_z, \sigma^{(\dagger)}\right] = 2\sigma^{(\dagger)}, \quad \{\sigma^\dagger, \sigma\} = \mathbb{1}_{\text{at}} \tag{C.15}$$

where $\mathbb{1}_{\text{at}} = |e\rangle\langle e| + |g\rangle\langle g|$ is the identity in the atomic Hilbert space. We use the later for the expresion of the dipolar momentum

$$\mathbf{d} = \mathbb{1}_{\text{at}}\mathbf{d}\mathbb{1}_{\text{at}} = d(\sigma^\dagger + \sigma) \tag{C.16}$$

where $d = \langle e|\,\mathbf{d}\,|g\rangle = \langle g|\,\mathbf{d}\,|e\rangle$ and $\langle e|\,\mathbf{d}\,|e\rangle = \langle g|\,\mathbf{d}\,|g\rangle = 0$ because the dipolar momentum only connects states of different parity. By substituting in C.9 we finally get the hamiltonian

$$\hat{H} = \omega_a \hat{a}^\dagger \hat{a} + \omega_\sigma \sigma^\dagger \sigma + g\left(\hat{a}^\dagger + \hat{a}\right)\left(\sigma + \sigma^\dagger\right) \tag{C.17}$$

which is called the Rabi Hamiltonian. In the interacting part, we have four different terms that represent four different processes: $\sigma^\dagger \hat{a}$, absorption of a photon and excitation of the atom, $\sigma \hat{a}^\dagger$, creation of a photon and desexcitation of the atom, $\sigma^\dagger \hat{a}^\dagger$, emission of a photon and excitation of the atom, $\sigma \hat{a}$, destruction of a photon and desexcitation of the atom. In contrast to the first two, the last two do not conserve energy separately. Moreover, if $g, |\Delta| \ll \omega_a, \omega_\sigma$ where $\Delta = \omega_a - \omega_\sigma$ they vary much more rapidly, and integrating the time-dependent Schrödinger equation they will have denominator containing $\omega_a + \omega_\sigma$ instead of $\omega_a - \omega_\sigma$. We neglect these terms under the rotating wave approximation (RWA) which finally leads to the Jaynes-Cummings hamiltonian

$$\hat{H}^{JC} = \omega_a \hat{a}^\dagger \hat{a} + \omega_\sigma \sigma^\dagger \sigma + g\left(\hat{a}^\dagger \sigma + \hat{a}\sigma^\dagger\right) \tag{C.18}$$

The eigenstates of this hamiltonian are called the *dressed states*. The interaction term in $\hat{H}^{JC}$ causes only transitions of the type

$$|\psi_{1n}\rangle = |e\rangle\,|n\rangle \leftrightarrow |\psi_{2n}\rangle = |g\rangle\,|n+1\rangle \tag{C.19}$$

which are sometimes referred as the *bare states* of the JC model and obviously $\langle\psi_{1n}|\psi_{2n}\rangle = 0$. Using this basis we can obtain the matrix $H_{ij}^{(n)} = \langle\psi_{in}|\,\hat{H}^{JC}\,|\psi_{jn}\rangle$. For a given n the energy eigenvalues of this matrix are

$$E_\pm(n) = \left(n + \frac{1}{2}\right)\omega_a \pm \Omega_n(\Delta) \tag{C.20}$$

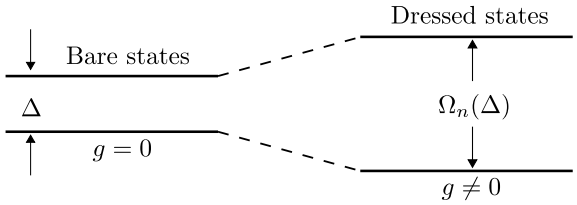

Fig. C.1: Energy-level splitting due to the interaction of the atom with a quantized field. The split levels on the right are the energy levels of the dressed states.

where

$$\Omega_n(\Delta) = \left[\Delta^2 + 4g^2(n+1)\right]^{1/2} \tag{C.21}$$

the eigenstates $|n, \pm\rangle$ asociated with this eigenvalues are given by

$$|n, +\rangle = \cos(\Phi_n/2)\,|\psi_{1n}\rangle + \sin(\Phi_n/2)\,|\psi_{2n}\rangle \tag{C.22}$$

$$|n, -\rangle = -\sin(\Phi_n/2)\,|\psi_{1n}\rangle + \cos(\Phi_n/2)\,|\psi_{2n}\rangle \tag{C.23}$$

where the angle Φ_n is defined through

$$\Phi_n = \tan^{-1}\left(\frac{\Omega_n(0)}{\Delta}\right) \tag{C.24}$$

The states $|n, \pm\rangle$ are called the dressed states. As we can see in Fig. C while the energy difference of the bare states is Δ, for the dressed states increases to $\Omega_n(\Delta)$, which is larger for larger g or higher number of excitation, n.

D. EQUATIONS OF MOTION FOR THE CORRELATORS.

In this appendix, we derive the system equations of motion in the case of a one-dimensional array of single atom lasers. They can be trivially extended to higher dimensions.

The most general operator in the system reads $\langle O\rangle = \left\langle \Pi_k p_k^{\dagger m_k} p_k^{n_k} \Pi_j \sigma_j^{\dagger \mu_j} \sigma_j^{\nu_j} \right\rangle$. From the master equation in the main text, we obtain the equations of motion for the set of relevant operators by means of the general relation $\partial_t \langle O\rangle = \mathrm{Tr}\left\{(\right\} O \partial_t \rho)$ as

$$\partial_t \left\langle \Pi_k p_k^{\dagger m_k} p_k^{n_k} \Pi_j \sigma_j^{\dagger \mu_j} \sigma_j^{\nu_j} \right\rangle = \sum_{\bar{m}_1,\bar{n}_1,\ldots\bar{\mu}_1,\bar{\nu}_1\ldots} R_{\substack{m_1,n_1,\ldots\mu_1,\nu_1\ldots \\ \bar{m}_1,\bar{n}_1,\ldots\bar{\mu}_1,\bar{\nu}_1\ldots}} \left\langle \Pi_k p_k^{\dagger \bar{m}_k} p_k^{\bar{n}_k} \Pi_j \sigma_j^{\dagger \bar{\mu}_j} \sigma_j^{\bar{\nu}_j} \right\rangle . \quad \text{(D.1)}$$

The diagonal elements in R, involving all modes and emitters, are given by [175]:

$$\begin{aligned} R_{\substack{m_1,n_1,\ldots\mu_1,\nu_1\ldots \\ m_1,n_1,\ldots\mu_1,\nu_1\ldots}} &= \quad \text{(D.2)} \\ \sum_k [i\omega_k(m_k - n_k) - \frac{\gamma_a}{2}(m_k + n_k)] & \\ + \sum_j [i\omega_\sigma(\mu_j - \nu_j) - \frac{\gamma_\sigma + P_\sigma}{2}(\mu_j + \nu_j) - \frac{\gamma_\phi}{2}(\mu_j - \nu_j)^2] & . \end{aligned}$$

We have included in these elements the effect of pure dephasing at a rate γ_ϕ, added to the master equations through the Lindblad term $\gamma_\phi \mathcal{L}_{\sigma_j^\dagger \sigma_j}(\rho)$. This only results in the increase of the total decoherence rate into $\Gamma = \gamma_a + P_\sigma + \gamma_\sigma + \gamma_\phi$ [176]. Next, the incoherent pumping of emitter j affects only elements concerning such emitter so that for all j:

$$R_{\substack{\ldots\mu_j,\nu_j\ldots \\ \ldots\mu_j,\nu_j\ldots}} = P_\sigma \mu_j \nu_j \, . \quad \text{(D.3)}$$

Finally, the coupling between mode k and emitter j, provides the elements:

$$R_{\substack{m_k,n_k,\mu_j,\nu_j \\ m_k-1,n_k,1-\mu_j,\nu_j}} = iG_{kj}m_k(1-\mu_j)\,, \tag{D.4a}$$

$$R_{\substack{m_k,n_k,\mu_j,\nu_j \\ m_k,n_k-1,\mu_j,1-\nu_j}} = -iG^*_{kj}n_k(1-\nu_j)\,, \tag{D.4b}$$

$$R_{\substack{m_k,n_k,\mu_j,\nu_j \\ m_k+1,n_k,1-\mu_j,\nu_j}} = iG^*_{kj}\mu_j\,, \tag{D.4c}$$

$$R_{\substack{m_k,n_k,\mu_j,\nu_j \\ m_k,n_k+1,\mu_j,1-\nu_j}} = -iG_{kj}\nu_j \tag{D.4d}$$

$$R_{\substack{m_k,n_k,\mu_j,\nu_j \\ m_k+1,n_k,\mu_j,1-\nu_j}} = -2iG^*_{kj}\mu_j(1-\nu_j)\,, \tag{D.4e}$$

$$R_{\substack{m_k,n_k,\mu_j,\nu_j \\ m_k,n_k+1,1-\mu_j,\nu_j}} = 2iG_{kj}\nu_j(1-\mu_j)\,, \tag{D.4f}$$

and zero everywhere else.

With these general rules, we can write the equations for the main correlators of interest, starting with the populations of the modes, $n_k = \left\langle p_k^\dagger p_k \right\rangle$ and emitters $n_j = \left\langle \sigma_j^\dagger \sigma_j \right\rangle$:

$$\partial_t n_j = -(P_\sigma + \gamma_\sigma)n_j + P_\sigma - 2\sum_k \Im[G^*_{kj}\left\langle p_k^\dagger \sigma_j \right\rangle]\,, \tag{D.5a}$$

$$\partial_t n_k = -\gamma_a n_k + 2\sum_j \Im[G^*_{kj}\left\langle p_k^\dagger \sigma_j \right\rangle]\,, \tag{D.5b}$$

$$\begin{aligned}\partial_t \left\langle p_k^\dagger \sigma_j \right\rangle &= -[\frac{\Gamma}{2} + i(\omega_\sigma - \omega_k)]\left\langle p_k^\dagger \sigma_j \right\rangle \\ &+ iG_{kj}[n_j - n_k + 2\left\langle p_k^\dagger p_k \sigma_j^\dagger \sigma_j \right\rangle] \\ &+ \sum_{l\neq j} iG_{kl}\left\langle \sigma_l^\dagger \sigma_j \right\rangle + \sum_{q\neq k}(-iG_{ql})\left\langle p_k^\dagger p_q \right\rangle \\ &+ \sum_{q\neq k} 2iG_{qj}\left\langle p_k^\dagger p_q \sigma_j^\dagger \sigma_j \right\rangle\,.\end{aligned} \tag{D.5c}$$

The equations for the correlators that represent the indirect coupling between

different emitters or Bloch modes are:

$$\begin{aligned}
\partial_t \left\langle \sigma_l^\dagger \sigma_j \right\rangle &= -(P_\sigma + \gamma_\sigma) \left\langle \sigma_l^\dagger \sigma_j \right\rangle \\
&+ \sum_k i[G_{kl}^* \left\langle p_k^\dagger \sigma_j \right\rangle - G_{kj} \left\langle p_k \sigma_l^\dagger \right\rangle] \\
&+ \sum_k 2i[G_{kj} \left\langle p_k \sigma_l^\dagger \sigma_j^\dagger \sigma_j \right\rangle - G_{kl}^* \left\langle p_k^\dagger \sigma_l^\dagger \sigma_l \sigma_j \right\rangle] , \qquad \text{(D.6a)} \\
\partial_t \left\langle p_k^\dagger p_q \right\rangle &= -[\gamma_a - i(\omega_k - \omega_q)] \left\langle p_k^\dagger p_q \right\rangle \\
&+ \sum_j i[G_{kj} \left\langle p_q \sigma_j^\dagger \right\rangle - G_{qj}^* \left\langle p_k^\dagger \sigma_j \right\rangle] . \qquad \text{(D.6b)}
\end{aligned}$$

Within the formal scheme of the Cluster-Expansion Method, Eq. (D.6a) is of the same order as the Bloch-mode populations n_k. This is owed to the dominant Jaynes-Cummings interaction in the system, which can be used to establish a formal equivalence between an electronic transition and photon creation or absorption [64]. In the thermal and lasing regimes investigated in the main text, the influence of these correlations is small and, therefore, neglected in order to keep the formal solution of the equations as simple as possible.

Finally, the intensity-intensity correlations are given by:

$$\begin{aligned}
\partial_t \left\langle p_k^\dagger p_k \sigma_l^\dagger \sigma_l \right\rangle &= -(\gamma_a + P_\sigma + \gamma_\sigma) \left\langle p_k^\dagger p_k \sigma_l^\dagger \sigma_l \right\rangle + P_\sigma n_k \\
&+ i(G_{kl}^* \left\langle p_k^\dagger p_k^\dagger p_k \sigma_l \right\rangle - G_{kl} \left\langle p_k^\dagger p_k p_k \sigma_l^\dagger \right\rangle) \\
&+ i \sum_{q \neq k} (G_{ql}^* \left\langle p_q^\dagger p_k^\dagger p_k \sigma_l \right\rangle - G_{ql} \left\langle p_q^\dagger p_k p_k \sigma_l^\dagger \right\rangle) \\
&+ i \sum_{j \neq l} (G_{kj} \left\langle p_k \sigma_l^\dagger \sigma_l \sigma_j^\dagger \right\rangle - G_{kj}^* \left\langle p_k^\dagger \sigma_j \sigma_l^\dagger \sigma_l \right\rangle) . \qquad \text{(D.7)}
\end{aligned}$$

E. ESTIMATES FOR THE FIELD CORRELATIONS IN ONE DIMENSION IN THE LIMIT $N \to \infty$

For one dimension, $m = 1$, the momentum distribution in the stationary state reads,

$$n_k = \frac{\kappa_\sigma \Gamma}{4} \frac{n_\sigma}{(\delta/2)^2 + \Delta_k^2}, \tag{E.1}$$

which is a Lorentzian in the detunings $\Delta_k = \Delta - 2J\cos k$, and for $N \to \infty$ the field correlations read,

$$\mathcal{C}(x) = \frac{1}{n_a 2\pi} \int_{-\pi}^{\pi} dk e^{-ixk} n_k \,. \tag{E.2}$$

With n_k a real and even function of k, it is obvious that $\mathcal{C}(x)$ is also real and even as a function of the distance x. Therefore in what follows we consider only the case $x \geqslant 0$. Up to the prefactor $\frac{\kappa_\sigma \Gamma n_\sigma}{4 n_a J^2}$, and bearing in mind that x takes only integer values, the correlations are obtained by calculating a Fourier transform of the form

$$C_n = \frac{1}{2\pi} \int_{-\pi}^{\pi} \frac{e^{ikn}}{(2\cos k - \widetilde{\Delta})^2 + \widetilde{\delta}^2} \, dk, \quad n = 0, 1 \ldots \tag{E.3}$$

where the parameters $\widetilde{\Delta}$ and $\widetilde{\delta}$ are $\widetilde{\Delta} = \Delta/J$ and $\widetilde{\delta} = \delta/(2J)$. One rearranges the expression under the integral as

$$\frac{1}{(2\cos k - \widetilde{\Delta})^2 + \widetilde{\delta}^2} = \frac{1}{2i\widetilde{\delta}} \frac{1}{2\cos k - \widetilde{\Delta} - i\widetilde{\delta}} + \text{c.c.}\,, \tag{E.4}$$

so that one has to compute

$$C_n = \frac{1}{4\pi i \widetilde{\delta}} \int_{-\pi}^{\pi} \frac{e^{ikn}}{2\cos k - u} \, dk + \text{c.c.}\,, \tag{E.5}$$

where u denotes the complex quantity $u = \widetilde{\Delta} + i\widetilde{\delta} = J^{-1}(\Delta + i\delta/2)$. This integral is solved by introducing the new variable $z = e^{ik}$, which runs on

the unit circle $\mathcal{C}_1$,

$$C_n = \frac{-1}{4\pi\delta} \int_{\mathcal{C}_1} \frac{z^n}{z^2 - u\, z + 1}\, dz + \text{c.c.}\,. \tag{E.6}$$

The poles of the integrand are the roots of the denominator $\zeta_{1,2}$, and satisfy $\zeta_1 + \zeta_2 = u$ and $\zeta_1\, \zeta_2 = 1$. There are two possibilities, either (i) $|\zeta_1| < 1 < |\zeta_2|$, or (ii) $|\zeta_1| = 1 = |\zeta_2|$. Representing the roots as $\zeta_2 = e^{\lambda} e^{iq}$ and $\zeta_1 = e^{-\lambda} e^{-iq}$, case (i) amounts to $\lambda > 0$ and ζ_1 lying inside the unit circle. The residue theorem then gives

$$C_n = \frac{i}{2\widetilde{\delta}}\, \frac{1}{\zeta_2 - \zeta_1}\, \zeta_1^n + \text{c.c.}\,. \tag{E.7}$$

This shows that the correlations oscillate along the chain with a wave number q and decay exponentially with the inverse decay length λ.

Case (ii) corresponds to $\lambda = 0$, when both roots are found on $\mathcal{C}_1$. This takes place when $u = \zeta_1 + \zeta_2 = 2\cos q$ i.e. u is real and belongs to the interval $[-2, 2]$. With poles on the integration path the integral is divergent. Still, it makes sense to consider this as a limit case, with u approaching the segment $[-2, 2]$ of the real axis. Then ζ_1 approaches the unit circle from within, and the correlation length $1/\lambda$ goes to infinity. The system becomes critical. The requirements on the system parameters for achieving criticality are $\delta \to 0$ and $|\Delta| \leqslant 2J$. It also follows that q is the momentum of the resonant Bloch mode.

It is straightforward to relate the quantities λ and q, to the system parameters but the expressions are cumbersome. Some qualitative features are easily obtained though, and they describe different regimes of correlation behaviour.

A first situation is encountered when u lies in the complex plane far away from the critical interval $[-2, 2]$. For $\widetilde{\Delta}$ and $\widetilde{\delta}$ large, this corresponds to small J-values, since $\widetilde{\Delta} \propto J^{-1}$ and $\widetilde{\delta} \propto J^{-1}$ In this case λ is large and in the relation $\zeta_1 + \zeta_2 = u$ the small root ζ_1 becomes negligible. It follows that $\lambda = \ln|\zeta_2| \simeq \ln|u| \propto -\ln J$.

A completely different behavior is seen when u is close to the segment $[-2, 2]$. In this regime J is large to make $\widetilde{\delta}$ small. Also, Δ, J are of the same magnitude and obey $|\Delta| \leqslant 2J$, to keep $\widetilde{\Delta}$ within the limit of the interval. In this case $\lambda \simeq 0$, both roots are close to the unit circle. Therefore both contribute to the sum, and one can write

$$\frac{1}{2} u = \frac{1}{2}(\widetilde{\Delta} + i\widetilde{\delta}) = \cosh\lambda \cos q + i \sinh\lambda \sin q\,. \tag{E.8}$$

With λ small, one has $\cosh\lambda \simeq 1$ and $\sinh\lambda \simeq \lambda$ and by identifying the real and imaginary parts, it follows that $\cos q = \widetilde{\Delta}/2 = \Delta/(2J)$ and

$$\lambda = \frac{\widetilde{\delta}}{2\sin q} = \frac{\delta/2}{\sqrt{4J^2-\Delta^2}} = \sqrt{\frac{g^2\Gamma}{\gamma_a(4J^2-\Delta^2)}\left[\frac{\gamma_a\Gamma}{4g^2}-(2n_\sigma-1)\right]}\,. \tag{E.9}$$

With Δ of the same order as J, one obtains $\lambda \propto J^{-1}$.

The above result holds for $\widetilde{\Delta}$ not too close to the endpoints of the critical interval, where $\sin q$ becomes small and division by it gives rise to large values of λ. This is seen in the final expression for λ, in which Δ approaching $2J$ leads to a singularity. Therefore this case requires a separate, more careful consideration, since now q becomes a small quantity, too. Expanding up to the second order in terms of the small arguments, Eq. (E.8) becomes

$$\frac{1}{2}(\widetilde{\Delta}+i\widetilde{\delta}) \simeq 1+\frac{1}{2}\lambda^2-\frac{1}{2}q^2+i\lambda\, q\,. \tag{E.10}$$

To keep the discussion simple we discuss the case $\Delta = 2J$, or $\widetilde{\Delta} = 2$. Actually this illustrates the more general situation in which $1-\widetilde{\Delta}/2$ is a small quantity of a higher than second order. Then, from Eq. (E.10) we find $\lambda = q$ and $\lambda^2 = \widetilde{\delta}/2 = \delta/(4J)$. More precisely

$$\lambda = \left\{\frac{g^2\Gamma}{4\gamma_a J^2}\left[\frac{\gamma_a\Gamma}{4g^2}-(2n_\sigma-1)\right]\right\}^{1/4}\,. \tag{E.11}$$

Note that now $\lambda \propto J^{-1/2}$.

Examples for the fits

In this section we provide some examples for the fits of functions $f(x) = [c_1\cos(\nu x)+c_2\sin(\nu x)]\exp(-\lambda x)$ to the normalized correlations $\mathcal{C}(x)$. These examples are shown in Fig. E.1 and illustrate the excellent quality of the fits. Only for $J \ll g$ the fitting procedure is more fragile as correlations decay very fast and are thus indistinguishable from zero for most values of x.

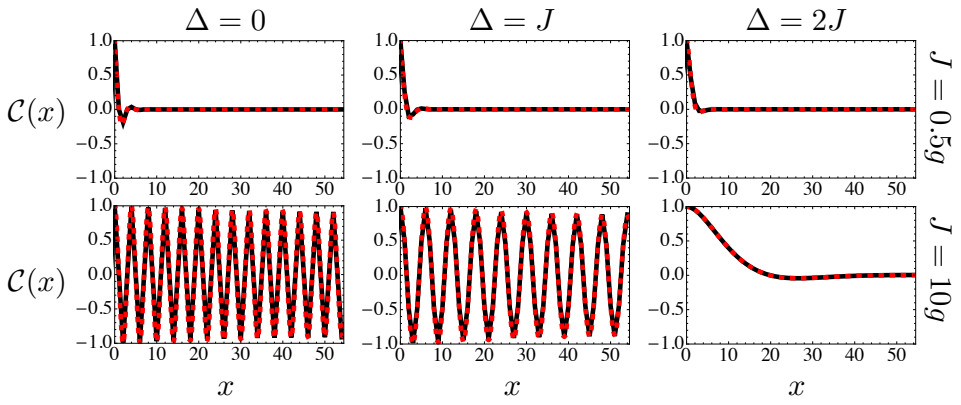

Fig. E.1: Examples for fits of functions $f(x) = [c_1 \cos(\nu x) + c_2 \sin(\nu x)] \exp(-\lambda x)$ to the normalized correlations $\mathcal{C}(x)$ for $N = 108$ and the parameters Δ and J given in the labels of the columns and rows. Other parameters are $\gamma_a = 0.1g$, $\gamma_\sigma = 0.01g$, $P_\sigma = 5g$.

F. FIELD PROPAGATION INSIDE THE CAVITY. PARAXIAL APPROXIMATION

We follow the usual derivation for the propagation of the field inside the cavity by considering that the effect of diffraction during a cavity roundtrip is small and by making use of the slowly varying envelope approximation (see e.g. [177]).

If k_{L} and ω_{L} are the wave number and angular frequency of the field $E(z,\mathbf{r},t)$ with complex amplitude $A_+(z,\mathbf{r},t)$ ($A_-(z,\mathbf{r},t)$) propagating in the positive (negative) z direction, it is useful to consider the representation of the field,

$$E(z,\mathbf{r},t) = i\mathcal{V}\left(A_+(z,\mathbf{r},t)\,e^{ik_{\mathrm{L}}z} + A_-(z,\mathbf{r},t)\,e^{-ik_{\mathrm{L}}z}\right)e^{-i\omega_{\mathrm{L}}t} + \text{c.c.}, \quad \text{(F.1)}$$

which satisfies the Maxwell equations without free charges and currents, that is,

$$\left(\nabla^2 - \frac{1}{c^2}\partial_t\right)E(z,\mathbf{r},t) = 0 \quad \text{(F.2)}$$

After replacing, it is assumed that the complex amplitude $A_\pm$ only varies slowly with z and t compared with the wavelength and period respectively,

$$\left|\partial_z^2 A_\pm\right| \ll |k_{\mathrm{L}}\partial_z A_\pm| \qquad \left|\partial_t^2 A_\pm\right| \ll |\omega_{\mathrm{L}}\partial_t A_\pm| \quad \text{(F.3)}$$

which is called the *slowly varying envelope approximation* (SVEA). The final equations are

$$\left(\pm\partial_z + \frac{1}{c}\partial_t\right)A_\pm = \frac{i}{2k_{\mathrm{L}}}\nabla_\perp^2 A_\pm \quad \text{(F.4)}$$

where $\nabla_\perp^2 = \partial_x^2 + \partial_y^2$ acts in the perpendicular plane. By solving this equation we find that in order to propagate the field a distance d we have to apply the operator $\mathcal{U}_L = e^{id\nabla_\perp^2/2k_{\mathrm{L}}}$ so

$$A_\pm(d,\mathbf{r},t) = \mathcal{U}_L A_\pm(0,\mathbf{r},t-d/c) \quad \text{(F.5)}$$

G. DISCRETE MODEL BASED ON AN ARRAY OF WEAKLY-COUPLED MICRO-MIRRORS.

In this Appendix we propose an alternative of experimental realization for the optomechanical model, proposed in this case for the linear coupling model. This is not membrane like but an array of weakly coupled mirrors, see Fig. G.1, whose continuous limit recovers the linear coupling model. In the following we show this in detail, and provide a numerical analysis of how many micro-mirrors are needed to see the transverse patterns that we have predicted.

We first describe the displacement field in terms of the displacement $\{q_{\mathbf{j}}\}_{\mathbf{j}\in\mathbb{N}^2}$ of the micro-mirrors which form it—labelled by a double index $\mathbf{j}=(j_x,j_y)$ in a 2D configuration—, as $Q(\mathbf{r},t)=\sum_{\mathbf{j}} q_{\mathbf{j}}(t)w_{\mathbf{j}}(\mathbf{r})$, where $w_{\mathbf{j}}(\mathbf{r})$ is a function which equals 1 when $\mathbf{r}$ is on the surface of micro-mirror $\mathbf{j}$ and is 0 otherwise (in the following we assume for simplicity that the micro-mirrors are much larger than the separation between them, that is, $a\gg b$ in Fig. G.1). Each of these displacements satisfies the equation of motion of a damped and forced harmonic oscillator:

$$\ddot{q}_{\mathbf{j}}+\gamma_{\mathrm{m}}\dot{q}_{\mathbf{j}}+\Omega_{\mathrm{m}}^2 q_{\mathbf{j}}=F_{\mathbf{j}}/m, \tag{G.1}$$

where γ_{m}, Ω_{m} and m are, respectively, the damping rate, oscillation frequency, and mass of the micro-mirrors. The force acting on mirror $\mathbf{j}$ has two contributions, $F_{\mathbf{j}}=F_{\mathbf{j}}^{(\mathrm{RP})}+F_{\mathbf{j}}^{(\perp)}$, coming from the radiation pressure effected by the cavity field and the coupling to the neighbouring mirrors, respectively. The first contribution is readily obtained by integrating the radiation pressure[1] over the surface $\mathcal{S}_{\mathbf{j}}$ of the corresponding micro-mirror

$$F_{\mathbf{j}}^{(\mathrm{RP})}=\frac{2\hbar k_{\mathrm{c}}}{t_{\mathrm{c}}}\int_{\mathcal{S}_{\mathbf{j}}}\mathrm{d}^2\mathbf{r}\,|A(\mathbf{r},t)|^2\,. \tag{G.3a}$$

[1] The expression used for the radiation pressure on the array of mirrors is $P_{\mathrm{rad}}(\mathbf{r},t)=\langle S_+(\mathbf{r},t)\rangle_{z=L}/c$ in therms of the time averaged modulus of the Ponting vector associated to the wave impinging to the array of mirrors $\langle S_+(\mathbf{r},t)\rangle_{z=L}=2\epsilon_0 c\mathcal{V}^2|A(\mathbf{r},t)|^2$ with $\mathcal{V}=\sqrt{\hbar\omega_{\mathrm{c}}/4\varepsilon_0 L}$, where ε_0 is the vacuum permittivity and ω_{c} the cavity frequency.

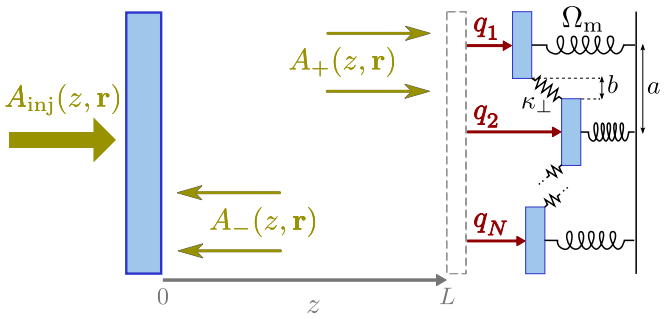

Fig. G.1: Cartoon of the implementation based on a deformable mirror formed by an array of weakly-coupled micro-mirrors.

where $k_{\rm c} = \omega_{\rm c}/c$.

As for the force coming from the coupling to neighbouring mirrors, we assume that it originates from a potential which, in a first approximation, couples neighbours harmonically as $V_{\mathbf{j}}^{\perp} = \kappa_\perp \sum_{\langle \mathbf{l} \rangle_{\mathbf{j}}} (q_{\mathbf{l}} - q_{\mathbf{j}})^2/2$, where $\langle \mathbf{l} \rangle_{\mathbf{j}}$ means that the sum is performed over the neighbours of mirror $\mathbf{j}$; the corresponding force is then obtained as $F_{\mathbf{j}}^{\perp} = -\partial V_{\mathbf{j}}^{\perp}/\partial q_{\mathbf{j}}$, leading to

$$F_{\mathbf{j}}^{(\perp)} = \kappa_\perp \sum_{\langle \mathbf{l} \rangle_{\mathbf{j}}} (q_{\mathbf{l}} - q_{\mathbf{j}}), \tag{G.4}$$

which we note that for a generic micro-mirror not in the boundary of the deformable mirror, it takes the explicit form $F_{\mathbf{j}}^{\perp} = \kappa_\perp (q_{\mathbf{j}+\mathbf{x}} + q_{\mathbf{j}-\mathbf{x}} + q_{\mathbf{j}+\mathbf{y}} + q_{\mathbf{j}-\mathbf{y}} - 4q_{\mathbf{j}})$.

Let us now prove that the the displacement field equation given in the main text, Eq. 7.33(b), is the continuous limit (with the proper normalization) of the evolution equations (G.1) of the individual displacements $q_{\mathbf{j}}(t)$ of the micro-mirrors. In order to do this, we first write the displacements as a function of the field as

$$q_{\mathbf{j}} = \int_{\mathbb{R}^2} \frac{d^2\mathbf{r}}{a^2} Q(\mathbf{r})\, w_{\mathbf{j}}(\mathbf{r}). \tag{G.5}$$

Finally the radiation pressure is:

$$P_{\rm rad}(\mathbf{r},t) = \frac{\hbar k_{\rm c}}{t_{\rm c}} |A(\mathbf{r},t)|^2 \tag{G.2}$$

Next, using

$$\int_{\mathcal{S}_{\mathbf{j}}} \mathrm{d}^2\mathbf{r}\,|A(\mathbf{r},t)|^2 = \int_{\mathbb{R}^2} \mathrm{d}^2\mathbf{r}\,|A(\mathbf{r},t)|^2\, w_{\mathbf{j}}(\mathbf{r}), \tag{G.6a}$$

$$\int_{\mathbb{R}^2} d^2\mathbf{r} Q(\mathbf{r})\, w_{\mathbf{j}\pm\mathbf{x}}(\mathbf{r}) = \int_{\mathbb{R}^2} d^2\mathbf{r} Q(\mathbf{r}\mp a\mathbf{x})\, w_{\mathbf{j}}(\mathbf{r}), \tag{G.6b}$$

and similar in the y direction, the equation of motion of a generic displacement $q_{\mathbf{j}}$ is turned into

$$\begin{aligned}\partial_t^2 Q(\mathbf{r}) + \gamma_{\mathrm{m}}\partial_t Q(\mathbf{r}) + \Omega_{\mathrm{m}}^2 Q(\mathbf{r}) - \Omega_\perp^2[Q(\mathbf{r}+a\mathbf{x}) \\ +Q(\mathbf{r}-a\mathbf{x}) + Q(\mathbf{r}+a\mathbf{y}) + Q(\mathbf{r}-a\mathbf{y}) - 4Q(\mathbf{r})] \\ = \frac{2\hbar k_{\mathrm{c}} a^2}{t_{\mathrm{c}} m}\,|A(\mathbf{r})|^2\,,\end{aligned} \tag{G.7}$$

with $\Omega_\perp = \sqrt{\kappa_\perp/m}$. The last step consists in taking the limit $a \to 0$, but keeping finite the speed at which transverse perturbations propagate in the deformable mirror $v = a\Omega_\perp$ and its surface mass density $\sigma = m/a^2$; in particular, in this limit we can approximate

$$Q(\mathbf{r}\pm a\mathbf{x}) \simeq Q(\mathbf{r}) \pm a\partial_x Q(\mathbf{r}) + a^2\partial_x^2 Q(\mathbf{r})/2, \tag{G.8}$$

and similarly in the y direction, which introduced in the previous equation, leads to the same equation of motion (apart from the constants) for the displacement $Q(\mathbf{r})$ as the one introduced in the main text, Eq. 7.28 , which is

$$\partial_t^2 Q + \gamma_{\mathrm{m}}\partial_t Q + \left(\Omega_{\mathrm{m}}^2 - v^2\nabla_\perp^2\right) Q = \frac{2\hbar k_{\mathrm{c}}}{t_{\mathrm{c}}\sigma}\,|A|^2\,. \tag{G.9}$$

Note that for deriving equation (G.7) we have taken a micro-mirror which is not in the boundary of the deformable mirror, since in the continuous limit the fields are assumed to extend up to infinity.

In order to check the validity of this continuous limit, we have also integrated the underlying discrete model, Eqs.(G.1) instead of (G.9). In particular, let us advance that, using quasiplane-wave (supergaussian) injection with finite width and working in 1D for simplicity, we have found that a discrete model consisting in $N \approx 20$ micro-mirrors with size $a \approx 4l_{\mathrm{c}}$ (a distance surprisingly close to that of the size of solitons, as we are about to see) is enough to observe the localized structures exactly as predicted by the continuous limit; periodic patterns may require a larger number of

micro-mirrors depending on their periodicity, but in any case they should still be well captured with a reasonable number of these (say $N < 100$). Let us provide now more details about these simulations.

As mentioned in the main text, we have numerically simulated the continuous limit by evolving the normalized equations (see subsection 7.3.1) with the usual split-step method (which naturally requires periodic boundary conditions), which at any time step provides an approximation of the fields at certain space points. The same method can be applied to the discrete model, and in particular, let us take M spatial points for the optical field at every mirror, denoting by (j,l) point l of mirror j, so that the field amplitude $A(x)$ is represented by the array $\{A_{j,l}\}_{j=1,2,...,N}^{l=1,2,...,M}$, giving a total of $N \times M$ points. The next step consists in choosing a discretization of the integral appearing in the mechanical equations (G.1); we have found that, for stability purposes, an integration rule of the type

$$\int_{\mathcal{S}_j} \mathrm{d}x \left|A\left(x,t\right)\right|^2 \approx a \sum_{l=0}^{M+1} d_l \left|A_{j,l}\left(t\right)\right|^2,$$

where $A_{j,0} = A_{j-1,M}$ and $A_{j,M+1} = A_{j+1,1}$, is what works best, that is, we use a discrete representation of the integral over mirror j which includes the last point of the previous mirror and the first point of the next one; the weights satisfy the constrain $\sum_{j=0}^{M+1} d_l = 1$, and we have chosen a second order integration rule $\{d_l\}_{l=0,1,...,M+1} = \{1, 23, 24, 24, ..., 24, 23, 1\}/24M$ which seems to provide very good convergence properties. Next, in order to compare with the simulation in the continuous limit, we use the next normalization for the displacements and the optical field ,

$$z_j = \frac{4k_{\mathrm{L}}}{T} q_j, \quad F = \frac{2}{\Omega_{\mathrm{m}}} \sqrt{\frac{2\hbar k_{\mathrm{c}} k_{\mathrm{L}} a}{t_{\mathrm{c}} m T}} A; \tag{G.10}$$

puting everything together, we get the normalized mechanical equations

$$\begin{aligned} & \frac{d^2 z_j}{d\tau^2} + \gamma \frac{dz_j}{d\tau} + \Omega^2 z_j \\ = \;& \rho^2 \Omega^2 \frac{l_{\mathrm{c}}^2}{a^2} \sum_{\langle l \rangle_j} (z_l - z_j) + \Omega^2 \sum_{l=0}^{M+1} d_l \left|F_{j,l}\right|^2, \end{aligned} \tag{G.11}$$

where we have rewritten $\kappa_\perp/m = v^2/a^2$ in terms of the effective rigidity parameter ρ, Eq. 7.31 in the main text, which, together with the detuning,

is the parameter which controls the pattern forming instability in the continuous limit. We remind that $\gamma = \gamma_m/\gamma_c$, $\Omega = \Omega_m/\gamma_m$, and the time has been normalized as $\tau = \gamma_c t$. The normalized equation of the field remains the same as 7.33(a), but with the normalized mechanical field written as $Z(x') = \sum_j z_j w_j(l_c x')$.

In Fig. G.2, we show in solid blue the stationary structures found by numerical resolution of this discrete model in a spatial window $x \in [-40l_c, +40l_c]$ for different number of micro-mirrors N (whose size is then $a = 80l_c/N$), taking $M = 11$ field points per micro-mirror. We have chosen the same parameters as those in the the main text: $\gamma = 0.1$, $\Omega = 10$, $\Delta = -2.2$, and $\rho = 1.13$, and studied the structures for two values of the maximum of the quasi-plane (supergaussian) injection, $E^2 = 2.25$ and 2.7, where the continuous limit predicts the existence of solitons and periodic patterns, respectively. We show in dashed red the structures found in the continuous limit for this same parameters. Note how solitons are well captured even with a fairly small number of micro-mirrors. On the other hand, the restrictions on the number of micro-mirrors needed to see the periodic patterns are a bit tighter, because we need enough to hold such an extended structure, but they still can be observed with not a large number of micro-mirrors.

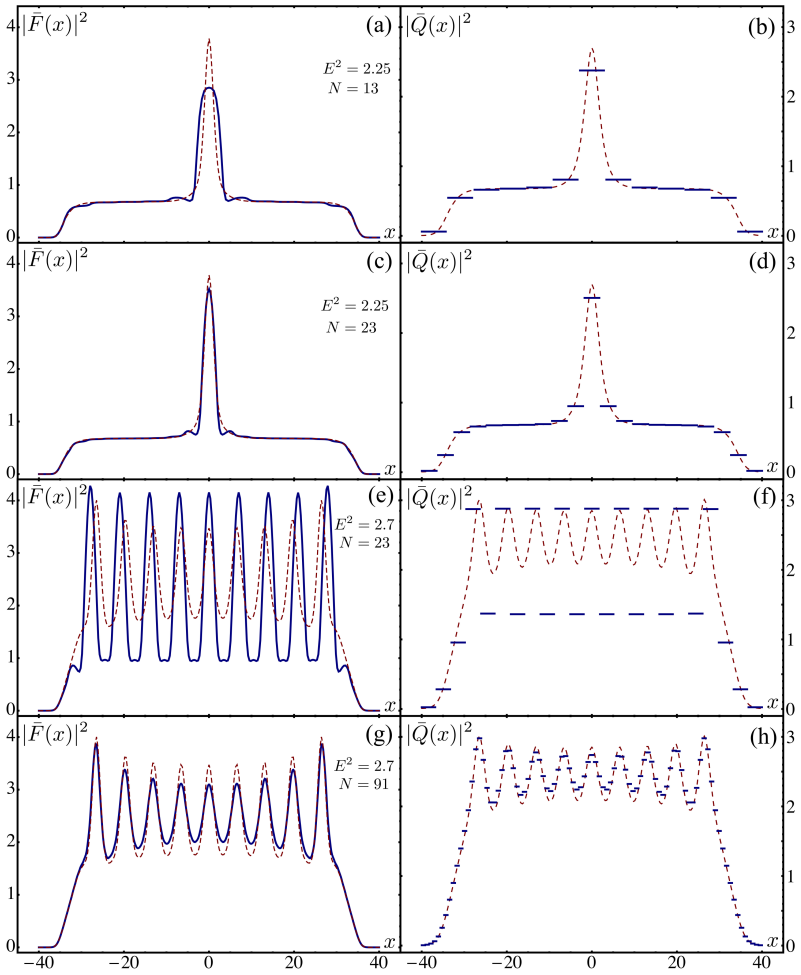

Fig. G.2: Normalized field amplitude (squared) $|F(x)|^2$ and mechanical field $Q(x)$ in the steady-state as a function of the position, for a 1D system of finite size $x \in [-40l_c, 40l_c]$. These have been obtained by numerical resolution of the discrete (solid blue) and continuous (dashed red) models described extensively in the text, and under quasi-plane-wave illumination. In all cases $\gamma = 0.1$, $\Omega = 10$, $\Delta = -2.2$, and $\rho = 1.13$. The injection E^2 has been chosen in the region where solitons (a-d) or periodic patterns (e-h) are expected from the continuous model. For the discrete model we consider N micro-mirrors as specified in the figure, so that their size is $a = 80l_c/N$.

H. SPLIT-STEP METHOD

In this appendix we explain the split step method used for numerical analysis in Chapters 8 and 9. The method treats the linear an the non linear parts separately. The linear step is done in the frequency domain while the nonlinear step is done in the time domain, which makes necessary to Fourier transform back and forth.

Consider the system

$$\partial_t \vec{A} = \mathbf{L}(\nabla^{\mathbf{2}})\vec{A} + \mathbf{N}(\vec{A}) \tag{H.1}$$

where $\vec{A} = \text{col}(F \quad Z \quad Y)$ is our variable vector and $\mathbf{L}(\nabla^{\mathbf{2}})$ and $\mathbf{N}(\vec{A})$ correspond to the linear and non linear parts respectively. The complete step (h) in this method is done according to:

$$\vec{A}(t_0 + h, x) = U_{\mathbf{L}}(h/2)U_{\mathbf{N}}(h)U_{\mathbf{L}}(h/2)\vec{A}(t_0, x) \tag{H.2}$$

The evolution in the linear part is done according to

$$\vec{A}_{\mathbf{L}}(t_0+h/2, x) = U_{\mathbf{L}}(h/2)\vec{A}(t_0, x) = \mathcal{F}^{-1}\left\{e^{\mathbf{L}(-k^2)h/2}\mathcal{F}\left\{\vec{A}(t_0, x)\right\}\right\} \tag{H.3}$$

In the main part of the thesis there have been exposed two models, the linear coupling and the quadratic coupling models. For the non-linear step we have find exact solutions in both cases. The equations and the solutions are as follows:

Linear coupling model

In this case, the equation is conformed by

$$\mathbf{L}(\nabla^{\mathbf{2}}) = \begin{pmatrix} \mathbb{D} & 0 & 0 \\ 0 & 0 & 1 \\ 0 & -\mathbb{L} & -\gamma \end{pmatrix} \qquad \mathbf{N}(\vec{A}) = \begin{pmatrix} iZ^2F + E \\ 0 \\ \Omega_0^2 Z\,|F|^2 \end{pmatrix} \tag{H.4}$$

with $\mathbb{D} = -1 + i\Delta + i\nabla^2$ and $\mathbb{L} = \Omega_0^2\left(1 - \rho^2\nabla^2\right)$. For the nonlinear part we find the exact solutions

$$F_{\mathbf{N}}(t_0 + h) = \left(F_0 - i\frac{E}{Z_0^2}\right)e^{iZ_0^2 h} + i\frac{E}{Z_0^2} \tag{H.5a}$$

$$Z_{\mathbf{N}}(t_0+h) = Z_0 \tag{H.5b}$$

$$\begin{aligned} Y_{\mathbf{N}}(t_0+h) = 2\Omega_0^2 Z_0 \Bigg[\left(|F_0|^2 + \frac{2E^2}{Z_0^4} - \frac{2E}{Z_0^2}\mathrm{Im}(F_0) \right) h + \frac{2E}{Z_0^4}\mathrm{Re}(F_0) \\ + \frac{2E}{Z_0^4} \left(-\mathrm{Re}(F_0)\cos(Z_0^2 h) + \left(\mathrm{Im}(F_0) - \frac{E}{Z_0^2} \right) \sin(Z_0^2 h) \right) \Bigg] + Y_0 \end{aligned} \tag{H.5c}$$

Quadratic coupling model

The equations ar given by

$$\mathbf{L}(\boldsymbol{\nabla^2}) = \begin{pmatrix} \mathbb{D} & 0 & 0 \\ 0 & 0 & 1 \\ 0 & -\mathbb{L} & -\gamma \end{pmatrix} \quad \mathbf{N}(\vec{A}) = \begin{pmatrix} iZ^2F + E \\ 0 \\ \Omega_0^2 Z \left|F\right|^2 \end{pmatrix} \tag{H.6}$$

with $\mathbb{D} = -1 + i\Delta + i\nabla^2$ and $\mathbb{L} = \Omega_0^2 \left(1 - \rho^2\nabla^2\right)$. And for the non-linear part we find the solutions,

$$F_{\mathbf{N}}(t_0+h) = \left(F_0 - i\frac{E}{Z_0^2} \right) e^{iZ_0^2 h} + i\frac{E}{Z_0^2} \tag{H.7a}$$

$$Z_{\mathbf{N}}(t_0+h) = Z_0 \tag{H.7b}$$

$$\begin{aligned} Y_{\mathbf{N}}(t_0+h) = 2\Omega_0^2 Z_0 \Bigg[\left(|F_0|^2 + \frac{2E^2}{Z_0^4} - \frac{2E}{Z_0^2}\mathrm{Im}(F_0) \right) h + \frac{2E}{Z_0^4}\mathrm{Re}(F_0) \\ + \frac{2E}{Z_0^4} \left(-\mathrm{Re}(F_0)\cos(Z_0^2 h) + \left(\mathrm{Im}(F_0) - \frac{E}{Z_0^2} \right) \sin(Z_0^2 h) \right) \Bigg] + Y_0 \end{aligned} \tag{H.7c}$$

I. RESUMEN EN CASTELLANO

I.1 Objetivos

La tesis engloba tres ramas dentro de los campos de la óptica cuántica y no lineal.

En la primera parte, el tema de estudio son las fluctuaciones cuánticas en el Oscilador Óptico Paramétrico (OPO) de tipo II [14]. En esencia, los OPOs son cavidades ópticas que contienen un cristal con una no linealidad de segundo orden. Cuando bombeamos con un laser de frecuencia $2\omega_0$, el OPO es capaz de generar frecuencias ω_s (señal) y ω_i (vago) de tal forma que $\omega_s + \omega_i = 2\omega_0$. Que el dispositivo sea de Tipo II hace referencia a que estos haces tienen polarizaciones ortogonales. En una descripción clásica, la generación de frecuencias requiere que el OPO sea bombeado por encima de un cierto valor umbral [14]; sin embargo, Cuánticamente las parejas de fotones señal-vago pueden ser generadas incluso por debajo de ese umbral, lo cual les confiere propiedades cuánticas muy interesantes [16]. En particular, los OPOs de tipo I, en los cuales señal y vago tienen la misma polarización, mantienen el record de reducción de ruido en cuadraturas (single-mode *squeezing*) [19–23], lo que se manifiesta en el modo degenerado de frecuencia $\omega_s = \omega_i = \omega_0$; consistiendo el *squeezing* en reducir el ruido cuántico en un observable a costa de incrementarlo en su par canónico, preservando así el principio de incertidumbre, lo que permite, por ejemplo, realizar medidas ultraprecisas virtualmente libres de ruido cuántico. Por otro lado, los OPOs de tipo II además de proporcionar *squeezing* en la suma de fases de señal y vago (lo que no resulta detectable puesto que se trata de una cuadratura "mixta" que implica a dos modos de frecuencias y polarizaciones diferentes), tiene reducción completa de ruido en la resta de intensidades, lo cual quiere decir que sus amplitudes están perfectamente correlacionadas y los haces "entrelazados" [34, 38, 39]. Cuando dos sistemas están entrelazados, presentan correlaciones cuánticas no-locales que pueden explotarse para muchas aplicaciones impensables en el dominio clásico. Sin embargo, para la manipulación y detección de estos estados es muy conveniente que los campos

generados estén degenerados en frecuencia (*locking*). Hasta ahora, las técnicas conocidas que consiguen *locking* deterioran los niveles de *squeezing* y entrelazamiento. La primera vez que fue propuesta una técnica de *locking* fue por Fabre y colaboradores en [41]. En esta parte de la tesis, nosotros proponemos una alternativa de conseguir degeneración a frecuencia ω_0. Mostramos que el *locking* puede ser conseguido en el OPO tipo II preservando buenos niveles de entrelazamiento.

En la segunda parte de la tesis nos centramos en el estudio de simuladores cuánticos de la física de sistemas de muchos cuerpos. En particular, nos centramos en el estudio de colecciones (*array*s) de cavidades ópticas, cada una interactuando fuertemente con un emisor de dos niveles [178–180]. Este tipo de sistemas han recibido una atención considerable en los últimos años. Se han descubierto fases coherentes fuertemente correlacionadas [85–87] y se ha discutido sobre analogías con el efecto hall cuántico [88] y con estados cuánticos topológicamente protegidos [89]. En investigaciones anteriores el mecanismo de bombeo utilizado ha sido un bombeo coherente para cada cavidad, con lo que la relación de fase entre los campos de cavidades distantes podía ser atribuida, al menos en parte, a la relación de fase entre los campos coherentes bombeados. En este trabajo mostramos que la coherencia entre cavidades distantes puede construirse espontáneamente, provocada solo por los procesos físicos dentro del *array*. De esta forma nos preguntamos si en estas estructuras se pueden desarrollar superfluidos fuera del equilibrio o condensados de Bose Einstein. Por este motivo, consideramos que el *array* de cavidades esta bombeado sólo de forma incoherente. Para una sola cavidad el sistema se reduce al láser de un solo emisor (one-emitter laser), ampliamente estudiado en [57–62]. En nuestro análisis nos concentramos en las correlaciones en cavidades distantes, típicamente consideradas para investigar efectos de rango lejano y la emergencia de superfluidez. De hecho encontramos correlaciones colectivas cuando las cavidades se encuentran en régimen de emisión láser. Estas correlaciones decaen más rápido que ninguna potencia de la distancia cuando la distancia entre cavidades tiende a infinito para cualquier dimensión del *array*. Como es de esperar, la longitud de correlación asociada aumenta al aumentar el acoplo entre cavidades. También encontramos propiedades intrínsecas del laser, como el típico espectro de fotoluminiscencia, el triplete de Mollow [70, 71], el cual puede ser observado lejos de la resonancia entre emisor y cavidad debido a la aparición de modos fotónicos colectivos.

La tercera parte de la tesis se centra en el estudio de cavidades op-

tomecánicas [11], que son resonadores ópticos (dos espejos enfrentados, por ejemplo) iluminados por un láser, en los que se produce una interacción entre la luz y uno o varios sistemas mecánicos. Estos dispositivos pueden implementarse de varias formas, siendo la más sencilla la que asume que la luz ejerce una presión de radiación que puede modificar la posición de un espejo móvil. El uso de resonadores ópticos permite aumentar en varios órdenes de magnitud la intensidad de la luz en el interior de la cavidad, lo cual conduce a una mejora impresionante de la interacción. Las cavidades optomecánicas han sido implementadas usando diferentes osciladores mecánicos (OM's) como, por ejemplo, resonadores microtoroidales [181] o membranas suspendidas en una cavidad [161]. Desde el punto de vista cuántico, estos dispositivos también pueden proporcionar estados cuánticos de la luz [154] como squeezed o entrelazados, así como enfriamiento del OM (laser *cooling*). El laser *cooling* es una técnica para enfriar el OM hasta su estado fundamental (el de mínima energía), punto de partida para estudiar la transición microscópica-macroscópica de las leyes mecano-cuánticas [182]. El modelo propuesto en esta parte de la tesis, permite la coexistencia de muchos modos tanto mecánicos como ópticos (estamos entonces en presencia de un sistema intrínsecamente multimodo). A través del estudio de la estabilidad del sistema hemos obtenido que pueden coexistir dos soluciones homogéneas (biestabilidad) y que no solo existen inestabilidades temporales, sino que también pueden formarse estructuras espaciales disipativas. Por ejemplo, partiendo de una inyección plana (invariante bajo traslaciones) encontramos patrones hexagonales (que rompen espontáneamente la simetría espacial), y, en la zona de biestabilidad, donde los patrones coexisten con una solución homogénea, encontramos solitones de cavidad.

I.2 Metodología

Para la realización de la tesis se han utilizado numerosos métodos analíticos así como numéricos. Dentro de las técnicas analíticas se han utilizado nociones de mecánica cuántica avanzada, así como descripciones para sistemas físicos con pérdidas, como el de la ecuación máster en forma Limblad [46]. El tratamiento de esta ecuación puede hacerse de diversas formas. En la primera parte, usando la representación positiva P [183], obtenemos una serie de ecuaciones para las variables estocásticas asociadas a los operadores del sistema. En la segunda parte encontramos directamente las ecuaciones para los correladores y luego los rompemos hasta el orden más bajo distinto

de cero utilizando el método de *cluster expansion* [74]. También hemos utilizado los métodos analíticos estándar para estudiar la estabilidad de las soluciones estacionarias [146, 159], como por ejemplo el método de Routh-Hurtwith. Entre los métodos numéricos utilizados se encuentra el método de Fourier simetrizado split-step, el cual trata de separada la evolución temporal en las partes lineal y no-lineal de la ecuación. También, para comprobar la validez de las soluciones en la parte 2 de la tesis hemos utilizado el método de saltos cuánticos (*quantum-jumps*) [68] para encontrar la solución exacta del sistema para una cavidad.

I.3 Conclusiones

En la primera parte, hemos propuesto una forma alternativa de conseguir *locking* de frecuencias en el OPO tipo II que preserve los niveles de entrelazamiento.

En la segunda, hemos estudiado las correlaciones de un *array* de cavidades acopladas, cada una interactuando con un emisor de dos niveles. Y hemos encontrado similitudes con procesos de la física muchos cuerpos.

En la tercera, hemos demostrado la existencia de estructuras disipativas estables, como por ejemplo, patrones y estructuras localizadas, en un modelo multimodo de una cavidad optomecánica.

BIBLIOGRAPHY

[1] Jean-Michel Raimond, M Brune, and Serge Haroche, "Manipulating quantum entanglement with atoms and photons in a cavity," Reviews of Modern Physics **73**, 565 (2001) Back to page 3

[2] Dieter Jaksch and Peter Zoller, "The cold atom hubbard toolbox," Annals of physics **315**, 52–79 (2005) Back to page 3

[3] M. Lewenstein, A. Sanpera, V. Ahufinger, B. Damski, A. Sen, and U. Sen, "Ultracold atomic gases in optical lattices: mimicking condensed matter physics and beyond," Advances in Physics **56**, 243–379 (2007) Back to page 3 or 57

[4] yD Leibfried, R Blatt, C Monroe, and D Wineland, "Quantum dynamics of single trapped ions," Reviews of Modern Physics **75**, 281 (2003) Back to page 3

[5] Ch Schneider, Diego Porras, and Tobias Schaetz, "Experimental quantum simulations of many-body physics with trapped ions," Reports on Progress in Physics **75**, 024401 (2012) Back to page 3

[6] Michel H Devoret, A Wallraff, and JM Martinis, "Superconducting qubits: A short review," arXiv preprint cond-mat/0411174(2004) Back to page 3

[7] JQ You and Franco Nori, "Superconducting circuits and quantum information," arXiv preprint quant-ph/0601121(2006) Back to page 3

[8] Bernhard Urbaszek, Xavier Marie, Thierry Amand, Olivier Krebs, Paul Voisin, Patrick Maletinsky, Alexander Högele, and Atac Imamoglu, "Nuclear spin physics in quantum dots: an optical investigation," Reviews of Modern Physics **85**, 79 (2013) Back to page 3

[9] Klemens Hammerer, Anders S Sørensen, and Eugene S Polzik, "Quantum interface between light and atomic ensembles," Reviews of Modern Physics **82**, 1041 (2010) Back to page 3

[10] Christine A Muschik, Hanna Krauter, Klemens Hammerer, and Eugene S Polzik, "Quantum information at the interface of light with atomic ensembles and micromechanical oscillators," Quantum Information Processing **10**, 839–863 (2011) Back to page 3

[11] M. Aspelmeyer, T.J. Kippenberg, and F. Marquardt, "Cavity optomechanics," arXiv preprint arXiv:1303.0733(2013) Back to page 3, 75, or 157

[12] Tobias J Kippenberg and Kerry J Vahala, "Cavity opto-mechanics," Optics Express **15**, 17172–17205 (2007) Back to page 3

[13] Florian Marquardt and Steven M Girvin, "Optomechanics (a brief review)," arXiv preprint arXiv:0905.0566(2009) Back to page 3

[14] R. W. Boyd, *Nonlinear optics* (Academic press, 2003) Back to page 7 or 155

[15] C. Navarrete-Benlloch, *Contributions to the Quantum Optics of Multimode Optical Parametric Oscillators* (Moliner S.L., 2011) Back to page 11, 21, 23, 24, or 25

[16] P. Meystre, *Nonclassical effects in quantum optics* (American Inst. of Physics, 1991) Back to page 11 or 155

[17] A. Einstein, B. Podolsky, and N. Rosen, "Can quantum-mechanical description of physical reality be considered complete?." Physical review **47**, 777 (1935) Back to page 16, 18, or 21

[18] Daniel F Walls and Gerard J Milburn, *Quantum optics* (Springer Science & Business Media, 2007) Back to page 20, 80, or 84

[19] M. Mehmet, S. Ast, T. Eberle, S. Steinlechner, H. Vahlbruch, and R. Schnabel, "Squeezed light at 1550 nm with a quantum noise reduction of 12.3 db," Opt. Express **19**, 25763–25772 (2011) Back to page 20 or 155

[20] T. Eberle, S. Steinlechner, J. Bauchrowitz, V. Händchen, H. Vahlbruch, M. Mehmet, H. Müller-Ebhardt, and R. Schnabel, "Quantum enhancement of the zero-area sagnac interferometer topology for gravitational wave detection," Phys. Rev. Lett. **104**, 251102 (2010) Back to page 20 or 155

[21] M. Mehmet, H. Vahlbruch, N. Lastzka, K. Danzmann, and R. Schnabel, "Observation of squeezed states with strong photon-number oscillations," Phys. Rev. A **81**, 013814 (2010) Back to page 20 or 155

[22] H. Vahlbruch, M. Mehmet, S. Chelkowski, B. Hage, A. Franzen, N. Lastzka, S. Gossler, K. Danzmann, and R. Schnabel, "Observation of squeezed light with 10-db quantum-noise reduction," Phys. Rev. Lett. **100**, 033602 (2008) Back to page 20 or 155

[23] Y. Takeno, M. Yukawa, H. Yonezawa, and A. Furusawa, "Observation of-9 db quadrature squeezing with improvement of phase stability in homodyne measurement," Optics Express **15**, 4321–4327 (2007) Back to page 20 or 155

[24] M. J. Collett and C. W. Gardiner, "Squeezing of intracavity and traveling-wave light fields produced in parametric amplification," Phys. Rev. A **30**, 1386–1391 (1984) Back to page 20

[25] K. Goda, O. Miyakawa, E. E. Mikhailov, S. Saraf, R. Adhikari, K. McKenzie, R. Ward, S. Vass, A. J. Weinstein, and N. Mavalvala, "A quantum-enhanced prototype gravitational-wave detector," Nature Physics **4**, 472–476 (2008) Back to page 21

[26] H. Vahlbruch, S. Chelkowski, B. Hage, A. Franzen, K. Danzmann, and R. Schnabel, "Demonstration of a squeezed-light-enhanced power- and signal-recycled michelson interferometer," Phys. Rev. Lett. **95**, 211102 (2005) Back to page 21

[27] N. Treps, U. Andersen, B. Buchler, P. K. Lam, A. Maître, H.-A. Bachor, and C. Fabre, "Surpassing the standard quantum limit for optical imaging using nonclassical multimode light," Phys. Rev. Lett. **88**, 203601 (2002) Back to page 21

[28] N. Treps, N. Grosse, W. P. Bowen, C. Fabre, H. Bachor, and P. K. Lam, "A quantum laser pointer," Science **301**, 940–943 (2003) Back to page 21

[29] S. L. Braunstein and P. Van Loock, "Quantum information with continuous variables," Reviews of Modern Physics **77**, 513 (2005) Back to page 21, 43, 45, or 131

[30] C. Weedbrook, S. Pirandola, R. Garcia-Patron, N. J. Cerf, T. C. Ralph, J. H. Shapiro, and S. Lloyd, "Gaussian quantum information," Reviews of Modern Physics **84**, 621 (2012) Back to page 21, 43, 45, or 131

[31] M. D. Reid and P. D. Drummond, "Quantum correlations of phase in nondegenerate parametric oscillation," Phys. Rev. Lett. **60**, 2731–2733 (1988) Back to page 21

[32] M. D. Reid, "Demonstration of the einstein-podolsky-rosen paradox using nondegenerate parametric amplification," Physical Review A **40**, 913 (1989) Back to page 21

[33] P. D. Drummond and M. D. Reid, "Correlations in nondegenerate parametric oscillation. ii. below threshold results," Phys. Rev. A **41**, 3930–3949 (1990) Back to page 21

[34] A. S. Lane, M. D. Reid, and D. F. Walls, "Quantum analysis of intensity fluctuations in the nondegenerate parametric oscillator," Physical Review A **38**, 788 (1988) Back to page 21 or 155

[35] M. D. Reid and P. D. Drummond, "Correlations in nondegenerate parametric oscillation: squeezing in the presence of phase diffusion," Physical Review A **40**, 4493 (1989) Back to page 21

[36] C. Navarrete-Benlloch, E. Roldán, and G. J. de Valcárcel, "Noncritically squeezed light via spontaneous rotational symmetry breaking," Physical review letters **100**, 203601 (2008) Back to page 21, 23, 25, or 78

[37] C. Navarrete-Benlloch, A. Romanelli, E. Roldán, and G. J. de Valcárcel, "Noncritical quadrature squeezing in two-transverse-mode optical parametric oscillators," Physical Review A **81**, 043829 (2010) Back to page 21, 23, or 25

[38] S. Reynaud, C. Fabre, and E. Giacobino, "Quantum fluctuations in a two-mode parametric oscillator," JOSA B **4**, 1520–1524 (1987) Back to page 21 or 155

[39] A. Heidmann, R. J. Horowicz, S. Reynaud, E. Giacobino, C. Fabre, and G. Camy, "Observation of quantum noise reduction on twin laser beams," Physical review letters **59**, 2555 (1987) Back to page 21 or 155

[40] S. Feng and O. Pfister, "Stable nondegenerate optical parametric oscillation at degenerate frequencies in na: Ktp," Journal of Optics B: Quantum and Semiclassical Optics **5**, 262 (2003) Back to page 22

[41] L. Longchambon, J. Laurat, T. Coudreau, and C. Fabre, "Non-linear and quantum optics of a type ii opo containing a birefringent element," The European Physical Journal D-Atomic, Molecular, Optical and Plasma Physics **30**, 287–293 (2004) Back to page 22, 33, or 156

[42] J. Laurat, L. Longchambon, C. Fabre, and T. Coudreau, "Experimental investigation of amplitude and phase quantum correlations in a type ii optical parametric oscillator above threshold: from nondegenerate to degenerate operation," Optics letters **30**, 1177–1179 (2005) Back to page 22 or 33

[43] F. V. Garcia-Ferrer, C. Navarrete-Benlloch, G. J. de Valcárcel, and E. Roldán, "Noncritical quadrature squeezing through spontaneous polarization symmetry breaking," Optics letters **35**, 2194–2196 (2010) Back to page 22

[44] C. Navarrete-Benlloch, E. Roldán, and G. J. de Valcárcel, "Squeezing properties of a two-transverse-mode degenerate optical parametric oscillator with an injected signal," Phys. Rev. A **83**, 043812 (2011) Back to page 23, 25, or 32

[45] C. Navarrete-Benlloch and G. J. de Valcárcel, "Impact of anisotropy on the noncritical squeezing properties of two-transverse-mode optical parametric oscillators," Phys. Rev. A **87**, 065802 (2013) Back to page 23 or 25

[46] C. Gerry and P. Knight, *Introductory quantum optics* (Cambridge university press, 2005) Back to page 24, 127, 133, or 157

[47] P.D. Drummond and C.W. Gardiner, "Generalised p-representations in quantum optics," Journal of Physics A: Mathematical and General **13**, 2353 (1980) Back to page 25

[48] J. Ruiz-Rivas, C. Navarrete-Benlloch, and G.J. de Valcarcel, "Active locking and entanglement in type ii optical parametric oscillators," in preparation Back to page 35

[49] Carlos Navarrete-Benlloch, "An introduction to the formalism of quantum information," arXiv preprint arXiv:1504.05270(2015) Back to page 43, 45, or 131

[50] K. H. Drexhage and E. Wolf, "Progress in optics," Amsterdam, The Netherlands **12**, 163 (1974) Back to page 50

[51] A. Boca, R. Miller, K. M. Birnbaum, A. D. Boozer, J. McKeever, and H. J. Kimble, "Observation of the vacuum rabi spectrum for one trapped atom," Physical review letters **93**, 233603 (2004) Back to page 50

[52] A. Wallraff, D. I. Schuster, A. Blais, L. Frunzio, R. S. Huang, J. Majer, S. Kumar, Steven M. G., and R. J. Schoelkopf, "Strong coupling of a single photon to a superconducting qubit using circuit quantum electrodynamics," Nature **431**, 162–167 (2004) Back to page 50

[53] J. M. Fink, M. Göppl, M. Baur, R. Bianchetti, P. J. Leek, A. Blais, and A. Wallraff, "Climbing the jaynes–cummings ladder and observing its nonlinearity in a cavity qed system," Nature **454**, 315–318 (2008) Back to page 50

[54] J. P. Reithmaier, G. Sęk, A. Löffler, C. Hofmann, S. Kuhn, S. Reitzenstein, L. V. Keldysh, V. D. Kulakovskii, T. L. Reinecke, and A. Forchel, "Strong coupling in a single quantum dot–semiconductor microcavity system," Nature **432**, 197–200 (2004) Back to page 50

[55] Tomoyuki Yoshie, Axel Scherer, J Hendrickson, G Khitrova, HM Gibbs, G Rupper, C Ell, OB Shchekin, and DG Deppe, "Vacuum rabi splitting with a single quantum dot in a photonic crystal nanocavity," Nature **432**, 200–203 (2004) Back to page 50

[56] E. Peter, P. Senellart, D. Martrou, A. Lemaître, J. Hours, J. M. Gérard, and J. Bloch, "Exciton-photon strong-coupling regime for a single quantum dot embedded in a microcavity," Physical review letters **95**, 067401 (2005) Back to page 50

[57] Y. Mu and C. M. Savage, "One-atom lasers," Physical Review A **46**, 5944 (1992) Back to page 51 or 156

[58] J. McKeever, A. Boca, A. D. Boozer, J. R. Buck, and H. J. Kimble, "Experimental realization of a one-atom laser in the regime of strong coupling," Nature **425**, 268 (2003) Back to page 51 or 156

[59] O. Astafiev, K. Inomata, A. O. Niskanen, T. Yamamoto, Yu. A. Pashkin, Y. Nakamura, and J. S. Tsai, "Single artificial-atom lasing," Nature **449**, 588 (2007) Back to page 51 or 156

[60] M. Nomura, N. Kumagai, S. Iwamoto, Y. Ota, and Y. Arakawa, "Laser oscillation in a strongly coupled single-quantum-dot–nanocavity system," Nat. Phys. **6**, 279 (2010) Back to page 51 or 156

[61] E. del Valle and F. P. Laussy, "Regimes of strong light-matter coupling under incoherent excitation," Phys. Rev. A **84**, 043816 (2011) Back to page 51, 54, 56, 62, 67, 69, or 156

[62] P. Gartner, "Two-level laser: Analytical results and the laser transition," Phys. Rev. A **84**, 053804 (2011) Back to page 51 or 156

[63] A. Moelbjerg, P. Kaer, M. Lorke, B. Tromborg, and J. Mørk, "Dynamical properties of nanolasers based on few discrete emitters," IEEE Journal of Quantum Electronics **49**, 945 (2013) Back to page 53 or 54

[64] C. Gies, J. Wiersig, M. Lorke, and F. Jahnke, "Semiconductor model for quantum-dot-based microcavity lasers," Phys. Rev. A **75**, 013803 (2007) Back to page 53, 61, or 139

[65] N.S. Averkiev, M.M. Glazov, and A.N. Poddubny, "Collective modes of quantum dot ensembles in microcavities," Sov. Phys. JETP **135**, 959 (2009) Back to page 54

[66] F.P. Laussy, A. Laucht, E. del Valle, J. J. Finley, and J. M. Villas-Bôas, "Luminescence spectra of quantum dots in microcavities. III. multiple quantum dots," Phys. Rev. B **84**, 195313 (2011) Back to page 54 or 55

[67] A. Auffèves, D. Gerace, S. Portolan, A. Drezet, and M. França Santos, "Few emitters in a cavity: from cooperative emission to individualization," New J. Phys. **13**, 093020 (2011) Back to page 54 or 55

[68] M. B. Plenio and P. L. Knight, "The quantum-jump approach to dissipative dynamics in quantum optics," Reviews of Modern Physics **70**, 101 (1998) Back to page 55 or 158

[69] J. Ruiz-Rivas, E. del Valle, C. Gies, P. Gartner, and M. J. Hartmann, "Spontaneous collective coherence in driven dissipative cavity arrays," Physical Review A **90**, 033808 (2014) Back to page 55

[70] B. R. Mollow, "Power spectrum of light scattered by two-level systems," Phys. Rev. **188**, 1969–1975 (1969) Back to page 55 or 156

[71] E. Del Valle and F. P. Laussy, "Regimes of strong light-matter coupling under incoherent excitation," Physical Review A **84**, 043816 (2011) Back to page 55, 57, or 156

[72] G. Yeoman and G. M. Meyer, "Two-atom laser," Phys. Rev. A **58**, 2518 (1998) Back to page 55

[73] A. N. Poddubny, M. M. Glazov, and N. S. Averkiev, "Nonlinear emission spectra of quantum dots strongly coupled to a photonic mode," Phys. Rev. B **82**, 205330 (2010) Back to page 55

[74] C. Gies, M. Florian, P. Gartner, and F. Jahnke, "The single quantum dot-laser: lasing and strong coupling in the high-excitation regime," Opt. Express **19**, 14370–14388 (2011) Back to page 55 or 158

[75] E. del Valle and F. P. Laussy, "Mollow triplet under incoherent pumping," Phys. Rev. Lett. **105**, 233601 (2010) Back to page 56 or 69

[76] E. Jané, G. Vidal, W. Dür, P. Zoller, and J. I. Cirac, "Simulation of quantum dynamics with quantum optical systems," Quantum Information & Computation **3**, 15–37 (2003) Back to page 57

[77] R. Fazio and H. Van Der Zant, "Quantum phase transitions and vortex dynamics in superconducting networks," Physics Reports **355**, 235–334 (2001) Back to page 57

[78] M. J. Hartmann, F. G. S. L. Brandão, and M. B. Plenio, "Strongly interacting polaritons in coupled arrays of cavities," Nat. Phys. **2**, 849 (2006) Back to page 57

[79] A. D. Greentree, C. Tahan, J. H. Cole, and L. C. L. Hollenberg, "Quantum phase transitions of light," Nat. Phys. **2**, 856 (2006) Back to page 57

[80] D. G. Angelakis, M. F. Santos, and S. Bose, "Photon-blockade-induced mott transitions and XY spin models in coupled cavity arrays," Phys. Rev. A **76**, 031805 (2007) Back to page 57

[81] M. J. Hartmann, F. G.S.L. Brandão, and M. B. Plenio, "Quantum many-body phenomena in coupled cavity arrays," Laser & Photonics Reviews **2**, 527–556 (2008), ISSN 1863-8899 Back to page 58 or 59

[82] A. Tomadin and R. Fazio, "Many-body phenomena in qed-cavity arrays," JOSA B **27**, A130–A136 (2010) Back to page 58

[83] A. A. Houck, H. E. Türeci, and J. Koch, "On-chip quantum simulation with superconducting circuits," Nature Physics **8**, 292–299 (2012) Back to page 58 or 59

[84] I. Carusotto and C. Ciuti, "Quantum fluids of light," Rev. Mod. Phys. **85**, 299–366 (2013) Back to page 58 or 59

[85] I. Carusotto, D. Gerace, H. E. Tureci, S. De Liberato, C. Ciuti, and A. Imamoğu, "Fermionized photons in an array of driven dissipative nonlinear cavities," Phys. Rev. Lett. **103**, 033601 (2009) Back to page 58 or 156

[86] Michael J. Hartmann, "Polariton crystallization in driven arrays of lossy nonlinear resonators," Phys. Rev. Lett. **104**, 113601 (2010) Back to page 58 or 156

[87] F. Nissen, S. Schmidt, M. Biondi, G. Blatter, H. E. Türeci, and J. Keeling, "Nonequilibrium dynamics of coupled qubit-cavity arrays," Phys. Rev. Lett. **108**, 233603 (2012) Back to page 58 or 156

[88] R. O. Umucalılar and I. Carusotto, "Fractional quantum hall states of photons in an array of dissipative coupled cavities," Phys. Rev. Lett. **108**, 206809 (2012) Back to page 58 or 156

[89] C. E. Bardyn and A. İmamoğlu, "Majorana-like modes of light in a one-dimensional array of nonlinear cavities," Phys. Rev. Lett. **109**, 253606 (2012) Back to page 58 or 156

[90] I. Bloch, J. Dalibard, and W. Zwerger, "Many-body physics with ultracold gases," Rev. Mod. Phys. **80**, 885–964 (2008) Back to page 58

[91] S. Diehl, A. Micheli, A. Kantian, B. Kraus, H. P. Bucheler, and P. Zoller, "Quantum states and phases in driven open quantum systems with cold atoms," Nat. Phys. **4**, 878 (2008) Back to page 59

[92] P. Schindler, M. Müller, D. Nigg, J. T. Barreiro, E. A. Martinez, M. Hennrich, T. Monz, S. Diehl, P. Zoller, and R. Blatt, "Quantum simulation of dynamical maps with trapped ions," Nat. Phys. **9**, 361 (2013) Back to page 59

[93] D. Marcos, A. Tomadin, S. Diehl, and P. Rabl, "Photon condensation in circuit quantum electrodynamics by engineered dissipation," New J. Phys. **14**, 055005 (2012) Back to page 59

[94] E. Altman, L. M. Sieberer, L. Chen, S. Diehl, and J. Toner, "Two-dimensional superfluidity of exciton-polaritons requires strong anisotropy," (2013), arxiv:1311.0876 Back to page 59

[95] L. M. Sieberer, S. D. Huber, E. Altman, and S. Diehl, "Dynamical critical phenomena in driven-dissipative systems," Phys. Rev. Lett. **110**, 195301 (2013) Back to page 59

[96] J. Raftery, D. Sadri, S. Schmidt, H. E. Türeci, and A. A. Houck, "Observation of a Dissipation-Induced Classical to Quantum Transition," ArXiv e-prints(2013), arXiv:1312.2963 [quant-ph] Back to page 59

[97] A. Majumdar, A. Rundquist, M. Bajcsy, V. D. Dasika, S. R. Bank, and J. Vuckovic, "Design and analysis of photonic crystal coupled cavity arrays for quantum simulation," Phys. Rev. B **86**, 195312 (2012) Back to page 59

[98] A. Rundquist, A. Majumdar, M. Bajcsy, V. D. Dasika, S. B., and J. Vuckovic, "Photonic crystal coupled cavity arrays for quantum simulation," in *CLEO: 2013* (Optical Society of America, 2013) p. CM4F.7 Back to page 59

[99] M. Abbarchi, A. Amo, V. G. Sala, D. D. Solnyshkov, H. Flayac, L. Ferrier, I. Sagnes, E. Galopin, A. Lemaître, G. Malpuech, and J. Bloch, "Macroscopic quantum self-trapping and josephson oscillations of exciton polaritons," Nat. Phys. **9**, 275 (2013) Back to page 59

[100] G. Lepert, M. Trupke, M. J. Hartmann, M. B. Plenio, and E. A. Hinds, "Arrays of waveguide-coupled optical cavities that interact strongly with atoms," New J. Phys. **13**, 113002 (2011) Back to page 59

[101] I. Carusotto and C. Ciuti, "Quantum fluids of light," Rev. Mod. Phys. **85**, 299–366 (2013) Back to page 59

[102] E. del Valle, F. P. Laussy, and C. Tejedor, "Luminescence spectra of quantum dots in microcavities. II. Fermions," Phys. Rev. B **79**, 235326 (2009) Back to page 60

[103] M. J. Hartmann, "Polariton crystallization in driven arrays of lossy nonlinear resonators," Phys. Rev. Lett. **104**, 113601 (2010) Back to page 60

[104] M. P. A. Fisher, P. B. Weichman, G. Grinstein, and D. S. Fisher, "Boson localization and the superfluid-insulator transition," Physical Review B **40**, 546 (1989) Back to page 61

[105] N. D. Mermin and H. Wagner, Phys. Rev. Lett. **17**, 1133 (1966) Back to page 63

[106] P. C. Hohenberg, Phys. Rev. **158**, 383 (1967) Back to page 63

[107] W. Rudin, *Real and Complex Analysis* (McGraw-Hill, 1987) Back to page 64

[108] F.P. Laussy, E. del Valle, and J.J. Finley, "Universal signatures of lasing in the strong coupling regime," Proc. SPIE **8255**, 82551G (2012) Back to page 67

[109] J.H. Eberly and K. Wódkiewicz, "The time-dependent physical spectrum of light," J. Opt. Soc. Am. **67**, 1252 (1977) Back to page 69

[110] J. H. Eberly, C. V. Kunasz, and K. Wódkiewicz, "Time-dependent spectrum of resonance fluorescence," J. phys. B.: At. Mol. Phys. **13**, 217 (1980) Back to page 69

[111] E. del Valle, A. Gonzalez-Tudela, F. P. Laussy, C. Tejedor, and M. J. Hartmann, "Theory of frequency-filtered and time-resolved n-photon correlations," Phys. Rev. Lett. **109**, 183601 (2012) Back to page 69

[112] E. del Valle and F. P. Laussy, "Mollow triplet," Wolfram Demonstrations Project(2013) Back to page 69

[113] B. R. Mollow, "Power spectrum of light scattered by two-level systems," Phys. Rev. **188**, 1969 (1969) Back to page 69

[114] P. Lebedew, "Untersuchungen über die druckkräfte des lichtes," Annalen der Physik **311**, 433–458 (1901) Back to page 73

[115] E. F. Nichols and G. F. Hull, "A preliminary communication on the pressure of heat and light radiation," Physical Review (Series I) **13**, 307 (1901) Back to page 73

[116] R. Frisch and O. Stern, "Über die magnetische ablenkung von wasserstoffmolekülen und das magnetische moment des protons. i," Zeitschrift für Physik **85**, 4–16 (1933) Back to page 73

[117] R. A. Beth, "Mechanical detection and measurement of the angular momentum of light," Physical Review **50**, 115 (1936) Back to page 73

[118] S. Aldana, C. Bruder, and A. Nunnenkamp, "Equivalence between an optomechanical system and a kerr medium," Physical Review A **88**, 043826 (2013) Back to page 74

[119] A. Dorsel, J. D. McCullen, P. Meystre, E. Vignes, and H. Walther, "Optical bistability and mirror confinement induced by radiation pressure," Phys. Rev. Lett. **51**, 1550–1553 (1983) Back to page 74

[120] P. Meystre, E. M. Wright, J. D. McCullen, and E. Vignes, "Theory of radiation-pressure-driven interferometers," JOSA B **2**, 1830–1840 (1985) Back to page 74

[121] C. Fabre, M. Pinard, S. Bourzeix, A. Heidmann, E. Giacobino, and S. Reynaud, "Quantum-noise reduction using a cavity with a movable mirror," Phys. Rev. A **49**, 1337–1343 (1994) Back to page 75

[122] S. Mancini and P. Tombesi, "Quantum noise reduction by radiation pressure," Phys. Rev. A **49**, 4055–4065 (1994) Back to page 75

[123] K. Jacobs, P. Tombesi, M. J. Collett, and D. F. Walls, "Quantum-nondemolition measurement of photon number using radiation pressure," Phys. Rev. A **49**, 1961–1966 (1994) Back to page 75

[124] M. Pinard, C. Fabre, and A. Heidmann, "Quantum-nondemolition measurement of light by a piezoelectric crystal," Physical Review A **51**, 2443 (1995) Back to page 75

[125] D. WC Brooks, T. Botter, S. Schreppler, T.P. Purdy, N. Brahms, and D.M. Stamper-Kurn, "Non-classical light generated by quantum-noise-driven cavity optomechanics," Nature **488**, 476–480 (2012) Back to page 75

[126] V. Giovannetti, S. Mancini, and P. Tombesi, "Radiation pressure induced einstein-podolsky-rosen paradox," EPL (Europhysics Letters) **54**, 559 (2001) Back to page 75

[127] S. Mancini, V. Giovannetti, D. Vitali, and P. Tombesi, "Entangling macroscopic oscillators exploiting radiation pressure," Physical review letters **88**, 120401 (2002) Back to page 75

[128] I. Wilson-Rae, N. Nooshi, W. Zwerger, and TJ. Kippenberg, "Theory of ground state cooling of a mechanical oscillator using dynamical backaction," Physical Review Letters **99**, 093901 (2007) Back to page 75

[129] F. Marquardt, J.P. Chen, A.A. Clerk, and S.M. Girvin, "Quantum theory of cavity-assisted sideband cooling of mechanical motion," Physical Review Letters **99**, 093902 (2007) Back to page 75

[130] F. Marquardt, A.A. Clerk, and S.M. Girvin, "Quantum theory of optomechanical cooling," Journal of Modern Optics **55**, 3329–3338 (2008) Back to page 75

[131] C. Genes, D. Vitali, P. Tombesi, S. Gigan, and M. Aspelmeyer, "Ground-state cooling of a micromechanical oscillator: Comparing cold damping and cavity-assisted cooling schemes," Physical Review A **77**, 033804 (2008) Back to page 75

[132] L. Zhang and H. Kong, "Self-sustained oscillation and harmonic generation in optomechanical systems with quadratic couplings," Physical Review A **89**, 023847 (2014) Back to page 76

[133] T. Carmon, H. Rokhsari, L. Yang, T. J. Kippenberg, and K. J. Vahala, "Temporal behavior of radiation-pressure-induced vibrations of an optical microcavity phonon mode," Phys. Rev. Lett. **94**, 223902 (2005) Back to page 76

[134] S. Shim, M. Imboden, and P. Mohanty, "Synchronized oscillation in coupled nanomechanical oscillators," Science **316**, 95–99 (2007) Back to page 76

[135] S. Etaki, F. Konschelle, Y. M. Blanter, H. Yamaguchi, and H. S. J. Van Der Zant, "Self-sustained oscillations of a torsional squid resonator induced by lorentz-force back-action," Nature communications **4**, 1803 (2013) Back to page 76

[136] G. Heinrich, M. Ludwig, J. Qian, B. Kubala, and F. Marquardt, "Collective dynamics in optomechanical arrays," Physical review letters **107**, 043603 (2011) Back to page 76

[137] G. Labeyrie, E. Tesio, P. M. Gomes, G. L. Oppo, W. J. Firth, G. R.M. Robb, A. S. Arnold, R. Kaiser, and T. Ackemann, "Optomechanical self-structuring in a cold atomic gas," Nature Photonics **8**, 321–325 (2014) Back to page 76

[138] E. Tesio, G.R.M. Robb, T. Ackemann, W. J. Firth, and G. L. Oppo, "Spontaneous optomechanical pattern formation in cold atoms," Physical Review A **86**, 031801 (2012) Back to page 76

[139] T. Ackemann, G. Labeyrie, E. Tesio, P. M. Gomes, G.-L. Oppo, W. J. Firth, G. R. Robb, A. S. Arnold, and R. Kaiser, "Hexagonal self-structuring due to optomechanical nonlinearities in cold atomic gases," in *Nonlinear Optics* (Optical Society of America, 2013) pp. NW3B–4 Back to page 76

[140] A. M. Turing, "The chemical basis of morphogenesis," Philosophical Transactions of the Royal Society of London B: Biological Sciences **237**, 37–72 (1952) Back to page 76

[141] M. C. Cross and P. C. Hohenberg, "Pattern formation outside of equilibrium," Reviews of modern physics **65**, 851 (1993) Back to page 77

[142] P. Manneville, *Dissipative structures and weak turbulence* (Springer, 1995) Back to page 77

[143] G. Nicolis, *Introduction to nonlinear science* (Cambridge University Press, 1995) Back to page 77

[144] C. O. Weiss, "Spatio-temporal structures. part ii. vortices and defects in lasers," Physics reports **219**, 311–338 (1992) Back to page 77

[145] H. Haken, "Analogy between higher instabilities in fluids and lasers," Physics Letters A **53**, 77–78 (1975) Back to page 77

[146] L. M. Narducci, *Laser physics and laser instabilities* (World Scientific, 1988) Back to page 77, 90, or 158

[147] C. O. Weiss and R. Vilaseca, "Dynamics of lasers," NASA STI/Recon Technical Report A **92**, 39875 (1991) Back to page 77

[148] Y. I. Khanin, *Principles of laser dynamics* (Newnes, 2012) Back to page 77

[149] P. Mandel, *Theoretical problems in cavity nonlinear optics*, Vol. 21 (Cambridge University Press, 2005) Back to page 77

[150] K. Staliunas and V.J. Sánchez-Morcillo, *Transverse Patterns*, Vol. 183 (Springer, 2003) Back to page 77

[151] A. Esteban-Martín, J. García, E. Roldán, V. B. Taranenko, G. J. de Valcárcel, and C. O. Weiss, "Experimental approach to transverse wave-number selection in cavity nonlinear optics," Physical Review A **69**, 033816 (2004) Back to page 78

[152] S. Barland, J. R. Tredicce, M. Brambilla, L. A. Lugiato, S. Balle, M. Giudici, T. Maggipinto, L. Spinelli, G. Tissoni, T. Knoedl, *et al.*, "Cavity solitons as pixels in semiconductor microcavities," Nature **419**, 699–702 (2002) Back to page 78

[153] W. J. Firth and C. O. Weiss, "Cavity and feedback solitons," Optics and Photonics News **13**, 54–58 (2002) Back to page 78

[154] I. Pérez-Arjona, E. Roldán, and G. J. de Valcárcel, "Theory of quantum fluctuations of optical dissipative structures and its application to the squeezing properties of bright cavity solitons," Physical Review A **75**, 063802 (2007) Back to page 78 or 157

[155] C. Navarrete-Benlloch, G. J. de Valcárcel, and E. Roldán, "Generating highly squeezed hybrid laguerre-gauss modes in large-fresnel-number degenerate optical parametric oscillators," Physical Review A **79**, 043820 (2009) Back to page 78

[156] A. Luis and L. L. Sánchez-Soto, "A quantum description of the beam splitter," Quantum and Semiclassical Optics: Journal of the European Optical Society Part B **7**, 153 (1995) Back to page 80

[157] A. Gatti and L. Lugiato, "Quantum images and critical fluctuations in the optical parametric oscillator below threshold," Physical Review A **52**, 1675 (1995) Back to page 84

[158] A. Gatti, H. Wiedemann, L. A. Lugiato, I. Marzoli, G. Oppo, and S. M. Barnett, "Langevin treatment of quantum fluctuations and optical patterns in optical parametric oscillators below threshold," Physical Review A **56**, 877 (1997) Back to page 84

[159] I. S. Gradshteyn and I. M. Ryzhik, ""routh hurtwith teorem" §15.715 in table of integrals," Series, and Products (Academic, New York, 1980) **1** (1980) Back to page 90 or 158

[160] J. V. Moloney and A. C. Newell, "Nonlinear optics," Physica D: Nonlinear Phenomena **44**, 1–37 (1990) Back to page 98

[161] J. D. Thompson, B. M. Zwickl, A. M. Jayich, F. Marquardt, S. M. Girvin, and J. G. E. Harris, "Strong dispersive coupling of a high-finesse cavity to a micromechanical membrane," Nature **452**, 72–75 (2008) Back to page 117 or 157

[162] B. M. Zwickl, W. E. Shanks, A. M. Jayich, C. Yang, A. C. Bleszynski Jayich, J. D. Thompson, and J. G. E. Harris, "High quality mechanical and optical properties of commercial silicon nitride membranes," Applied Physics Letters **92**, 103125–103125 (2008) Back to page 117

[163] A. M. Jayich, J. C. Sankey, B. M. Zwickl, C. Yang, J. D. Thompson, S. M. Girvin, A. A. Clerk, F. Marquardt, and J. G.E. Harris, "Dispersive optomechanics: a membrane inside a cavity," New Journal of Physics **10**, 095008 (2008) Back to page 117

[164] D. J. Wilson, C. A. Regal, S. B. Papp, and H. J. Kimble, "Cavity optomechanics with stoichiometric sin films," Physical review letters **103**, 207204 (2009) Back to page 117

[165] J. C. Sankey, C. Yang, B. M. Zwickl, A. M. Jayich, and J. G.E. Harris, "Strong and tunable nonlinear optomechanical coupling in a low-loss system," Nature Physics **6**, 707–712 (2010) Back to page 117

[166] M. Karuza, C. Molinelli, M. Galassi, C. Biancofiore, R. Natali, P. Tombesi, G. Di Giuseppe, and D. Vitali, "Optomechanical sideband cooling of a thin membrane within a cavity," New Journal of Physics **14**, 095015 (2012) Back to page 117

[167] M. Karuza, M. Galassi, C. Biancofiore, C. Molinelli, R. Natali, P. Tombesi, G. Di Giuseppe, and D. Vitali, "Tunable linear and quadratic optomechanical coupling for a tilted membrane within an optical cavity: theory and experiment," Journal of Optics **15**, 025704 (2013) Back to page 117

[168] M. Karuza, C. Biancofiore, M. Bawaj, C. Molinelli, M. Galassi, R. Natali, P. Tombesi, G. Di Giuseppe, and D. Vitali, "Optomechanically induced transparency in a membrane-in-the-middle setup at room temperature," Physical Review A **88**, 013804 (2013) Back to page 117

[169] U. Kemiktarak, M. Metcalfe, M. Durand, and J. Lawall, "Mechanically compliant grating reflectors for optomechanics," Applied Physics Letters **100**, 061124 (2012) Back to page 117

[170] U. Kemiktarak, M. Durand, M. Metcalfe, and J. Lawall, "Cavity optomechanics with sub-wavelength grating mirrors," New Journal of Physics **14**, 125010 (2012) Back to page 117

[171] U. Kemiktarak, C. Stambaugh, M. Durand, and J. Lawall, "Optomechanics with subwavelength grating membranes inside a fabry-perot cavity," in *Laser Science* (Optical Society of America, 2013) pp. LTh3G–4 Back to page 117

[172] C. Sánchez del Rio (Coordinador), *Físca Cuántica* (Piramide, 1999) Back to page 127

[173] Michael A Nielsen and Isaac L Chuang, *Quantum computation and quantum information* (Cambridge university press, 2010) Back to page 131

[174] E. Roldán, "El modelo de jaynes-cummings," Óptica pura y aplicada **44**, 361–379 (2011) Back to page 133

[175] E. del Valle, *Microcavity Quantum Electrodynamics* (VDM Verlag, 2010) Back to page 137

[176] A. Gonzalez-Tudela, E. del Valle, E. Cancellieri, C. Tejedor, D. Sanvitto, and F. P. Laussy, "Effect of pure dephasing on the Jaynes-Cummings nonlinearities," Opt. Express **18**, 7002 (2010) Back to page 137

[177] S. Kolpakov, A. Esteban-Mart'ın, F. Silva, J. García, K. Staliunas, and G. J. de Valcárcel, "Experimental demonstration of hyperbolic patterns," Phys. Rev. Lett. **101**, 254101 (2008) Back to page 145

[178] M. J. Hartmann, F. G.S.L. Brandao, and M. B. Plenio, "Strongly interacting polaritons in coupled arrays of cavities," Nature Physics **2**, 849–855 (2006) Back to page 156

[179] A. D. Greentree, C. Tahan, J. H. Cole, and L. C.L. Hollenberg, "Quantum phase transitions of light," Nature Physics **2**, 856–861 (2006) Back to page 156

[180] D. G. Angelakis, M. F. Santos, and S. Bose, "Photon-blockade-induced mott transitions and x y spin models in coupled cavity arrays," Physical Review A **76**, 031805 (2007) Back to page 156

[181] A. Schliesser, P. Del'Haye, N. Nooshi, K. J. Vahala, and T. J. Kippenberg, "Radiation pressure cooling of a micromechanical oscillator using dynamical backaction," Physical Review Letters **97**, 243905 (2006) Back to page 157

[182] O. Romero-Isart, A. C. Pflanzer, F. Blaser, R. Kaltenbaek, N. Kiesel, M. Aspelmeyer, and J. I. Cirac, "Large quantum superpositions and interference of massive nanometer-sized objects," Physical review letters **107**, 020405 (2011) Back to page 157

[183] L. Mandel and E. Wolf, *Optical coherence and quantum optics* (Cambridge university press, 1995) Back to page 157